FACHBEREICH PHYSIK
BERGISCHE UNIVERSITÄT
GESAMTHOCHSCHULE WUPPERTAL

Search for extragalactic γ-ray point sources with the HEGRA air shower array

Stefan Westerhoff

Oktober 1996
WUB-DIS 96-18

FACHBEREICH PHYSIK
BERGISCHE UNIVERSITÄT
GESAMTHOCHSCHULE WUPPERTAL

Search for extragalactic γ-ray point sources with the HEGRA air shower array

Stefan Westerhoff

Dissertation

zur Erlangung des Doktorgrades
des Fachbereiches Physik
der Universität Wuppertal

Oktober 1996
WUB-DIS 96-18

Abstract

The success of earth-based air shower arrays in detecting point sources of cosmic rays above 10 TeV depends crucially on the possibility of finding efficient methods for separating γ-induced air showers from the background of hadron-induced showers. In this thesis, a γ/hadron separation based on the charged particle content and energy distribution of air showers is developed. The information is provided by the multi-layer calorimeter-like Geiger towers within the HEGRA air shower array. The event selection uses computer-simulated neural networks trained on MC data.
The separation method is applied to Geiger tower data taken between November 1994 and April 1995 to search for γ-ray emission from the superposition of nearby northern blazars. Together with an additionally analyzed sample of scintillator data taken between 1989 and 1992, a $5.5\,\sigma$ excess from the superposition of 12 sources with redshift $z \leq 0.062$ is observed. The non-detection of sources at higher redshifts is evidence for the postulated infrared-to-optical background radiation becoming relevant above $z = 0.07$ at HEGRA energies. The X-ray-selected flat-spectrum AGN 0116+319 is the strongest source in both time periods and yields a $4.9\,\sigma$ excess.

Contents

List of Figures

List of Tables

Chapter 1

Introduction

Ever since their discovery in 1912, cosmic rays have been a great stimulation for particle physics. The first detection of positrons and muons in cloud chamber experiments by Anderson in 1932 and 1936 [1], and the detection of the pion on photographic plates by Powell in 1947 [2] are important milestones on the way to today's picture of the fundamental constituents of matter and the interactions between them.
In a striking contrast to this impact on modern elementary particle physics, the main questions related to cosmic rays themselves have remained largely unsolved up to the present. We neither know the origin of the most energetic cosmic rays particles, nor the processes which are able to accelerate them to energies up to 10^{20} eV.
In the last 5 years, satellite experiments like the EGRET detector on board the Compton Gamma Ray Observatory CGRO and earth-bound detectors like the Whipple Čerenkov telescope have finally cast some light on the origin of extragalactic cosmic rays. EGRET has by now successfully detected more than 50 extragalactic GeV-γ point sources, all of them belonging to the class of objects called Active Galactic Nuclei (AGN) [3, 4, 5]. As shown by the Whipple group, at least two of them, the nearby blazars Mrk 421 and Mrk 501, also emit TeV-γ rays [6, 7], which means that γ-radiation from these objects has now successfully been observed covering 18 orders of magnitude in energy, from radio observations at 10^{-6}eV up to TeV γ-energies.
Apart from being a challenge to all theories trying to explain the physical processes in AGN which lead to γ-flux from radio to TeV, these observations have again raised the question whether AGN or sub-classes of AGN may be visible at even higher energies. Above 10 TeV the task of searching for a γ-flux from these sources is taken over by large earth-bound detector arrays like the HEGRA (High Energy Gamma Ray Astronomy) array situated 2200 m a.s.l. on the Canary Island La Palma. These so-called air shower arrays detect the primary particle rather indirectly by the huge amount of secondary particles induced by the incident cosmic ray primary in the Earth's atmosphere.
The discovery of cosmic ray point sources at HEGRA energies would unequivocally answer questions concerning the origin of the γ-rays and their acceleration. Hence, great effort has been devoted to the search for > 50 TeV sources. Nevertheless, no extragalactic source above 10 TeV has been established with sufficient significance up to now.
As an explanation of the rather disappointing performance of air shower arrays, the in-

evitable interaction between the TeV γ-rays and the photons of the infrared-to-optical background radiation has been claimed [8]. Based on the results of the Whipple observation of Mrk 421, various authors [9, 10] derive a rather high strength of the infrared background which would virtually rule out the possibility of detecting point sources at energies above 10 TeV.

But in contrast to the well-known 2.7 K microwave background radiation, there is no direct measurement of the infrared background up to now, and any prediction remains uncertain at present. Only the measurement of the TeV spectra of several sources and the observation of sources at different redshifts may give us a clue about the actual strength of the cosmic infrared background which is otherwise difficult to probe.

Nevertheless, even in case the infrared absorption is not as high as predicted and equals the lower limits from galaxy counting, we have to face the problem that any γ-flux above 50 TeV will be rather marginal, and trying to establish sources in this energy region will soon verge on the limitations of current detector arrays. For about a decade, various air shower arrays have only produced upper limits for the flux from individual extragalactic sources. Any new attempt therefore depends crucially on at least two items.

- Is it possible to increase the rather bad signal-to-noise-ratio of air shower arrays ?

In air shower physics, searching for γ-showers means separating them from the overwhelming background of hadron-induced showers which have lost the information about their origin by deflection in the intergalactic magnetic fields. In past and current applications, γ/hadron separation is mainly based on the difference in the muon content of both shower types. Approaches taking advantage of the Čerenkov light are promising, but are restricted to appropriate night sky and weather conditions.

Within the scope of this thesis, a new method based on the muon and high energy particle content and the different lateral and energetic distribution of charged particles in air showers is developed. This allows an all-day γ/hadron separation going beyond ordinary muon counting. The experimental tool for this analysis is the sub-array of 17 Geiger towers which has been installed as an integral part of the HEGRA array. For the first time, these multi-layer detectors allow both the tracking of muons and high energy $e^{\pm}$ *and* give valid calorimetric information at different distances from the shower core.

Due to the complexity of the input information, the analysis is consequently based on computer-simulated neural networks, a powerful technique of data analysis which is well-established in high energy physics by now. As it replaces the serial cuts in the artificially reduced data space typical of conventional analysis by parallel handling of all available information, the application of neural networks and other methods of multivariate analysis is self-evident in cases where efficient and economic data analysis based on a large number of measured quantities is crucial.

Apart from the development of a γ/hadron separation technique, a major part of this thesis is dedicated to a question with strong connection to theory.

- What sort of sources are likely candidates for 50 TeV emission ?

The successful observations in the GeV and TeV region by EGRET and the Whipple and HEGRA Čerenkov telescopes imply that the highest energy γ-rays in AGN are

produced in jets beamed at the observer. AGN where the jet axis is closely aligned with the line-of-sight form the blazar sub-class. Rapid variability by orders of magnitude in luminosity on a time scale of a few days, Doppler boosted emission and superluminal motion of radio knots, and a high degree of optical polarization are their main features. About 15 sources which are known to belong to the blazar class have redshifts below $z \simeq 0.1$ and are promising candidates for detection at TeV energies. In a recent paper [11], the TeV flux of these sources has been predicted on the basis of the proton blazar model [12], using multi-frequency data of all available energy regions. This source compilation is the basis of the point source search described in the following chapters.
Comprising a catalogue of equivalent sources allows to treat them as a class rather than as individual objects. Whenever only a marginal signal is expected, the sensitivity can be increased further by searching for a *cumulative* γ-excess from the *superposition* of n sources, thus imitating an n-fold observation of a single "generic" source. This stacking method is a common tool of astronomy.

Neural network based γ/hadron separation and stacking promising TeV sources are the two "leitmotivs" of this thesis. Taken together, they considerably increase the sensitivity of HEGRA and thus justify a new attempt at establishing TeV sources.
The thesis is organized as follows: Chapter 2 roughly outlines the mechanisms leading to multi-wavelength emission of AGN and summarizes today's knowledge on the infrared-to-optical background radiation, which plays a decisive role in TeV astrophysics. Chapter 3 describes the experimental tool of this analysis, the HEGRA detector, and the physical differences of γ- and hadron-initiated air showers which are accessible to measurement. The analysis technique is described in Chapter 4: after a brief sketch of the neural network approach and the algorithm for network training, various methods to illuminate the network separation are applied.
Chapter 5 and Chapter 6 are devoted to the analysis of data taken with the HEGRA array between October 1994 and May 1995. Apart from a new limit on the isotropic γ-flux between 50 and 100 TeV and on the diffuse γ-ray flux from the Galactic disc, the results of the search for extragalactic point sources, mainly the blazar sample of Chapter 2, are presented. Chapter 7 finally summarizes the results.

Chapter 2

Concepts of TeV γ-astronomy

High energy γ-ray astronomy is a relatively young research field. The first experiments in space were launched in the early 1960s, and ground-based TeV astronomy started up in the mid-1970s. From the first telescope missions till today, the sensitivity of the instruments has increased dramatically, from a few detected photons (EXP XI, OSO-3, SAS 2) to the large number of sources established with high statistical significance in the MeV to GeV energy region by now (COS-B, EGRET).
The launch of the Compton Gamma-Ray Observatory CGRO by NASA in 1991 meant an enormous influx of data from 50 keV to 30 GeV. TeV astronomy as done with HEGRA has received a large boost from CGRO data, and attention has focussed on the class of galaxies with strong non-thermal activity in their center caused by Active Galactic Nuclei (AGN). The EGRET detection of GeV γ-emission from about 50 AGN is of fundamental importance, as AGN are now established as the most luminous class of extragalactic objects *even at energies about GeV.*
In the first part of this chapter, the different manifestations of AGN are discussed and one particular model of the main AGN mechanisms is presented which also provides us with a unified classification scheme.
Whether or not subclasses of AGN are also γ-emitters above 50 TeV is still a controversial subject, together with the question which mechanisms actually produce particles of such enormous energies. Two models, the inverse-Compton blazar and the proton blazar model, are outlined in this chapter. Only one of them, the proton blazar, predicts γ-emission with energies exceeding 10 TeV.
The main aim of this chapter is to build a catalogue of potential sources of TeV γ-rays. To do this, we also have to analyze the inevitable influence of the various cosmic ray background components on traversing particles. The second part therefore concentrates on the interactions of TeV γ-rays with photons of the microwave and infrared background. Here, high energy γ-ray astronomy receives major input from particle physics.

2.1 High energy γ-ray astronomy

2.1.1 Radio galaxies with active nuclei

A large number of galaxies are strong radio sources, i. e. their emission at radio frequencies exceeds their optical emission. Cygnus A at $z = 0.056$ was the first radio source to be discovered in 1946, and although it is the second-brightest object at radio energies, the optical counterpart was not found before 1956 and turned out to be extremely weak.
Cyg A has a morphology which is typical of most strong radio sources. The main radio emission does not originate from the galaxy itself, but from two symmetric regions in a distance of $\simeq$ 170 kpc [1] from the center and thus far outside the (optical) galaxy. The extended outer radio sources include small regions of intense radio emission, so-called HOT SPOTS. Fig. 2.1 shows a VLBI (Very Long Baseline Interferometry) 6 cm observation of Cyg A with a radio source in the position of the galaxy, two extended regions far outside, and a jet reaching from the central region to the outer radio sources.
The elongated structure of radio emission as visible in Cyg A is observed for about 2/3 of these objects and typically has a size of 0.1 to 0.5 Mpc.
Radio galaxies may roughly be divided into two classes according to the strength of the emission from the central region: in contrast to "normal" galaxies, "active" galaxies release strong non-thermal radiation from a compact core situated in the center of the galaxy, the ACTIVE GALACTIC NUCLEUS (AGN). The strength of the non-thermal emission varies with time and covers nearly the whole electromagnetic spectrum from radio to optical and X-ray emission and even to γ-rays with GeV and TeV energies. The actual strength and the type of the emission is used as a classification scheme for the different manifestations of the AGN phenomenon.
The origin of this strong emission is in fact the center of the galaxy. As an example, Fig. 2.1 shows the X-ray intensity of Cyg A as measured by the X-ray satellite ROSAT. Whereas the radio emission is rather complex and reveals the morphology of the object, the X-ray emission basically originates from the active nucleus.
The spark chamber experiment EGRET [13] on board the CGRO has intensively studied radio galaxies in the energy region from 30 MeV to 30 GeV and has positively detected more than 50 AGN by now, among them 40 with high significance [4, 5]. As a rather striking result, the intensity of γ-emission in general exceeds the luminosity at other energies.
The distribution of AGN detected by EGRET is similar to the distribution at radio energies, i. e. EGRET detection is not restricted to the most nearby sources, but also includes a significant number at large redshifts.
Apart from showing that their spectrum reaches at least to GeV energies, the EGRET results on AGN are remarkable from another point of view. Out of the variety of different types of AGN, EGRET only detects *radio-loud, flat-spectrum radio-sources*, i. e. objects with a radio intensity in the energy range below $\simeq$ 5 GHz which may be described by a power law

$$I_\nu \propto \nu^{-\alpha} \tag{2.1}$$

[1] $1\,\mathrm{pc} = 3.086 \cdot 10^{16}\mathrm{m} = 3.26\,\mathrm{ly}$

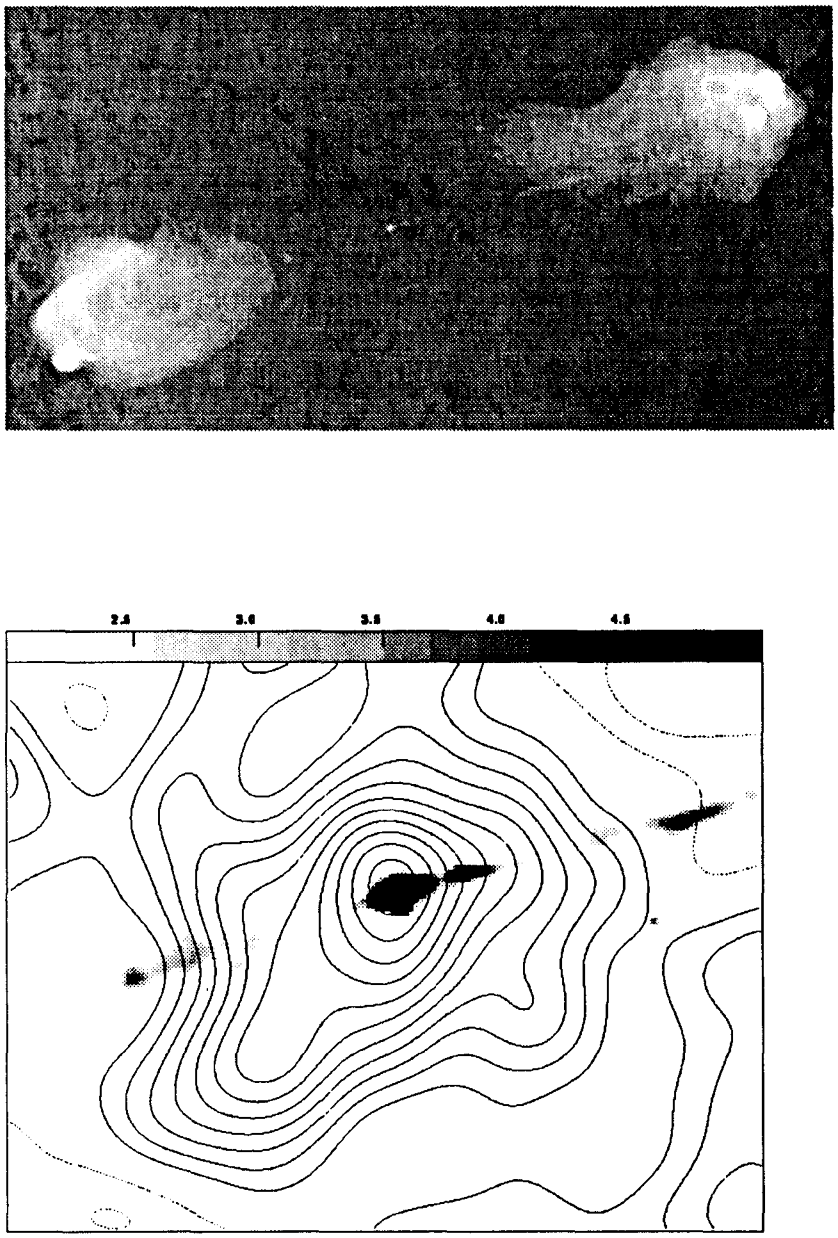

Figure 2.1: **Cyg A at radio and X-ray energies: VLBI picture at 6 cm (top) and VLA picture with ROSAT X-ray observation as superimposed contour map (bottom). The grey scale covers the 2 to 5 mJy range, the contour intervals are linear from -0.2 to 1.1 counts per $0.5''$ pixel in steps of 0.1.**

with a spectral index $\alpha \leq 0.5$, I_ν being the intensity of the emission and ν the frequency. In order to understand the implications of this result especially for TeV γ-astronomy, we have to discuss briefly some characteristics of AGN, their mechanism, and the most important sub-classes.

AGN characteristics

One of the most striking features of AGN is their compactness: as an example, the luminosity in γ-rays above 100 MeV of 3C 279 [14] has been found to be $5 \cdot 10^{40}$ W, which equals the total energy output of 10^{14} suns. The factor of five change in luminosity observed for this AGN during two days means that the emitting region is smaller than $10^{-6}\,\mathrm{pc}^3$, as

$$\gamma\, c\, t_{var} \simeq 5 \cdot 10^{13}\,\mathrm{m} \simeq 2 \cdot 10^{-2}\,\mathrm{pc}, \tag{2.2}$$

where γ is the Lorentz factor ($\simeq 10$ for typical AGN, see below), is an upper limit of the size of the object. The implication that an enormous power is released from a very small volume almost directly leads to black holes as candidates for the central engine of AGN: the "size" of a black hole is given by its Schwarzschild radius

$$R = 2GM = 3.1 \cdot 10^{-13} \left(\frac{M}{M_\odot}\right) \mathrm{ly} \simeq 10^{-13} \left(\frac{M}{M_\odot}\right) \mathrm{pc}, \tag{2.3}$$

G being the gravitational constant, M the mass of the object, and $M_\odot$ the mass of the sun. Thus the typical radius of $10^8\, M_\odot$ black holes is in the order of light hours to light days, and indeed there is widespread believe that AGN are powered by black holes with $10^6 - 10^{10} M_\odot$ sitting in the center of galaxies.
To further motivate this general picture of the nucleus of active galaxies and to get an overview of the different types of AGN, we will shortly review the history of their discovery.

The AGN zoo

Active nuclei are by no means a common feature of galaxies: normal galaxies are much more abundant than active galaxies. The first observed sub-class of AGN were the SEYFERT GALAXIES, discovered in 1943 by C. K. Seyfert by their optical emission. They are mostly spiral galaxies with star-like nuclei showing broad permitted emission lines and either narrow (Sy 1) or broad (Sy 2) forbidden lines. The term "forbidden" is rather misleading; it characterizes emission lines which in contrast to "permitted" lines with Einstein coefficients (i. e. transition probabilities) of the order $A = 10^8\,\mathrm{s}^{-1}$ (typical for electric dipole emission) have transition probabilities $A \simeq 0.01\,\mathrm{s}^{-1}$ (magnetic dipole emission, electric quadrupole emission).
An important feature of all Seyfert nuclei is their time variability from radio- to X-ray on time scales of months to years.
History of AGN discoveries continued in the 1960s with the optical identification of a number of strong radio sources from the 3rd Cambridge Catalogue (3C)[2]. Appearing

[2]For a listing of the main radio catalogues see Tab. 2.2

as point objects even when observed with the 5 m Mt. Palamor mirror, the outstanding feature of these QUASI-STELLAR RADIO SOURCES or QUASARS (M. Schmidt, 1962) is their enormous distance: 3C 273, as one of the most prominent representatives of this class and the first to be discovered, has a redshift of $z = 0.158$. Today, this may be called "nearby", as by now, quasars up to $z = 4.9$ (PC[3] 1247+3406) are known.
Strong radio emission, stellar appearance, great distances, and brightness variability are typical for quasars, and following their discovery, a few thousand of them have been catalogued by now (3570 with known redshift in the catalogue of Hewitt and Burbidge, 1987 [15]).
Direct observational confirmation that quasars are situated in the center of galaxies is difficult to obtain. Only for the nearest objects like 3C 273, the host galaxies are visible with CCD techniques, and these observations imply that the strong emission indeed comes from the active nucleus of the host galaxy. Recently, observations of four quasars with low redshift ($z \leq 0.5$) with the refurbished Hubble Space Telescope (HST) reveal details of the galaxies. All four quasars have elliptical hosts with at least one very close companion [16].
In 1965, the class of radio-quite quasars was discovered by A. Sandage. They have characteristics similar to the radio-loud quasars in the optical, but are only weak radio sources. It is almost certain now that these QUASISTELLAR OBJECTS or QSOs are just another manifestation of the quasar and thus the AGN class. In fact, only about 5% of all quasars are radio-loud [17].
The next sub-class of AGN discovered in 1969 is rather important for the following analysis and is connected to a historical classification error. The variability of the (extragalactic) object BL Lacertae ($2200 + 420, z = 0.069$), looking like a star in optical telescopes, mislead C. Hoffmeister (1929) to classifying it as a variable star. In 1969, a compact radio source was discovered in the same position , and it became obvious that BL Lac is not a star, but a prototype of a new class of objects with features similar to quasars, but with very weak emission lines, thus making a redshift measurement difficult. BL LACS are rapidly variable on time scales of hours to days at all wavelengths. The optical spectra are featureless and the continuum radiation is strongly polarized ($\leq 30\%$) with the polarization varying with time. Approximately 200 objects of this class are catalogued by now [18].
In many respects similar to BL Lacs is another class of AGN with very high radio activity, the OPTICALLY VIOLENT VARIABLES or OVVS. This small fraction of quasars is known to change their optical flux by more than an order of magnitude within a week. Like BL Lacs, but unlike most quasars, they show strong, variable, linear polarization. BL Lacs and OVV quasars form the so-called BLAZAR class [19].

To complicate the situation further, there is a number of additional classification schemes cataloguing objects with special observational characteristics: AGN with optically bright, star-like nuclei are called N-TYPE GALAXIES (W. W. Morgan, 1958), and following B. E. Markarian (1967) [20], galaxies with a strong ultraviolet excess compared to normal galaxies are called MARKARIAN (MRK) GALAXIES.

[3]PC=Palamor CCD catalogue

Designing an AGN

The observational data on Seyfert galaxies, quasars, QSOs, OVVs, and BL Lac objects imply that in spite of their different characteristics, they are in a certain sense just different symptoms of the same phenomenon, the *activity in the nucleus of a galaxy.* A model which aims at a unified understanding of the zoo of AGN has to explain the observed differences in radio intensity and optical polarization as well as the common features like variability and compactness.

We have a model of AGN which explains at least qualitatively most of the observations and furthermore allows to simplify a lot the rather eccentric historical classification scheme given above. A schematic view of the main ingredients we need is shown in Fig. 2.2.

As motivated above, there is strong – but yet no direct – evidence that the central engine of all AGN is a BLACK HOLE – at least we cannot think of any other object fulfilling the rather extreme demands following from observation. The black hole cre-

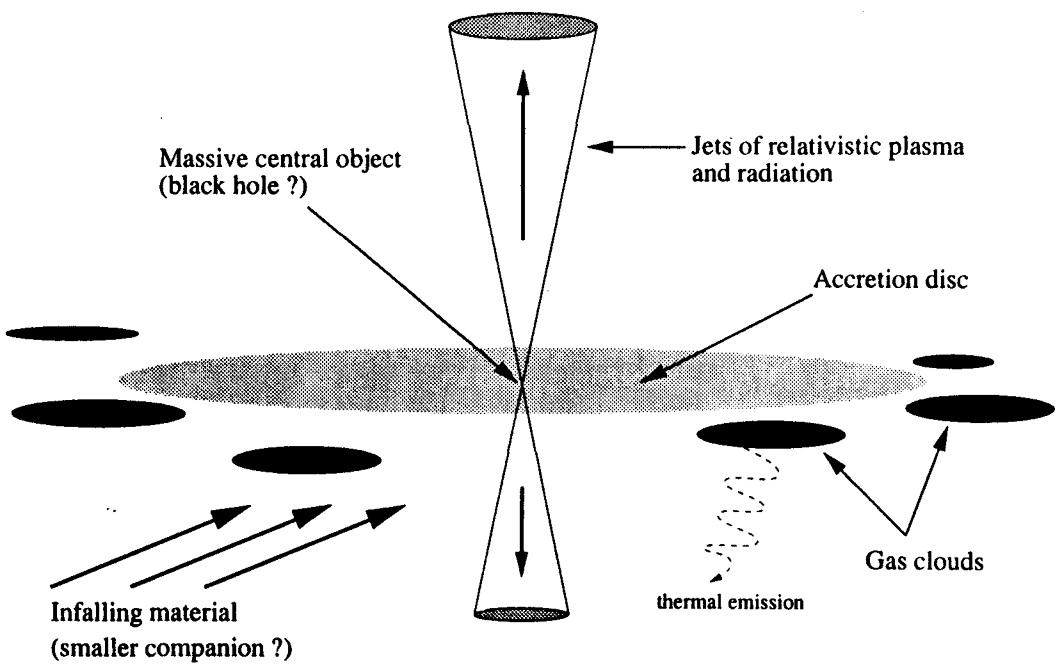

Figure 2.2: **Schematic of an AGN.**

ates two opposing JETS of relativistic plasma and radiation which, due to relativistic beaming, are highly collimated. The jets carry the plasma to the outer regions, where collisions with the intergalactic medium (IGM) and the intracluster medium (ICM) lead to the observed HOT SPOTS of intense radio emission. An ACCRETION DISC with the black hole in its center is the source of the material flowing to the jets and also the main source of X-rays.

There is a lot of observational evidence supporting this model. As explained above, almost all Very Long Baseline Interferometry (VLBI) observations of compact sources show an elongated radio structure, in an average distance of several 100 kpc from the core, with one or two jets emerging from the central region.
To explain the observed luminosity L_q of quasars, $3 \cdot 10^{14}\, L_{\odot}$, the accretion rate $\dot{M}$ necessary to fuel the AGN is

$$L_q \propto \epsilon \dot{M} \simeq 10 \ldots 100 \, \frac{M_{\odot}}{\mathrm{y}}, \tag{2.4}$$

where $\epsilon \simeq 0.1$ is the efficiency of the conversion process.
The idea that a central engine in the nucleus of a host galaxy is fuelled by matter falling onto it is further supported by the recent Hubble Space Telescope observations quoted above: although the number of objects is too small to make the result statistically

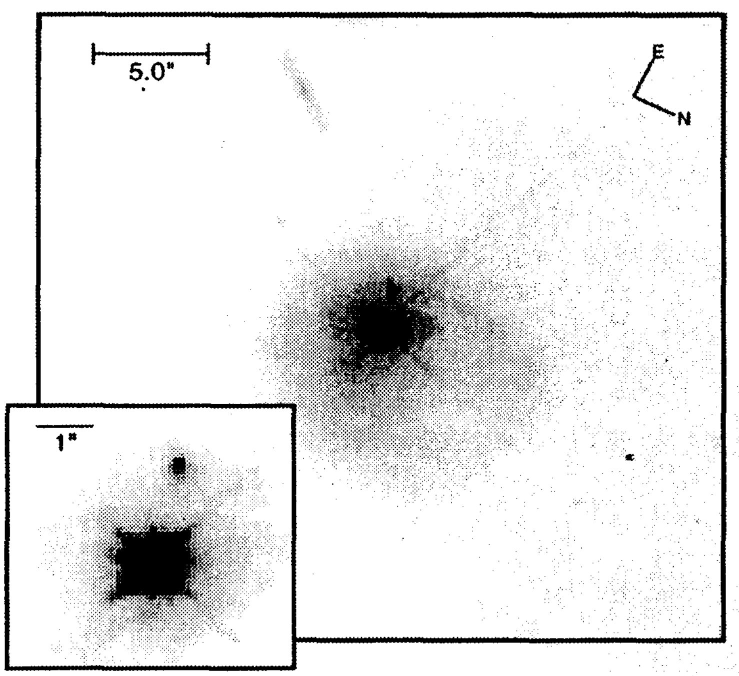

Figure 2.3: **Hubble Space telescope picture of the quasar PKS 2349 and its small companion galaxy. The picture is taken with the Wide Field Planetary Camera 2. Taken from [21].**

conclusive, the host galaxies of the four quasars seem to be interacting with a smaller companion, implying that we are actually observing merging events [16]. This could be an explanation of the striking fact that radio-loud quasars are always found in elliptical galaxies, whereas radio-quiet quasars have spiral hosts: collisions between galaxies are known to convert spirals to ellipticals.
As an example, Fig. 2.3 shows a HST picture of the quasar PKS 2349-014 [21]. The close companion galaxy caught by the quasar is clearly visible and is supposed to provide the AGN with infalling material necessary to fuel the central engine.

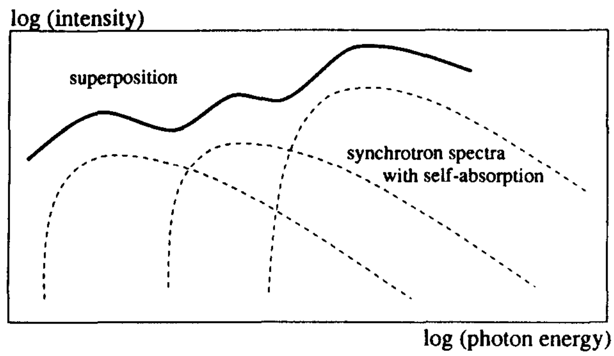

Figure 2.4: **Superposition of synchrotron spectra yields a flat radio spectrum.**

2.1.2 Relativistic jets

How does the model outlined in the previous subsection explain the AGN spectra and the different manifestations of AGN ?
The radio spectrum of AGN is a superposition of *thermal* and *non-thermal* components. The term thermal summarizes the line emission, e. g. the 21 cm line from the hyperfine structure transition of neutral hydrogen in so-called H I-regions, and the continuum emission from bremsstrahlung of ionized hydrogen in H II-region and gaseous nebulae. The thermal emission basically comes from the accretion flow ("UV bump" at 300 nm) and the heated dust and gas surrounding the nucleus.
In addition to the thermal radiation, there is a non-thermal spectrum with an intensity described by $I_\nu \propto \nu^{-\alpha}$. As pointed out by H. Alfvén and N. Herlofson in 1950, the power-law dependence is strong evidence for *synchrotron emission* of relativistic electrons being the main process. Whereas thermal radio continua are characterized by an intensity I_ν (almost) independent of ν, synchrotron radiation from a non-thermal distribution of electrons with number density $n(E) \propto E^{-\gamma}$, with E denoting the electron energy, automatically leads to power laws $I_\nu \propto \nu^{-\alpha}$ with $\alpha = 1/2\,(\gamma - 1)$ (see e. g. [22]). Note that this is not true for optically thick sources with a high degree of self-absorption.
Most non-thermal cosmic sources (like extragalactic radio galaxies) have $0.2 \leq \alpha \leq 1.2$, and there is indeed no *extended* source with an index below 0.5.
In contrast to this, a flat ($\alpha \leq 0.5$) or even inverted ($\alpha \leq 0$) radio spectrum is observed in most *compact* objects. In some cases, the spectrum is flat, but shows a considerable structure, so the description by a power laws fails (see 3C 120 in Fig. 2.13 as an example). This was explained in 1969 by Kellermann and Pauliny-Toth [23] as a result of the superposition of several synchrotron spectra with different low-frequency cutoffs due to synchrotron self-absorption (below a certain cutoff frequency ν_{cut}, the synchrotron radiation is re-absorbed by the relativistic electrons). Fig. 2.4 illustrates the superposition effect.
The interpretation of AGN radio-to-optical spectra by synchrotron emission from a non-thermal distribution of relativistic electrons nevertheless is insufficient and does

not yet explain some phenomena connected to the elongated radio structure. For a number of sources, (apparent) superluminal motion of radio knots has been observed. VLBI observations of 3C 273 [24] e. g. show that the compact source in the position of the quasar expands with an apparent velocity of about 11 c.
Another difficulty arises from the compactness of the sources. Calculating the radio brightness temperature of some variable objects with an estimated size of $c\,t_{var}$ gives temperatures above 10^{12} K, thus exceeding the inverse-Compton limit: for $T_{max} \geq 10^{12}$ K, the ratio of radiation intensity L_{IC} from inverse-Compton up-scattering of a low energy γ to a high energy γ^* by relativistic electrons [4],

$$e^- \gamma \longrightarrow e^- \gamma^*, \tag{2.5}$$

to the synchrotron emission intensity L_{syn} increases catastrophically like

$$\left(\frac{L_{IC}}{L_{syn}}\right) \propto \left(\frac{T}{10^{11}\mathrm{K}}\right)^{10}, \tag{2.6}$$

hence leading to immediate cooling of the source [23].
The way out of this dead end was shown in 1979 by Blandford and Königl in their paper on relativistic jets [22]: the radio emission of variable extragalactic radio sources originates both from the collimated jet and *from shocks and density inhomogeneities propagating as* KNOTS *along the jet.*
The model states that radio emission of AGN comprises two different components:

1. isotropic, steady, unpolarized optical continuum emission from the jet itself (hot spots, lobes), and

2. a variable, strongly polarized synchrotron emission from behind shock fronts propagating along the jet ("nuclear jet").

Fig. 2.5 shows a scheme of the jet topology. The nuclear jet region at short distance (1 . . . 10 pc) from the blazar is the source of synchrotron radiation, whereas isotropic emission, e. g. from hot spots, is emitted far outside at a distance of $10^2 \ldots 10^3$ pc.
One of the most important parameters of this model is the angle θ between the line-of-sight to the observer and the jet axis: the different types of AGN from radio-quiet to radio-loud quasars and variable blazars are in fact morphologically similar sources, the only difference being the *decreasing viewing angle* θ.
In this picture, bright double radio sources, e. g. Cyg A with its two clearly visible jets, are viewed edge-on with $\theta \simeq 90°$. In contrast to this, the brightest compact sources have jets with a small angle to the line-of-sight ($\theta \leq 10°$), and in blazars the jet is directly beamed towards us, i. e. we are within the cone with solid angle $1/\gamma_{jet}^2$.
With decreasing viewing angle to the jet axis, the radio spectrum of the sources becomes flatter as the observer now mainly sees the synchrotron radiation of the nuclear jet. As explained above, the superposition of the flux from knots with increasing cutoff frequency due to synchrotron self-absorption in the high magnetic fields of the jet

[4] In this thesis references to a specific charged state are to be interpreted as also implying the charge conjugate state.

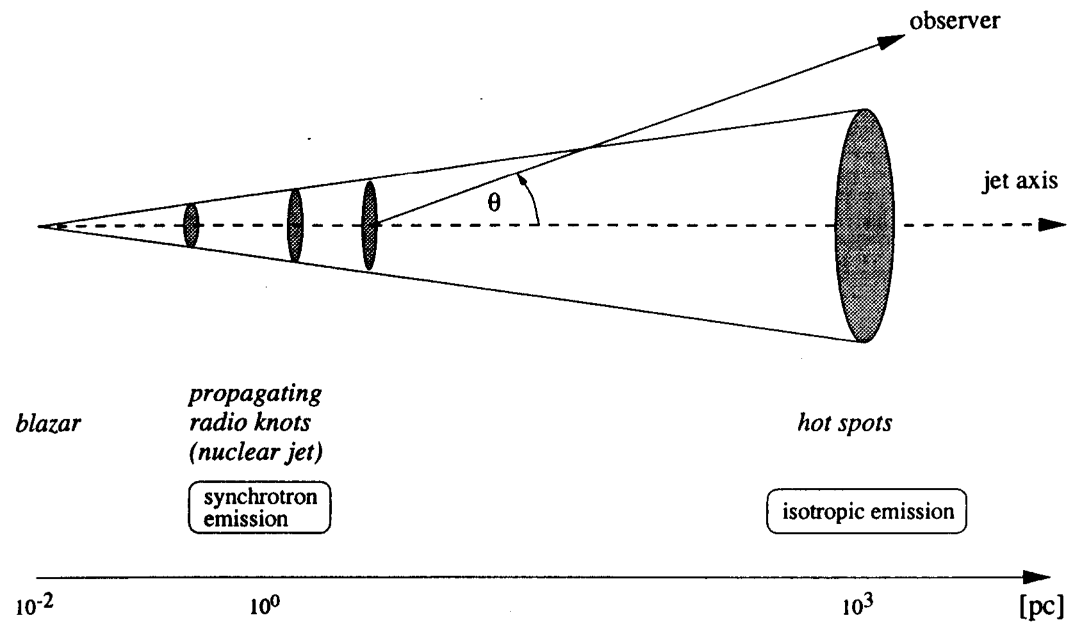

Figure 2.5: **Scheme of the jet topology.**

automatically yields flat spectra [23]. Furthermore, due to the increasing compactness of the emission volume, the polarization increases [22]. Outside the jet cone, the luminosity of the nuclear jet decreases rapidly and the isotropic radio component, e. g. from hot spots, dominates. The frequent outbursts of blazars are explained by knots traversing positions in the jet where θ has a value of maximal luminosity amplification (see next subsection).

The emission lines, i. e. the thermal spectra of AGN, are related to the optical- to X-ray continuum emission of the isotropic component, which photoionizes gas in the clouds surrounding the central source. In BL Lacs, where the emission lines are almost invisible, either the amount of gas in the neighborhood of the source is too small or, due to the small viewing angle, the jet synchrotron component totally covers the isotropic component.

Kinematical effects

The picture of relativistic bulk motion along a jet explains some kinematical effects of relativistic beaming, the apparent superluminal motion of radio knots and the absence of an observed counter-jet on the radio maps of several AGN.

Let $\vec{\beta}_{obs}$ be the observed velocity of a radio knot in a jet with velocity $\vec{\beta}_{jet}$. θ is the angle between the jet axis and the line-of-sight $\vec{n}$. Then due to Doppler boosting, the observed velocity is given by

$$\vec{\beta}_{obs} = \frac{\vec{n} \times (\vec{\beta}_{jet} \times \vec{n})}{1 - \vec{\beta}_{jet}\,\vec{n}}, \tag{2.7}$$

so for $\left|\vec{\beta}_{obs}\right|$ we get

$$\beta_{obs} = \frac{\beta_{jet}\ \sin\theta}{1 - \beta_{jet}\ \cos\theta}. \tag{2.8}$$

If θ is small, i.e. we almost directly look into the jet, this becomes

$$\beta_{obs} = \frac{\beta_{jet}\ \theta}{\frac{\theta^2}{2}\ \beta_{jet}} = \frac{2}{\theta}. \tag{2.9}$$

For 3C 273 with its apparent superluminal motion of $\beta_{obs} \simeq 11$ [24], this implies an angle between jet axis and line of sight of $\simeq 10°$.
Superluminal motion is thus an effect of relativistic bulk motion. In blazars, where according to the model the jet axis is aligned close with the line-of-sight, superluminal motion is expected, and indeed at present 30 objects are known to be superluminal sources, most of them showing properties similar to blazars. Apart from sources like 3C 273 and 3C 279, also Mrk 421 is reported to show evidence of superluminal flow [25].
Note that β_{obs} in Equation 2.8 has a maximum when the condition

$$\beta_{jet} = \cos\theta \tag{2.10}$$

resp.

$$\sin\theta = \frac{1}{\gamma_{jet}} \tag{2.11}$$

is fulfilled. This implies that we observe an apparent *outburst* of the blazar when the propagating radio knot traverses a jet radius where the relativistic amplification of the luminosity reaches a maximum.
Doppler boosting is also responsible for another effect which caused some irritation in the past. Whereas the 2-jet structure is clearly observable for a number of radio galaxies, there are also radio galaxies where only one jet is visible.
To explain this anisotropy, we have to consider the transformation of the flux density $S(\nu) \propto \nu^{-\alpha}$ from the comoving system of the radio jet to the observer's frame.
As the observed frequency is

$$\nu_{obs} = D_{jet}\nu \tag{2.12}$$

where D_{jet} is the Doppler factor

$$D_{jet} = \frac{1}{\gamma_{jet}(1 - \beta_{jet}\cos\theta)}, \tag{2.13}$$

the flux density and the total luminosity transform as [22]

$$S_{obs}(\nu) = D_{jet}^{3+\alpha} S(\nu) \tag{2.14}$$

$$L_{obs} = D_{jet}^{3} L, \tag{2.15}$$

so the luminosity of the jet directed towards the observer is Doppler increased by a factor D_{jet}^3, whereas the luminosity of the opposite jet is diminished by the same factor. Note that a factor D_{jet}^2 comes from the Doppler effect on the solid angle of the emission

cone, and a factor of D_{jet} from the blue-shifting, which increases the number of photons per unit time.
The transformation behavior explained above also holds for the brightness temperature, which thus also appears increased by Doppler boosting. Furthermore, the bending of jets observed for some sources is a result of relativistic projection effects which "blow up" small deviations of the jets from collinearity.

2.1.3 TeV γ-emission from AGN

The activity of AGN generally shows up as *thermal* emission in the far-infrared, ultraviolet, and soft X-ray region, and a broad *non-thermal* continuum from radio to γ-rays. In radio-quiet AGN, the thermal component dominates, whereas in radio-loud AGN, mainly the non-thermal synchrotron emission from the propagating shocks is visible. This allows us to replace the classification given in Section 2.1.1, which is strongly biased by history, by a unified scheme for radio-loud AGN which is based on the two main parameters of the model, the radio luminosity and the viewing angle, i.e. the flatness of the spectrum (Faranoff and Riley, 1974) [26]:

- FR II galaxies are powerful ($L_{178\mathrm{MHz}} \geq 2 \cdot 10^{25}\,\mathrm{W\,Hz^{-1}}$) radio galaxies when observed edge-on and appear as flat-spectrum radio quasars when the viewing angle is small, and
- FR I galaxies are weaker ($L_{178\mathrm{MHz}} \leq 2 \cdot 10^{25}\,\mathrm{W\,Hz^{-1}}$) radio sources appearing as BL Lacs when seen pole-on.

The name blazar now denotes the radio-loud AGN of both types *if their jet axis is close to the line of sight.*
Radio-quiet AGN and Seyfert galaxies with their lack of strong radio emission have the same morphological structure (black hole and accretion disc), but are interpreted as objects with non-relativistic jets due to a larger mass loss rate [27].
Having understood the radio behavior of AGN, the questions concerning their γ-ray emission up to TeV energies remain unanswered, together with the question what actually is injected into the jet and how. In fact, both questions correlate.
As reported above, EGRET has shown that many flat-spectrum radio sources are also strong γ-ray emitters, and the Whipple and HEGRA Čerenkov telescopes detect Mrk 421 and Mrk 501 up tp 10 TeV. Although it is not possible to resolve the origin of the hard X-ray and γ-component, they are certainly associated with the jet. This implies that a small viewing angle to the jet axis is crucial for high energy detection. Nevertheless, it is not a priori obvious what the mechanism for γ-ray emission is, as the synchrotron emission of relativistic electrons in the jet mainly emerges in the radio-to-optical regime and does not reach to hard X-rays.
As an example, Fig. 2.6 shows the multifrequency spectrum of the blazar Mrk 421. It has a shape typical for blazars; the flat radio spectrum is followed by a steepening of the spectrum in the optical-to-soft-X-ray region. The flux increases again in the hard X-ray region and reaches a second (rather bumpy) maximum at GeV energies. Note that the data combined for this spectrum are taken non-simultaneously, so flux

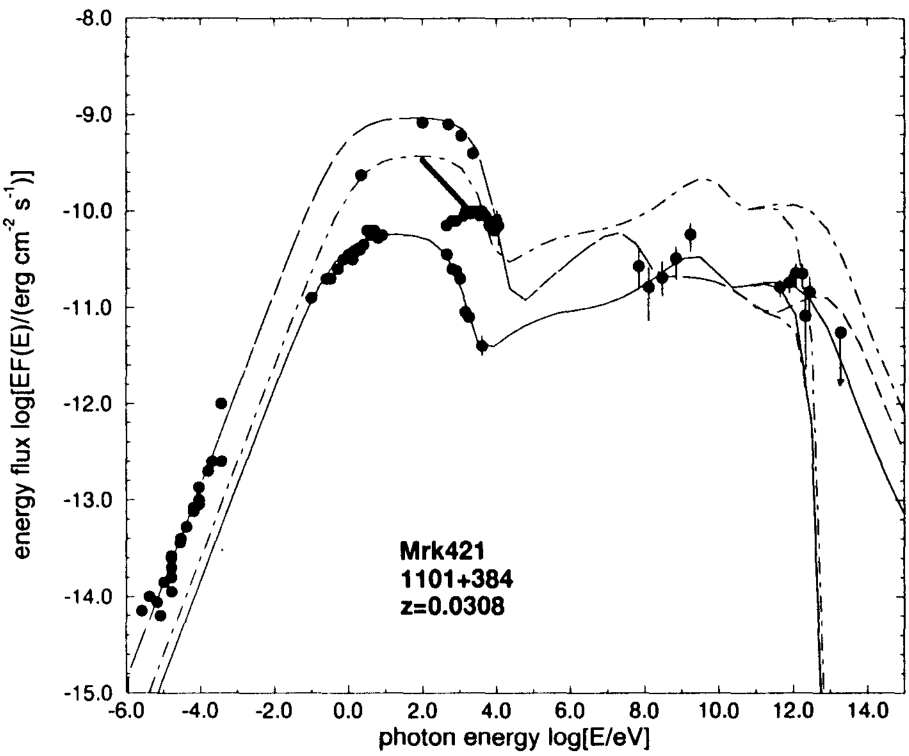

Figure 2.6: **Multifrequency spectrum of the blazar Mrk 421. The flux prediction is based on the proton blazar model taking into account cosmic and internal absorption (see text). Taken from [11].**

variations of more than one order of magnitude are visible e. g. in the optical region. Whereas there is general agreement as to synchrotron emission of relativistic electrons shaping the spectrum up to soft X-rays, the origin of the higher energy spectral components is still subject of lively debates.
γ-energies above 10^5 eV may be explained both by inverse-Compton up-scattering of optical-to-ultraviolet photons and by synchrotron-self-Compton scattering, i. e. Compton scattering of synchrotron photons off the same relativistic electrons which produced them [28]:

$$e^- \, \gamma_{UV} \longrightarrow \gamma \, e^- \quad (2.16)$$
$$e^- \, \gamma_{synch} \longrightarrow \gamma \, e^- \quad (2.17)$$
$$(2.18)$$

The energy of Compton scattered photons is $E_{IC} \simeq E\,\gamma_e^2$, thus energies up to 100 GeV are easily obtained in this way. Nevertheless, both mechanisms fail to explain the spectra of sources with a γ-ray luminosity L_γ *exceeding* the optical luminosity L_{opt}. L_γ is proportional to the luminosity of the synchrotron-self-Compton mechanism, L_{SSC}, and thus depends on the magnetic energy density u_B. On the other hand, L_{opt} is proportional to the synchrotron luminosity L_{syn}, which depends on the photon energy density u_{rad}, so

$$\frac{L_\gamma}{L_{opt}} \propto \frac{L_{SSC}}{L_{syn}} \simeq \frac{u_{rad}}{u_B} \tag{2.19}$$

implies that for $L_\gamma > L_{opt}$, the condition $u_{rad} > u_B$ must be fulfilled.
This is in contradiction to $u_B \geq u_{rad}$, which is required to explain the acceleration of the particles by statistical Fermi or drift mechanisms: for $u_{rad} > u_B$, the particles would simply escape the magnetic confinement.
In addition, inverse-Compton scattering needs a high photon density to produce the observed fluxes at GeV energies. This implies that the processes have to take place very close to the black hole, where the photon density is higher than further along the jet. On the other hand, a high photon density also means a high degree of self-absorption by $\gamma\,\gamma$-collisions, which again counteract the γ-emission at high energies. Models based solely on electron acceleration and inverse-Compton upscattering therefore inevitably reach their maximum energy at about 1 TeV.
A very promising (but still controversial) solution comes from *adding protons* to the standard Blandford and Königl model of compact relativistic jets. If, apart from the electrons, a certain amount of protons enters the jet, they are accelerated up to very high energies, as the main cooling process for high energy protons, pion production via collisions with matter, is negligible because the matter density in radio jets is low. Biermann and Strittmater showed in 1987 [29] that indeed the protons reach energies of 10^3 PeV (assuming magnetic fields of $\simeq$10 G in the jet). At these energies, photoproduction of pions and e^+e^--pairs (via $\Delta(1232)$) is the dominant cooling process:

$$p\,\gamma \longrightarrow \pi^0\,p \tag{2.20}$$
$$p\,\gamma \longrightarrow \pi^+\,n \tag{2.21}$$
$$p\,\gamma \longrightarrow e^+\,e^-\,p\ . \tag{2.22}$$

The $e^\pm$-pairs immediately lose energy by synchrotron radiation, the neutral pions decay via $\pi^0 \to \gamma\,\gamma$, and the charged pions produce positrons via muon decay, thus an electromagnetic cascade is induced in the jet. If the energy of the γ-rays is above the critical value E_{crit} with $\tau_{\gamma\gamma}(E_{crit}) = 1$, i. e. the optical depth $\tau_{\gamma\gamma}$ exceeds 1, they produce $e^\pm$-pairs via $\gamma\,\gamma \to e^+\,e^-$, which again produce γ-rays. This cascade-cycle is repeated several times until the energy of the γ-rays is below E_{crit}. Now the jet is no longer opaque and the high energy γ-rays escape.
As an important difference from models explaining the high energy spectral component by synchrotron-self-Compton scattering, this PROTON BLAZAR MODEL [12, 30] predicts source spectra reaching TeV γ-rays.
A crucial question of course is whether protons are actually present in the jet plasma. If we assume that the jet originates as a hydromagnetic wind ejected by the accretion flow, then the plasma is of the same composition as the plasma falling onto the black hole, with protons being the most abundant baryon.

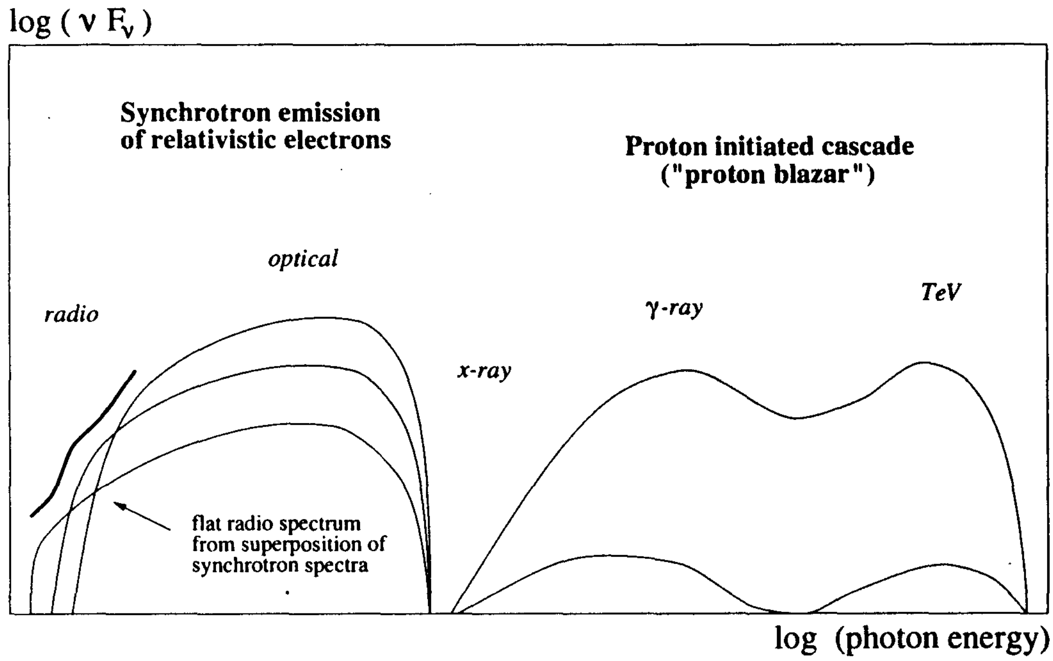

Figure 2.7: **Schematic of typical blazar spectra.**

For a simple comparison of the proton-initiated cascade luminosity L_{pic} to the synchrotron luminosity L_{syn} we calculate the ratio L_{pic}/L_{syn}. The luminosity is directly proportional to the energy densities u_p and u_e of the particles involved in the corresponding process (protons for L_{pic} resp. electrons for L_{syn}) and anti-proportional to the cooling times t_p and t_e of the particles, thus

$$\frac{L_{pic}}{L_{syn}} \simeq \frac{u_p}{u_e}\frac{t_e}{t_p}. \tag{2.23}$$

With $\xi = t_e/t_p$ and $\eta = u_p/u_e$, we obtain

$$L_{pic} \simeq \eta\xi L_{syn} , \tag{2.24}$$

so in case of $\xi \simeq 1$ at the beginning of a newly formed shock (see e. g. [11]) the proton cascade luminosity exceeds the synchrotron luminosity by the energy density ratio η which can be relatively large: $\eta \simeq 100$ holds for the Milky Way and the interstellar space and may also be true for the jets. In fact, $\eta \simeq 100$ could be a universal constant: the proton blazar model fitting in with multifrequency spectra of several nearby blazars [11] support this assumption.

A scheme of a typical blazar spectrum is shown in Fig. 2.7. The shape of the multifrequency spectrum with its two characteristic bumps is interpreted as the combination of the synchrotron (radio to ultraviolet) and the proton blazar radiation (X-ray to γ-rays).

Electron synchrotron spectra with increasing self-absorption cutoff are produced dur-

ing the propagation of a shock along the jet. Their superposition yields a flat radio-spectrum ($S_\nu \simeq const.$) and steepens in the optical- to X-ray region ($S_\nu \propto \nu^{-1}$). Now the proton blazar spectrum sets in, rising as $S_\nu \propto \nu^{-0.5}$ and steepening to $S_\nu \propto \nu^{-1}$ in the MeV to GeV region. Above TeV, the absorption of γ-rays by low energy synchrotron photons leads to further steepening of the spectrum ($S_\nu \propto \nu^{-2}$). Apart from this intrinsic absorption effect, interaction with the cosmic infrared background photons (see next section) exponentially cuts off the spectra somewhere above 10 TeV.
The bumpy structure of the proton blazar spectrum is a consequence of the different γ-production modes in proton blazars: the γ-rays produced by the cascade processes following the photo-production do not leave the jet simultaneously but in generations, i.e. whenever the individual γ-ray energy drops below the pair-production threshold and the jet becomes transparent. The total spectrum is a superposition of several cascade generations.
The time behavior of blazars correlates with the propagation of the shocks along the jet. A typical outburst starts with optical to ultraviolet emission when the shock enters the jet at the basis. At this time there is no radio emission, as the synchrotron self-absorption cutoff frequency

$$\nu_{cut} \simeq 2 \left(\frac{R}{1\text{pc}}\right)^{-\frac{5}{6}} \text{GHz} \tag{2.25}$$

does not allow radio emission until the jet radius R is of the order 1 pc, i.e. until expansion of the dense plasma makes it transparent for radio emission. Thus the outburst shows up delayed in the radio region.
The γ-emission is closely related to the optical outburst, as infrared-to-optical photons are the main targets for proton-initiated cascades. The only (short) delay may arise from the photon-production cooling time and the proton acceleration time. As an important consequence of the dependence of the proton blazar on the target photons, the γ-ray fluctuations are larger in amplitude than the optical fluctuations: the γ-ray flux is proportional both to the proton and the target photon energy, so the dependence on energy variations is quadratic rather than linear.
Multifrequency observations of nearby blazars are supposed to check this outburst scenario. The coordination of observation campaigns simultaneously covering the whole spectrum from the radio- to the TeV-region therefore is of great importance.
In addition, any detection of blazars above some 10 TeV would be a strong support for the proton blazar model, as this region is not within reach of simple synchrotron-self-Compton models.

2.2 Traversing the cosmic background

2.2.1 Extragalactic Background Radiation

The EGRET detection of a large number of flat-spectrum radio galaxies at GeV energies is a guideline where promising sources at energies above 10 TeV may be found. Doppler boosted emission in blazar jets with small viewing angle to the observer is a

crucial requirement for γ-rays at these energies.
The first blazar to be discovered at 10 TeV, Mrk 421 at $z = 0.033$, nevertheless is one of the weakest EGRET sources, and strong GeV sources like 3C 279 at $z = 0.54$ have not been found at TeV energies. A blazar morphology is thus necessary, but not sufficient, and cannot be the only criterion we have to consider on the way to a source catalogue. The most likely reason why powerful but distant AGN like 3C 279 are not detected with current γ-ray telecopes is that TeV γ-rays on their way to the observer are absorbed in external photon background fields.
The propagation of high energy particles over cosmic distances is one of the most important topics of astroparticle physics. On their way between source and observer, cosmic rays traverse magnetic fields and interact with the diffuse radiation background, which is a complex mixture of photons from all wavelength regions, ranging from the radio to ultra-high energy photons. The radiation background is not at all homogeneous, and quite a lot of physically different contributions are summarized by the term "diffuse": often enough, true extragalactic components of the background can hardly be distinguished from Galactic contamination, or unresolved point sources significantly contribute, as e. g. in the X-ray and cosmic ray region.
Our present day knowledge on the radiation background is rather incomplete. Whereas e. g. the microwave background is very thoroughly analyzed, other parts like the infrared are very difficult to probe, and measurements at these wavelengths suffer from great uncertainties.
After a short outline of the different components of the extragalactic background radiation, the rest of this section will concentrate on those regions relevant for the propagation of 50-100 TeV cosmic ray photons through the extragalactic space, as this is the γ-energy for which HEGRA has been designed.
Measurements of the diffuse radiation background covering 30 orders of magnitude in energy are compiled in Fig. 2.8, which is taken from the review by Ressell and Turner [31]. Note that the wavelength λ is connected to the energy ϵ of the background photon via

$$\epsilon = \frac{2\pi\hbar}{\lambda} = 12.4 \left[\frac{100\,\mathrm{nm}}{\lambda}\right] \mathrm{eV}. \tag{2.26}$$

By order of background photon energy, the diffuse radiation has the following ingredients:
In the RADIO ($10^{-8}\,\mathrm{eV} - 10^{-6}\,\mathrm{eV}$), the diffuse background is comprised from two components, the synchrotron radiation both from the disc and the halo of our Galaxy, and the emission from unresolved extragalactic radio galaxies. As these components cannot be separated even when observing the region around the north Galactic pole, measurements at these energies must be regarded as upper limits on the extragalactic radiation background.
The MICROWAVE ($10^{-6}\,\mathrm{eV} - 10^{-2}\,\mathrm{eV}$) region is dominated by the cosmic microwave background radiation which is interpreted as the relic of the big bang, representing the temperature of the universe at the moment of last scattering, redshifted by a factor of 1100. Due to the cosmological impact, this part of the radiation background is intensively studied, and the energy flux is very well known [32, 33] to be a black body spectrum of temperature $T = (2.74 \pm 0.02)\,\mathrm{K}$ [33].

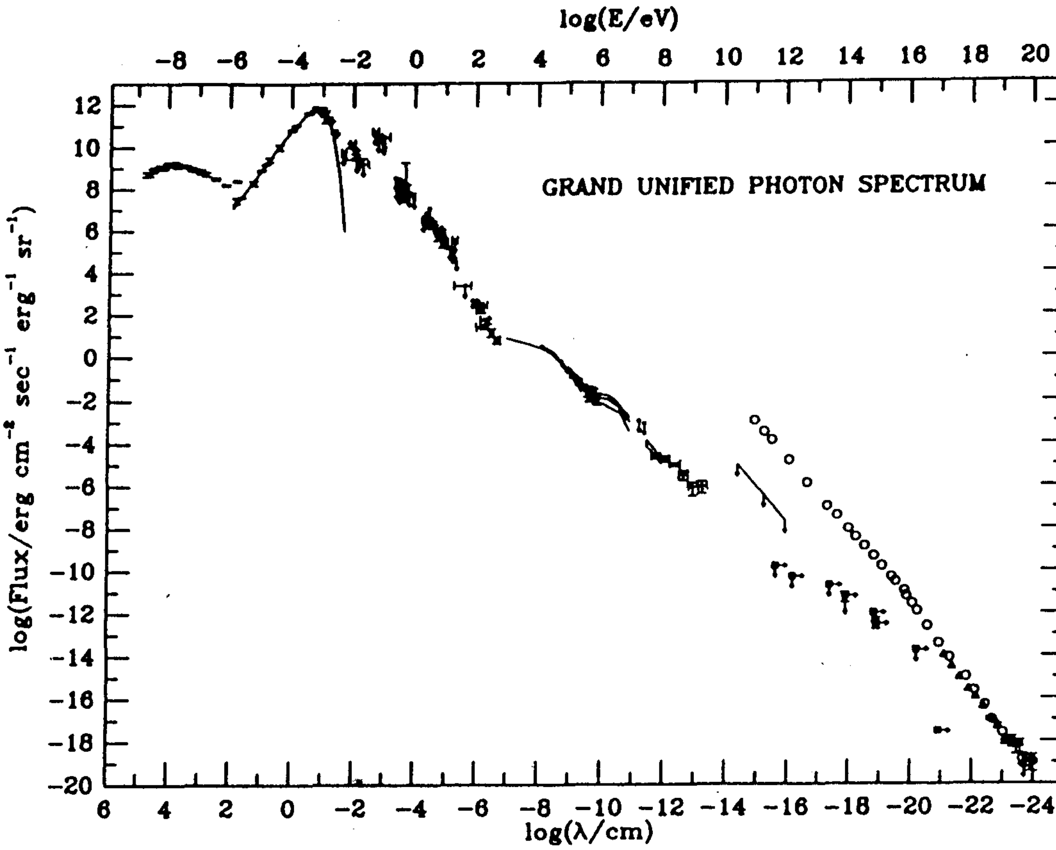

Figure 2.8: **The background photon spectrum, taken from [31].**

The most important part of the radiation background both for TeV cosmic ray physics and cosmology is the INFRARED (10^{-2}eV – 1 eV). It comprises infrared emission of nearby galaxies as well as optical emission at distances $z \geq 2$ redshifted to the infrared. This makes the infrared background a probe of galaxy formation and evolution, as emission of evolving galactic systems in the early phase of galaxy formation should show up in the infrared by now [34]. Direct measurements of this background are difficult, especially as both Galactic and zodiacal contamination and strong foreground from interplanetary and interstellar dust emission exceed the cosmological component by orders of magnitude. They have to be modelled and subtracted, a method which can hardly avoid large systematic errors. Nevertheless, a tentative measurement has recently been published by the COBE satellite experiment [35] and will be described at the end of this section.

Due to the expansion of the universe, the energy of all components of the background radiation is a function of redshift z resp. of time. Both radio and infrared-to-optical background are tied to the evolution of the corresponding sources, i. e. radio and normal galaxies [36].

The OPTICAL and ULTRAVIOLET (100 eV – 10^5 eV) part of the background is again difficult to probe, as stars in the field of view, zodiacal light and radiation from the interstellar gas dominate the measurements. An optical component of the diffuse background radiation therefore has not been detected up to now, and Ressell and Turner quote only upper limits.
In contrast to this, the extragalactic X-RAY and γ-RAY background (1 keV – 100 MeV) is very well known and can be described by simple power laws. It is made up in unknown relative portions by quasars and Seyfert galaxies, i. e. *discrete* sources, and most probably by a hot diffuse plasma at $T \simeq 10^9$ K, but there is no consensus on this point [37].
The region above 100 MeV γ-ray energy may be summarized as the COSMIC RAY REGION. No measurement of the diffuse flux at cosmic ray energies has been claimed yet, and Galactic contamination is difficult to subtract. COS-B data for the Galactic anti-center region and air shower flux estimations of the overall cosmic ray flux are used as firm upper limits on the extragalactic background radiation.
Applying techniques for separating γ-showers from the bulk of hadronic background, the HEGRA collaboration [31] has recently published an upper limit in the 60-200 TeV region, showing that the γ-flux is at least two orders of magnitude below the limits presented in the compilation of Ressell and Turner [31]. In Chapter 5, a new HEGRA upper limit is given on the basis of the data used in this analysis.

Within the scope of this thesis, which aims at a detection of γ-rays above 50 TeV from extragalactic point sources, mainly the cosmic microwave and the infrared-to-optical background are of great importance. Their effect on traversing γ-rays reaches from (1) absorption of primary photons by e^+e^--pair production with the photons of the radiation background to (2) the creation of e^+e^--cascades [38] and to (3) extended e^+e^--pair halos with radii $\simeq$ 1 Mpc around AGN with high energy γ-ray emission [39]. The latter effect would make AGN appear as *extended* sources rather than as point sources and is a challenge to future high resolution detectors.
The remaining part of this section will give a discussion of these three topics.

2.2.2 Pair production at microwave and infrared background photons

Soon after the discovery of the cosmic microwave radiation, Gould, Schréder [40] and Jelley [41] pointed out that the existence of cosmic photons has an important effect on traversing photons, as pair production via photon-photon-collisions

$$\gamma\,\gamma_{bg} \longrightarrow e^+\,e^- \tag{2.27}$$

leads to absorption of γ-rays above a threshold

$$E \geq E_{thresh} = \frac{2m_e^2}{\epsilon\,(1-\cos\theta)} \simeq 0.5\left[\frac{1\,\mathrm{TeV}}{\epsilon}\right]\mathrm{eV} \tag{2.28}$$

with E denoting the energy of the primary γ-ray, ϵ the energy of the background photon and θ the angle between the photon directions. The average energy of microwave

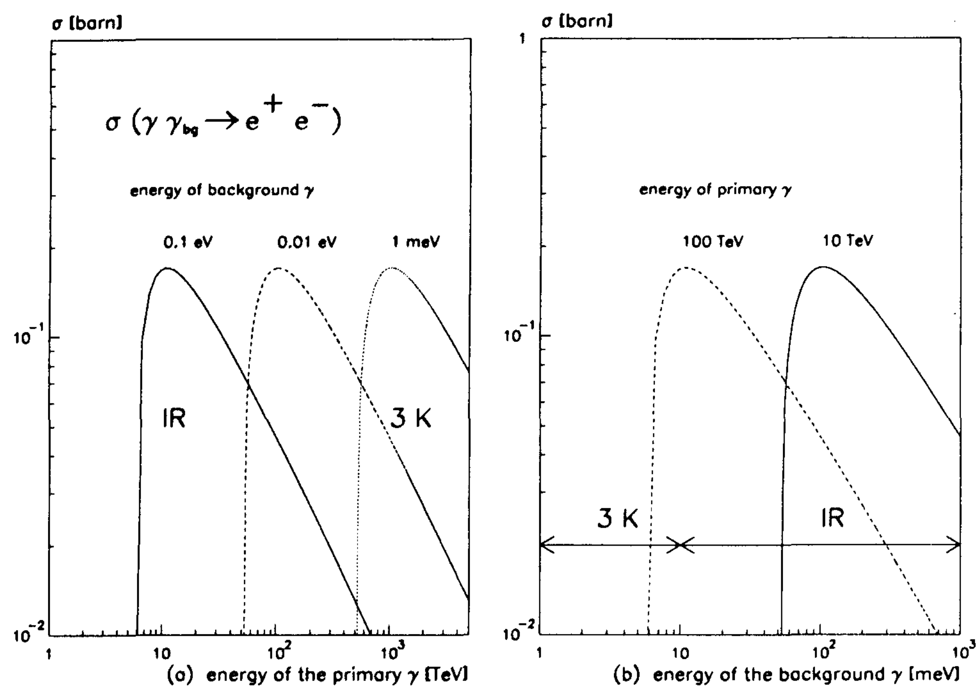

Figure 2.9: **Photon-photon pair production cross section as a function of the energy (a) of the primary cosmic ray photon and (b) of the background photons.**

background photons is 10^{-3}eV, so the corresponding threshold energy is $E_{thresh} \simeq$ 500 TeV (see Fig. 2.9).
The total cross section for this process is given by [42]

$$\sigma_{pp} = \frac{3\sigma_T}{16}\left(1-\beta^2\right)\left[\left(3-\beta^4\right)\ln\frac{1+\beta}{1-\beta} - 2\beta\left(2-\beta^2\right)\right] \tag{2.29}$$

with

$$\beta = \sqrt{\frac{1-2m_e^2}{E\epsilon\left(1-\cos\theta\right)}} \tag{2.30}$$

being the velocity of the outgoing electron in the center-of-mass system and σ_T being the Thomson cross section. Fig. 2.9 (a) shows the cross section as a function of the energy of the primary cosmic ray photon for various energies of the background photon. As the cross section peaks near the threshold, the microwave background photons at energies $\epsilon = 10^{-2} \ldots 10^{-3}$ eV will interact with γ-rays with energies above 100 TeV, whereas the propagation of primaries with energies between 1 and 100 TeV is affected by the infrared background radiation. This is illustrated in Fig. 2.9 (b), where the cross section is shown as a function of the background photon energy. For 100 TeV primaries, the cross section peaks at $\epsilon \simeq 10^{-2}$ eV, whereas for 10 TeV primaries, infrared background photons of energy $\epsilon \simeq 0.1$ eV, corresponding to $\lambda = 10\,\mu$m, will

contribute most to the absorption.
The search for extragalactic point sources at HEGRA energies thus crucially depends on the actual strength of the MICROWAVE and INFRARED background radiation, and to estimate the amount of photons lost due to absorption on the way from the source to the observer, we have to focus on background photon energies $1\,\mathrm{meV} \leq \epsilon \leq 1\,\mathrm{eV}$.
If $n(\epsilon, z)$ is the number density of background radiation photons at redshift z, the so-called OPTICAL DEPTH τ for attenuation between the source at z_s and the observer is given by

$$\tau(\epsilon, z) = \frac{1}{2H} \int_0^{z_s} (1+z)^{-2} (1+2qz)^{-\frac{1}{2}} \, dz \int_{-1}^{1} (1-\cos\theta) \, d\cos\theta \int_{\epsilon_{thresh}}^{\infty} n(\epsilon, z) \sigma d\epsilon \tag{2.31}$$

with H being the Hubble constant and q the deceleration parameter. Provided $n(\epsilon, z)$ is known, the optical depth for a source at given redshift z can be calculated, and it is possible to estimate at what distance z the universe becomes opaque for γ-rays ($\tau_{\gamma\gamma} \geq 1$). This will restrict the part of the universe visible for HEGRA to sources with a redshift below a certain maximum value z_{max}, and the catalogue of possible sources depends on the actual value of z_{max}, as the flux dN/dE from sources is reduced rather drastically like

$$dN/dE \propto e^{-\tau(E)}. \tag{2.32}$$

A modelling of $n(\epsilon, z)$ is quite easy for the microwave background, where the number density is given by a black-body spectrum

$$n_{3K}(\epsilon) = \frac{8\,\pi}{(2\,\pi\,\hbar)^2} \frac{\epsilon^2}{(e^{\epsilon/kT} - 1)} \tag{2.33}$$

with $T = (1+z)\,2.7\,\mathrm{K}$ (see Fig. 2.10).
For the infrared background, the evolution of the radiation with time is considerably more complicated. Radiation produced at a time corresponding to a redshift z is cooled by a factor $(R(z)/R(0))^3 = (1+z)^3$ due to the expansion of the universe from radius $R(z)$ to the present value $R(0)$. In addition, as mentioned before, the production rate of infrared photons is a function of time and can be expressed as a luminosity evolution function $f(z)$ [43], leading to a photon density

$$n(\epsilon, z) = (1+z)^3 n(\epsilon, 0) f(z). \tag{2.34}$$

Here, $f(z) = 1$ corresponds to the case of all infrared photons being produced before the z in question, a situation which is true for the 3 K photon background. In the infrared, this is obviously only part of the truth, as not all of the infrared background photons are of cosmological origin; but dealing with sources at low redshifts ($z \leq 0.1$) and attributing most of the infrared background to an early era of active galaxy formation at $z \geq 2$, the cosmological scenario is a good approximation even in the infrared [38]. In fact, $n(\epsilon, z) \propto (1+z)^3$ seems to describe correctly faint blue galaxies, thus indicating that *strong* evolution either in luminosity or density is indeed a feature of these objects [44], but no evolution is found e. g. for normal galaxies up to $z \simeq 1.5$ [45], so the z-dependence may be shallower, i. e. $n(\epsilon, z) \propto (1+z)^k$ with $k \leq 3$. Modelling the

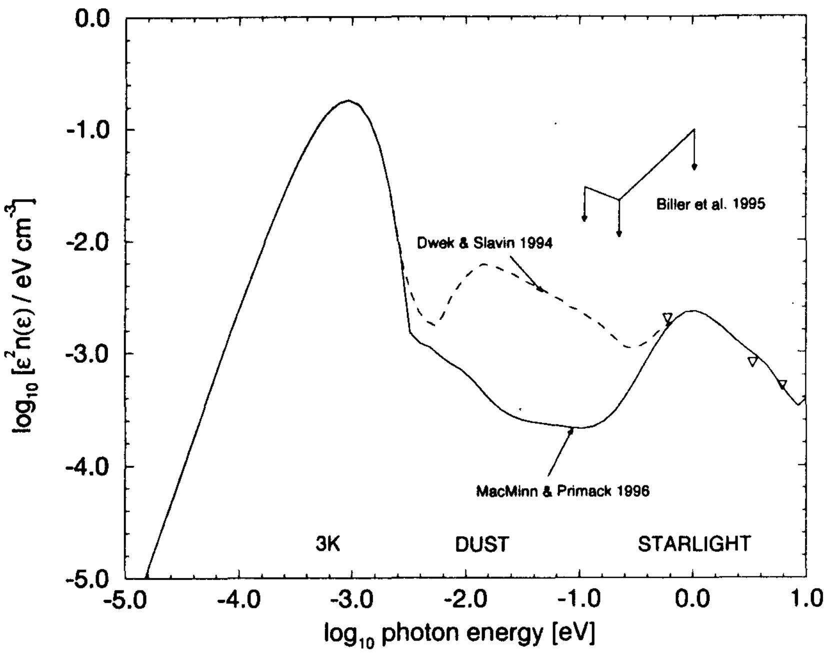

Figure 2.10: **Diffuse background radiation from microwave to optical wavelengths including two estimations of the infrared background (see text). Taken from [11].**

(unknown) history of galaxy formation and evolution is therefore crucial for getting an estimate on $n(\epsilon, z)$ in the infrared. MacMinn and Primack [46] have calculated the infrared background assuming various scenarios of galaxy formation and claim that the era of galaxy formation is the dominant factor influencing the background which is thus a powerful tool for probing this era. In fact, this has a strong cosmological impact, as the possibility of distinguishing between early and late galaxy formation may help to decide on dark matter models: whereas cold dark matter (CDM) models imply early galaxy formation ($1 \leq z \leq 3$), a late galaxy formation ($0.2 \leq z \leq 1$) is favored by cold and hot dark matter (CHDM) models. The basic difference in the mechanisms is the velocity of the cold or hot dark matter particles: whereas CDM (e. g. WIMPS, MACHOS, or supersymmetric particles) has *low* velocity and hence reinforces structure formation via gravity, HDM (light axions, massive neutrinos) has a *large* velocity which counteracts and thus delays the formation of structures. In CDM models, about 30 % of the background flux comes from sources at $z > 2$, whereas a contribution of only 1 % is predicted in CHDM models.
Fig. 2.10 shows the infrared background photon density as calculated by MacMinn and Primack, averaging various CDM and CHDM models. The resulting prediction of the background strength is considerably smaller than a tentative measurement by Stecker et al. [9] and Dwek and Slawin [10] based on the Whipple data for Mrk 421, shown as

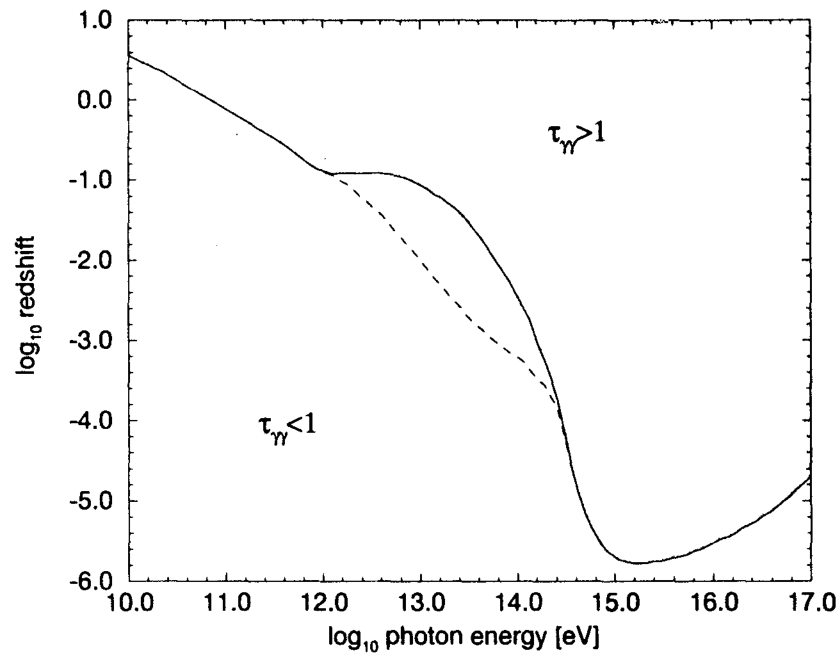

Figure 2.11: **γ-ray horizon $\tau(E,z) = 1$ as a function of the energy of the primary γ-ray. The dashed and dotted lines correspond to the different estimations on the infrared background shown in Fig. 2.10. Taken from [11].**

dashed line in Fig. 2.10. Upper limits from Biller et al. [47] at photon energies from 0.1 to 1 eV are also based on the spectrum of Mrk 421.

Recently, results based on data taken with the Michelson interferometer FIRAS (Far Infrared Absolute Spectrometer) on board the COBE (Cosmic Background Explorer) satellite have been published [35]. After modelling and removing interplanetary and interstellar dust components, a significant positive value remains at all wavelengths which is interpreted as a diffuse infrared background with density $\epsilon^2 n(\epsilon) = 1.0 \cdot 10^{-3}\,\mathrm{eV\,cm^{-3}}$ at $1.2 \cdot 10^{-2}\,\mathrm{eV}$. Within the uncertainties, this value is equal to the far-infrared flux predicted by MacMinn and Primack.

From the background modelling in Fig. 2.10, the γ-ray horizon $\tau(E,z) = 1$ is calculated, assuming $\Omega = 1$, $H_0 = 75\,\mathrm{km\,s^{-1}\,Mpc^{-1}}$ and strong evolution ($k = 3$), and shown in Fig. 2.11. The ambivalence due to the uncertainty in the actual strength of the infrared background is indicated by the dashed and solid line, corresponding to Fig. 2.10.

There are several results: apart from the well-known microwave background providing a cut-off for γ-rays above 100 TeV, the infrared background makes the universe opaque for sources with distances above $z = 0.1$ even at 50 TeV and even with the most optimistic assumption about the strength of the infrared background. Candidates for

emission at HEGRA energies are only very nearby sources with redshifts well below $z = 0.1$, as Mrk 421 and Mrk 501 at $z \simeq 0.03$.
Fig. 2.11 also suggests that the analysis of the spectra of sources at different redshifts and at different energies is a a tool for probing the infrared background. If it is possible to detect a cutoff due to external absorption for several sources up to $z = 0.5$, present-day Čerenkov telescopes with their threshold energy of of 0.5 to 1 TeV may help to pin down the actual strength of the diffuse infrared radiation. Detailed knowledge of the intrinsic source spectra is nevertheless crucial, as otherwise it is impossible to separate the cutoff due to external absorption from the intrinsic steepening of the source spectrum. The claimed measurement of the infrared background by fitting an exponential cutoff to the Whipple spectrum of Mrk 421 as done by Stecker et al. [9] is in fact only an upper limit if the source spectrum itself steepens above TeV, as recent measurements with the HEGRA Čerenkov telescopes indicate [48].

2.2.3 Cascading

At initial energies above TeV, we are dealing with the extreme relativistic case. As a consequence, so-called cascade processes have to be taken into account [36, 38], which counteract the γ-ray absorption in background radiation fields.
Electromagnetic cascades are mainly driven by pair production and inverse-Compton scattering off background photons,

$$e\,\gamma_{bg} \longrightarrow e\,\gamma \tag{2.35}$$

The cross section for this process is given by the Klein-Nishina formula

$$\sigma_{ICS} = \sigma_T \frac{3}{8}\frac{m_e^2}{s\beta}\left[\frac{2}{\beta(1+\beta)}\left(2+2\beta-\beta^2-2\beta^3\right)-\frac{1}{\beta^2}\left(2-3\beta^2-\beta^3\ln\frac{1+\beta}{1-\beta}\right)\right] \tag{2.36}$$

with

$$\beta = \frac{1-m_e^2}{1+m_e^2} \tag{2.37}$$

denoting the velocity of the outgoing electron in the center-of-mass system. In contrast to photon-photon pair production, this process has no threshold energy.
At center-of-mass energies $s \gg m_e^2$, almost all of the energy in a pair production process is transferred either to the electron or the positron. If this particle Compton-scatters off a background photon, the energy is almost totally carried away by the photon which may thus end up with nearly the energy of the initial source photon. This so-called CASCADE CYCLE of pair-production followed by inverse-Compton scattering significantly slows down the attenuation if extragalactic magnetic fields are not too strong. In case the synchrotron loss rate exceeds the rate of upscattering processes, this cascade effect is suppressed.
Taking into account pair-production/Compton cascades, Protheroe and Stanev [38] have simulated the propagation of TeV γ-rays from sources with E^{-2}-spectra and shown that the cascade process significantly increases the observable flux compared to the flux with absorption only. Nevertheless, the cutoff energy of γ-rays due to the

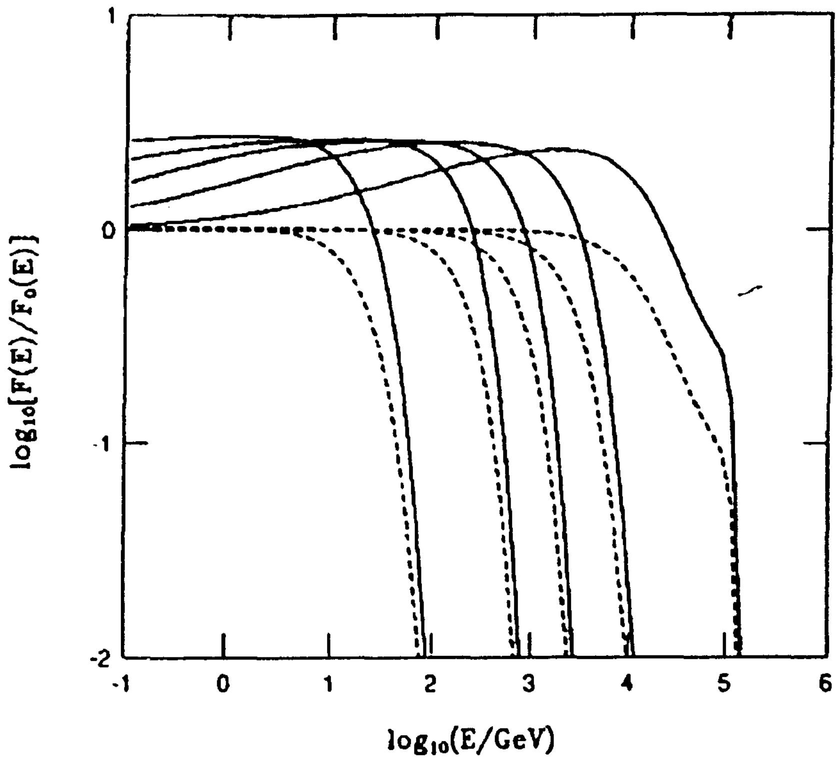

Figure 2.12: **γ-ray spectrum at Earth $F(E)$, expected from sources at $z = 0.0033$, $z = 0.031$, $z = 0.158$, $z = 0.54$, and $z = 2.16$, emitting an E^{-2} spectrum. $F_0(E)$ is the spectrum without background radiation fields. The results with (solid lines) and without cascading (dashed line) are shown. Taken from [38]).**

infrared absorption is only increased by the factor 2. At very small redshifts ($z \leq 0.01$), the pile-up due to the cascade process is in the $1 - 10\,\mathrm{TeV}$ region, with a shift to lower energies at higher redshifts.

For production spectra with a spectral index steeper than 2, the effect of cascading is decreased as less energy is injected in the region where interaction with background photons occurs. At GRO energies of some GeV, cascading reaches its maximum and even flattens the source spectra.

Fig. 2.12 shows the γ-ray spectrum $F(E)$ at Earth for sources at different redshifts emitting an E^{-2}-spectrum up to $10^{18}\,\mathrm{eV}$. Dashed lines indicate absorption, solid lines show the increase in flux due to cascading processes [38].

Cascading of course takes place even in case of strong extragalactic magnetic fields, but if the gyroradius of electrons

$$g_e \simeq 100 \left[\frac{E}{100\,\mathrm{TeV}}\right] \left[\frac{B}{10^{-9}\,\mathrm{G}}\right]^{-1} \ \mathrm{pc} \tag{2.38}$$

is smaller than the inverse-Compton cooling length

$$\Lambda \simeq 4 \cdot 10^3 \left[\frac{E}{100\,\mathrm{TeV}}\right]^{-1} \ \mathrm{pc}\ , \tag{2.39}$$

the direction of the upscattered background photon is not sufficiently correlated to the direction of the initial TeV γ-ray. The intergalactic magnetic field strengths are in fact only marginally known. Vallée [49] gives an upper limit of $6 \cdot 10^{-12}$ G, but points out that the true value might be much lower. Directional information of the primary γ is in fact only conserved if the magnetic field strength is less than 10^{-14} to 10^{-15} G [38]. As an interesting consequence of their dependence on magnetic fields, cascade processes and the time dilatation of TeV-γ-rays due to the increased propagation way have recently been suggested as a method of probing extragalactic magnetic fields [50].
Theoretical predictions of the flux increase due to cascading processes [38] indicate that the effect plays a major role only at energies from GeV to 1 TeV, but as they all depend on our weak knowledge on the infrared-to-optical background radiation, the cascade effect may well be relevant even at energies above some TeV.

2.2.4 Pair halos

The cascade processes described in the previous chapter may have a very interesting effect on the observation of TeV point sources, as pointed out by Aharonian, Coppi, and Völk [39].
As shown before, γ-ray primaries above 100 TeV are not directly visible as they interact with the microwave background photons. Assuming a blazar emitting γ-rays with energies well above 100 TeV, the small photon-photon interaction length will lead to a cascade on microwave background photons in the neighborhood of the sources (length scale $\simeq 1$ Mpc). In a second step, the Compton-upscattered photons and the source photons with $E \leq 100$ TeV will again cascade both in the microwave and the infrared background, according to their energy. As a consequence, the blazar is surrounded by a HALO of e^+e^--pairs at a distance of $\simeq 1$ Mpc. Due to magnetic fields, the direction of the e^+e^--pairs is randomized, and the halo radiation is therefore isotropical. Thus the otherwise invisible blazar emission above 100 TeV shows up as isotropic radiation of energies well below the threshold for interaction with the microwave background.
As an important consequence of this second stage γ-emission, the blazar might appear not as a point-like source but as an extended object with an angular size again depending on the unknown infrared-to-optical background field. Using a low and a high background level following [8], Aharonian et al. calculate halo sizes of 0.3° and 3.0° resp. for source distances of about 1000 Mpc (corresponding to $z \simeq 0.3$). A low infrared-to-optical background might therefore show up in a large angular size of blazar emission at energies above 1 TeV.

Although a detection of pair halos is therefore not within reach of current earth-bound detector arrays and Čerenkov telescopes, the process itself might increase the flux from extragalactic sources above some 10 TeV.

2.3 The source sample

In the precedent sections, concepts of a theory-guided search for extragalactic γ-ray emission have been evaluated. As a consequence, the further analysis concentrates on what is expected to be the most promising source type for detection in the TeV region, the *nearby flat-spectrum AGN*.
It is in fact difficult to decide what *nearby* means in terms of redshift, but confronted with Fig. 2.11, even in the most optimistic case of a low infrared absorption field, sources with $z \geq 0.1$ are very unlikely candidates for detection with HEGRA.

Table 2.1: **The blazar sample.**

source	z	name	class	references
0055+300	0.017	NGC 315		[51]
2201+044	0.028		BL	[52, 53]
1101+384	0.031	Mrk 421	BL,OVV	[18, 54, 55, 56, 53]
0430+052	0.033	3C 120.0	OVV	[57, 58]
1652+398	0.034	Mrk 501	BL	[18, 54, 59, 56]
2344+513	0.044		BL	[18, 61]
1514+004	0.052			[51]
1727+502	0.055	I Zw 187	BL,OVV	[18, 54, 56]
0402+379	0.055	4C +37.11		[51]
0116+319	0.059	4C +31.04		[60]
0802+243	0.060	3C 192.0		[51]
1214+381	0.062	MS 12143+38		[60]

The source catalogue, for simplicity called *blazar sample*, is mainly based on the paper by Mannheim et al. [11], which fits the proton blazar model [12] to multifrequency data of 15 nearby flat spectrum radio sources to obtain flux predictions in the HEGRA energy region. The available flux measurements or flux upper limits used to create multifrequency spectra typically cover the whole energy band from the radio to Whipple energies. In the high energy region, ROSAT data from the all-sky survey and preliminary flux limits from Whipple and HEGRA were additionally taken into account. The sample is mainly taken from the compilation of Fichtel et al. [3], which is based on a number of catalogues with emphasis on

- sources with flat or inverted radio spectrum, i.e. with a radio spectral index between 11 cm and 6 cm of $\alpha \leq 0.5$ ($S_\nu \propto \nu^{-\alpha}$)

following the definition of Kühr et al. [62] [5]. The radio spectra for the sources for which sufficient data is available are shown in Fig. 2.13. The sources typically have a radio

[5] $1\,\mathrm{Jy} = 10^{-23}\,\mathrm{erg} / (\mathrm{cm}^2\,\mathrm{s\,Hz}) = 10^{-26}\,\mathrm{J} / (\mathrm{m}^2\,\mathrm{s\,Hz})$

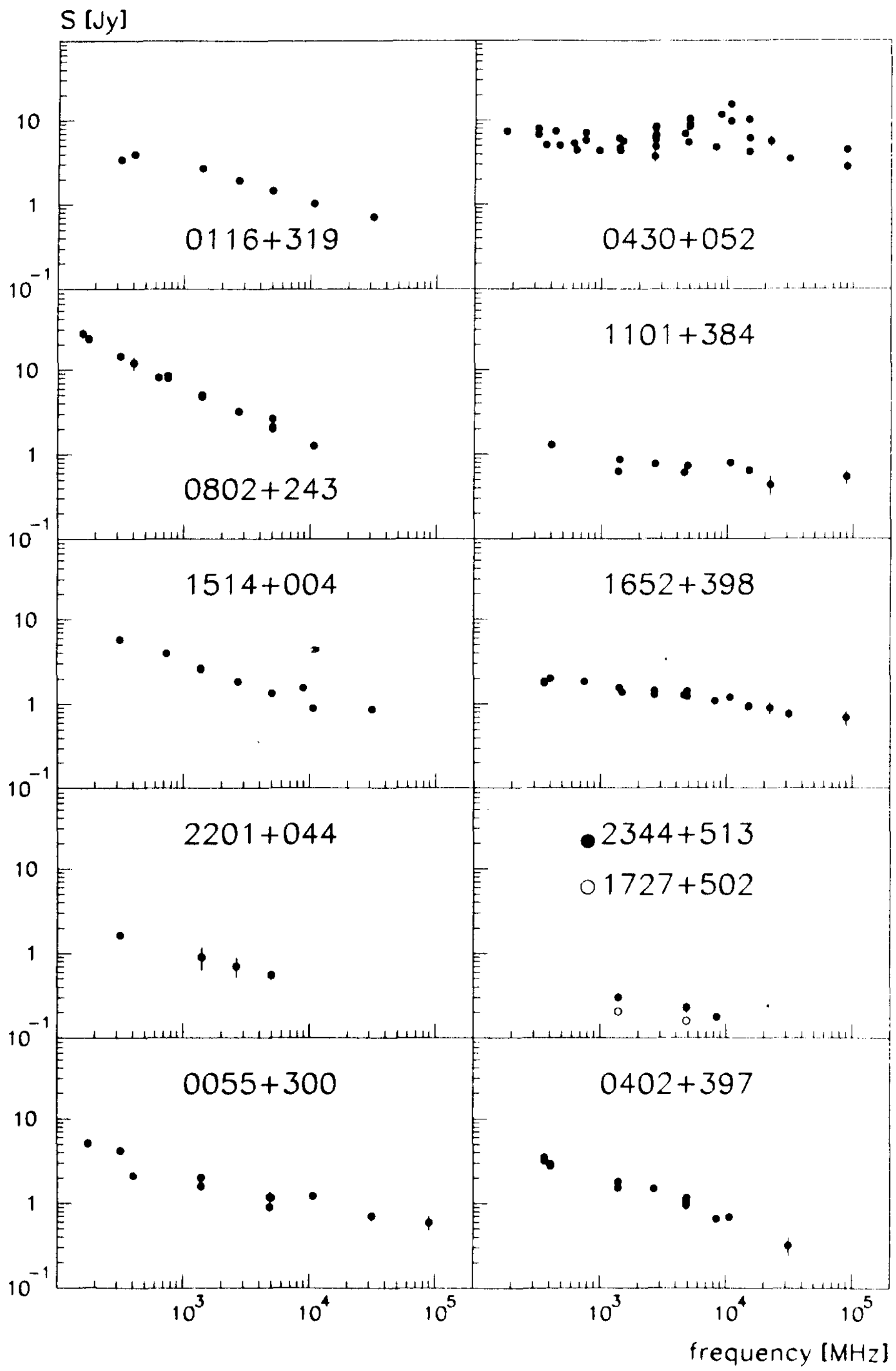

Figure 2.13: **The sources of the blazar sample and their radio spectrum.**

Table 2.2: **The main catalogues.**

NGC	New General Catalogue of Nebulae and Clusters of Stars J. L. E. Dreyer, Sky Publishing Corporation and Cambridge University Press, 1988.
3C 4C	3rd Cambridge Survey of Radio Sources 4th Cambridge Survey of Radio Sources J. D. H. Pilkington, P. F. Scott, Mon. Not. R. Astr. Soc. 69 (1965) 183 and J. F. R. Gower, P. F. Scott, D. Wills, Mon. Not. R. Astr. Soc. 71 (1967) 49
I Zw	Catalogue of Galaxies and Clusters of Galaxies F. Zwicky et al., 1960, California Institute of Technology, Pasadena
Mrk	Catalogue of Markarian Galaxies B. E. Markarian et al., 1967-1977, Astrofis, 3-13
MS	Einstein Medium Sensitivity Survey (EMSS) I. M. Gioia et al., Astrophys. J. Suppl. Ser. 72 (1990) 567

flux $\gtrsim$ 1 Jy.
Most of the sources are BL Lac objects, which by definition show a

- high degree of polarization and variability at all wavelengths.

References are given in Tab. 2.1, which lists the final source sample after additionally considering the trivial constraint of

- good visibility from the HEGRA location on the northern hemisphere (restricting the source declination to $0° \leq \delta \leq 52°$).

The list is in agreement with the BL Lac compilation of Véron-Cetty and Véron [18], additionally two nearby sources (4C +37.11 and NGC 315) have been added from the catalogue of Stickel et al. [51].
2344 + 513 is taken from the *Einstein Slew Survey* [61], a catalogue of 819 X-ray sources detected with the Einstein Observatory (HEAO 2) [63]. The catalogue gives no redshift, but $z = 0.044$ has recently been measured. The source has been (tentatively) detected with the Whipple Čerenkov telescope. Note that the radio flux of 2344 + 513 is only $\simeq$0.1 Jy, which is considerably smaller than the typical flux of $\gtrsim$ 1 Jy of the sources in the sample.
Although classified as a BL Lac in [18], NGC 1275 (Mrk 1505) has not been added to the source list, as it is a radio galaxy with Sy 2 nucleus. The subluminal radio knots indicate that the viewing angle is rather large. We are thus not observing the BL Lac itself, but the emission from the jet at large radii, which is expected to be much lower than the nuclear jet emission. NGC 1275 therefore does not belong to the catalogue of blazars. In addition, there are some doubts as to the redshift of $z = 0.018$ given in [64], as later measurements failed in finding suited emission lines.
At the time of data analysis, the blazar sample comprises 12 sources with redshift below $z \leq 0.062$. The next blazar with higher redshift which would enter the list is BL Lac itself with $z = 0.069$.

The cut in z is of course somewhat arbitrary: as our knowledge on the infrared background is vague, only the *existence* of a cutoff is sure, but we do not know at which distance the universe actually is opaque for 50 TeV γ-radiation. When analyzing the blazar sample in Chapter 6, the redshift cut has to be re-visited, and we certainly have to check it by including sources with $z \geq 0.062$ in the sample.

Upper limits on individual sources

A small fraction of the sources comprised in the sample have been subject of previous analyses of data taken with several air shower arrays at different locations. Upper limits on the TeV flux mainly exist for Mrk 421, as it was the first source to be discovered above 1 TeV. In addition, the catalogues analyzed in previous point source searches mainly comprised sources observed by EGRET, and in fact Mrk 421 is the only source in the sample which has positively been detected by EGRET.
Tab. 2.3 gives the results of previous searches for blazars from arrays on the northern hemisphere. As they are located at rather different altitudes and considerably differ in their threshold energy, the main characteristics of the most prominent arrays are shortly summarized:

(1) The CASA-MIA detector [65] is a very large array in west central Utah at an altitude of 1460 m with a total area of $2.3 \cdot 10^5\,\mathrm{m}^2$, consisting of 1089 independent scintillator stations with 15 m grid spacing. The energy threshold for γ-showers is 100 TeV. As a very important additional feature, MIA is an associated array of 1024 $2.5\,\mathrm{m}^2$ muon detectors buried 3 m under the ground. The muon threshold energy is 0.75 GeV. MIA allows a γ-/hadron separation based on the estimation of the muon content. While retaining 75 % of the γ-rays, more than 90 % of the cosmic ray background is rejected.

(2) The CYGNUS array [66] at 2134 m altitude in Los Alamos, New Mexico, covers an area of $2.2 \cdot 10^4\,\mathrm{m}^2$. It comprises 108 scintillation counters with an area of $1\,\mathrm{m}^2$ each. The threshold energy for γ-rays e. g. from Mrk 421 is of the order 70 TeV.

(3) The EAS-TOP array [67] is located at 2005 m a. s. l. at Campo Imperatore (Italy) above the Gran Sasso Underground Laboratories. It comprises 35 moduls of scintillation counters with an area of $10\,\mathrm{m}^2$ each, a $12 \times 12\,\mathrm{m}^2$ detector for the muonic and hadronic component, and 8 Čerenkov stations. The array covers an area of about $10^5\,\mathrm{m}^2$.

(4) The Tibet air shower array [68] is located in Yangbajing at a rather high altitude of 4300 m a. s. l. It consists of 49 scintillation counters with an area of $0.5\,\mathrm{m}^2$ on a 15 m grid. Due to the high altitude with an atmospheric depth of $606\,\mathrm{g\,cm}^{-2}$, the threshold energy for γ-induced showers is only about 10 TeV. The Tibet array thus has the lowest threshold energy of all earth-bound scintillation arrays. It is only one order of magnitude higher than the energy threshold of Čerenkov telescopes. As the array is rather small at present, it will be scaled up by a factor of 4 in the near future.

The results on Mrk 421 in the energy range from 100 MeV to 100 TeV are summarized in Fig. 2.14 together with the prediction of the proton blazar model (taken from [11]) including internal and external absorption, and extrapolations from EGRET and HEGRA Čerenkov results. Whereas a simple extrapolation from EGRET to TeV

Table 2.3: **Limits on individual objects from the sample as achieved with various air shower arrays. E_{thresh} is the threshold energy and $\Phi(E \geq E_{thresh})$ is the 90 % (Tibet: 95 %) c. l. upper limit on the integral flux.**

array	source	E_{thresh} [TeV]	separation	Φ [$\mathrm{cm}^{-2}\mathrm{s}^{-1}$]	reference
CASA-MIA	Mrk 421	100	N_μ	$3.5 \cdot 10^{-14}$	[69]
EAS-TOP	Mrk 421	25	-	$1.2 \cdot 10^{-13}$	[70, 71]
		90	-	$3.4 \cdot 10^{-14}$	
		240	-	$7.3 \cdot 10^{-15}$	
		240	N_μ	$8.3 \cdot 10^{-15}$	
CYGNUS	Mrk 421	50	-	$9.0 \cdot 10^{-14}$	[72]
		50	N_μ	$7.5 \cdot 10^{-14}$	
Tibet	Mrk 421	10	-	$8.6 \cdot 10^{-13}$	[73]
		30	-	$1.7 \cdot 10^{-13}$	
HEGRA	Mrk 421	60	-	$1.8 \cdot 10^{-13}$	[74]
scint.	Mrk 501	60	-	$9.9 \cdot 10^{-14}$	
HEGRA	Mrk 421	25	-	$1.2 \cdot 10^{-13}$	[75]
AIROBICC	Mrk 501	24	-	$3.7 \cdot 10^{-13}$	

energies is completely ruled out by flux upper limits from various air shower arrays, flux estimates derived by extrapolating the measurements at 1 TeV to higher energies are still below the sensitivity of current air shower detectors. Experimental data clearly indicate a steepening of the spectrum in the TeV region due to *internal* absorption, but there is still no direct evidence for *external* absorption by photons of the infrared background.
Nevertheless, Fig. 2.14 indicates that with a further improvement of the sensitivity of air shower arrays especially at low energies (Tibet, HEGRA-AIROBICC) we may well be able to detect Mrk 421 and other nearby blazars.
Apart from improving the angular resolution and lowering the energy threshold, γ/hadron separation for suppressing the hadronic background is the most promising way. Tab. 2.3 shows that up to now γ/hadron separation is solely based on N_μ, i. e. on estimating the muon content of air showers. In the next chapters, we will concentrate on methods of improving the signal-to-noise ratio of HEGRA by γ/hadron separation.

The southern hemisphere

The source catalogue in Tab. 2.1 concentrates on sources with good visibility at the HEGRA site. Search for γ-flux from individual blazars has also been performed with various arrays on the southern hemisphere.
The Buckland Park Extensive Air Shower Array on sea-level north of Adelaide has started data taking in the early 1970's. As a striking result of their analysis, the Buckland group reports a steady flux from Cen A (NGC 5128, 1322-425)) [78]. Cen A

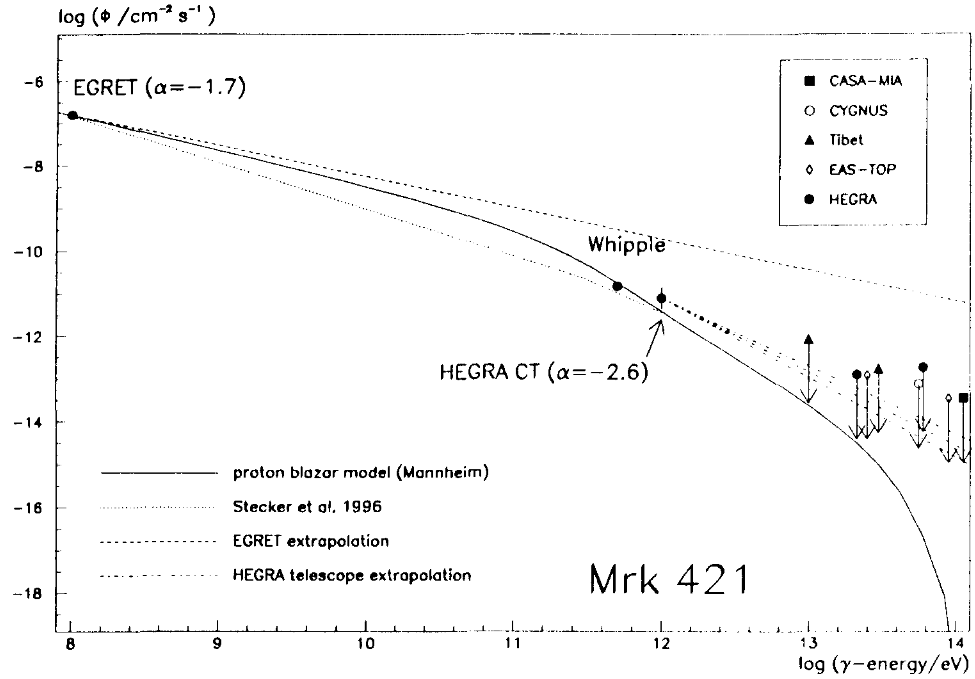

Figure 2.14: **Integral flux measurements and limits for Mrk 421 as a function of the γ-energy. EGRET [5] and HEGRA Čerenkov telescope measurements [48] are shown together with power-law extrapolations, the result of the Whipple group is taken from [76]. The prediction of the proton blazar model (Mannheim [11]) and models based on electron acceleration (Stecker et al. [77]) are included.**

is a very nearby AGN at a distance of approximately 5 Mpc which is known for its rapid variability at radio energies on time-scales of a few days.
The data were taken between 1984 and 1989. During this period, the threshold energy of the array was approximately 100 TeV. The time averaged flux has been estimated to

$$\Phi(E \geq 100\,\mathrm{TeV}) = (7.4 \pm 2.6) \cdot 10^{-12}\,\mathrm{cm}^{-2}\mathrm{s}^{-1} \ , \qquad (2.40)$$

and the data show evidence for a spectral cutoff at 150 TeV, which is consistent with γ-ray absorption by photons of the cosmic microwave background.
The $\simeq 3\,\sigma$ significance of the excess is not compelling, especially as no steady flux has been detected between October 1987 and January 1992 by the JANZOS air shower array [79] at 1635 m altitude. Nevertheless, the JANZOS group reports that during 18 days of high intensity in 1990, a flux excess at the $3.8\,\sigma$ level has been accumulated. This would be in accordance with a high degree of variability of Cen A even at the highest energies.

Chapter 3

Experimental tools

This chapter deals with the challenges and possibilities of high energy γ-astronomy from the experimental point of view. After a short introduction to the physics of extended air showers, the HEGRA (High Energy Gamma Ray Astronomy) array, located 2200 m a.s.l. on the Canary Island La Palma (28.8° N, 17.9° W), is described with restriction to those parts of the multicomponent array which play a major part in the subsequent analysis, i. e. the scintillator array and the Geiger tower sub-array. This tool allows a new and robust γ/hadron separation based on the electromagnetic and muonic component of air showers. The properties of γ- and hadron-induced showers which allow a separation are described in the last section of this chapter.

3.1 Air showers

The differential cosmic ray flux is well described by an inverse power law in energy,

$$\frac{dN}{dE} \propto E^{-(\gamma+1)} \tag{3.1}$$

with $\gamma = 2.67$ [80] being the spectral index. As the flux is thus rapidly decreasing with energy, it is obvious that different types of detectors have to be used to probe it. Whereas balloon and satellite experiments with their limited effective area are excellent tools in the >GeV energy region, a large detector size is essential to have a sufficient rate from point sources at energies above TeV, so earth-bound detector arrays have to cover this region. This makes the analysis of the primary cosmic rays considerably more complicated, because the Earth's atmosphere works as a calorimeter of inhomogeneous density, and the relevant properties of cosmic ray primaries have to be reconstructed rather indirectly by detecting the cascade of secondary particles they induce in the atmosphere, the so-called air shower.

The development of a cosmic ray induced air shower is carried by an electromagnetic, a muonic, and a hadronic component. γ-showers are almost purely electromagnetic with alternate pair production and bremsstrahlung being the main process chain. In proton- and hadron-induced showers, additional hadronic cascades lead to subshowers and anisotropies in the shower development and to a considerable muon content from pion and kaon decay,

$$\pi^- \longrightarrow \mu^- \bar{\nu}_\mu \tag{3.2}$$
$$K^- \longrightarrow \mu^- \bar{\nu}_\mu \,. \tag{3.3}$$

Fig. 3.1 shows a computer simulation[1] of the development of showers induced by a primary γ, a proton, and an iron nucleus. The most striking features are the smoothness of the purely electromagnetic γ-induced shower and the rather grainy structure of the hadron-induced showers which is a consequence of the additional muonic and hadronic component. In all shower types, the electromagnetic component dominates by orders of magnitude, as electrons and positrons rapidly multiply. The total number of $e^\pm$ reaches a maximum and decreases quickly afterwards as the energy drops below the critical value for pair production ($\simeq$ 80 MeV). Muons lose energy by ionization only, so their number reaches a maximum and then attenuates slowly.
The shower maximum has a typical altitude of 15 to 30 km depending on the primary energy. Any earth-bound detector array has therefore a severe shortcoming, as it samples the shower at one depth only. Even at high altitude (La Palma 2200 m, Tibet 4300 m), this is well after the maximum. Sophisticated fitting and extrapolation is necessary to gain information about the shower and the primary particle.

3.2 The HEGRA air shower array

The HEGRA air shower array has been built with the aim of detecting directed γ-radiation from galactic and extragalactic point sources and extended regions of γ-emission. It furthermore allows to analyze the chemical composition of the primary cosmic radiation [82] and to observe time variations. As a rather new and challenging scientific goal, the search for burst-like phenomena has been added, as a detection of TeV counterparts might cast some light on the nature of γ-ray bursts [83, 84, 85].
The array covers an area of $180 \times 180\,\mathrm{m}^2$ with a detector sampling density of about 3 % and comprises 4 sub-arrays measuring physically different components of extended air showers.

- The direction of the primary particle is reconstructed by a grid of 243 scintillator huts which measure the arrival time and the lateral distribution of the electromagnetic particles. As described above, this detector component analyzes the shower well below its maximum.

- The grid of 49 open Čerenkov counters AIROBICC (AIR shower Observation By angle Integrating Čerenkov Counters) [86] is able to detect the atmospheric Čerenkov light cone produced by the electromagnetic shower component and thus to reconstruct the direction of the primary particle and – to a certain degree – draw conclusions as to the nature of the primary particle. The Čerenkov light

[1] Here and in the following analyses, the air shower simulation code CORSIKA [81] is used. It is briefly described in the next section.

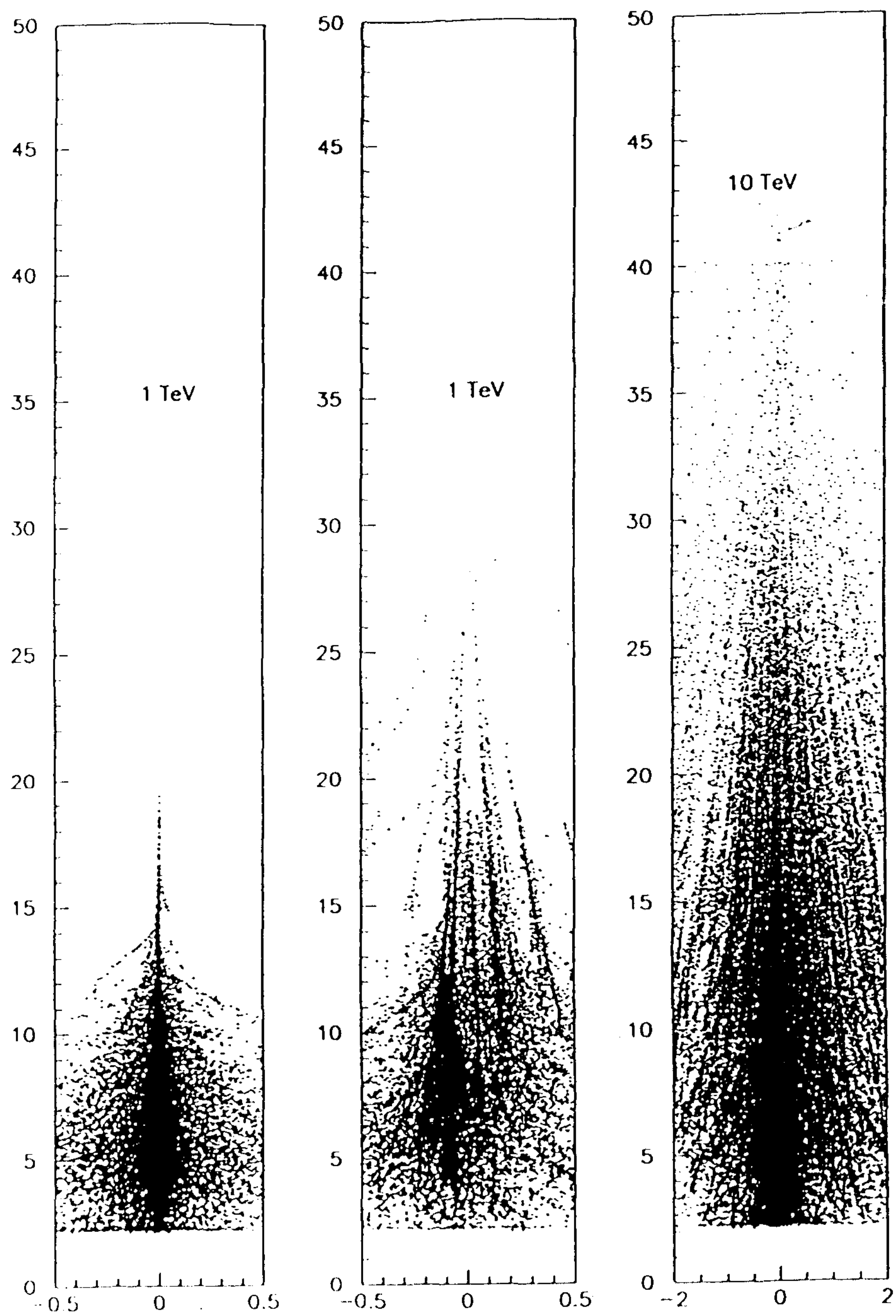

Figure 3.1: Monte Carlo simulation of air showers.

seen by AIROBICC is produced during the whole shower development and only subject to atmospheric absorption. The light density at different distances from the shower core may thus be used to reveal the shower history. Most of the Čerenkov light is naturally produced at the shower maximum, so AIROBICC probes the shower at higher altitudes than the scintillator array.

- The matrix of 17 Geiger towers [87] contributes a measurement of the muon and high energy particle component of the air shower. It gives valid information about the particle energy distribution at different distances from the shower core. Like the scintillator array, it samples the tail of the shower development.
- A system of 6 Čerenkov telescopes [88] allows a theory-guided search for sources. With the first three telecopes in a stand-alone-mode, the discovery of TeV γ-rays from the Crab supernova remnant and the blazars Mrk 421 and Mrk 501 has been confirmed. In addition, γ-rays from the galactic source GRS 1915+105 [89] have recently been detected with a significance of more than $5\,\sigma$ [90].

The present layout of the HEGRA array is shown in Fig. 3.2.

3.2.1 The scintillator array

At the time of data taking for this analysis, the HEGRA scintillator matrix consisted of 167 counters on a grid with 15 m spacing and an additional matrix of 76 counters interleaved to achieve a dense region of 10 m grid spacing in the inner part of the array. Each scintillator counter consists of $1 \times 1 \times 0.04\,\mathrm{m}^3$ of scintillator covered by 4.8 mm of lead absorber which filters low energy electrons and converts a part of the incoming photons into e^+e^--pairs. The main aim is an improvement of the angular resolution of the matrix, as the time spread of the shower front is decreased.
As shown in Fig. 3.3, a fast 5″ photomultiplier allows to measure time and pulse height. If the signal exceeds a predefined threshold value corresponding to 0.3 MIPs (minimal ionizing particles), a constant fraction discriminator (CDF) produces two pulses of 150 ns. One of them is used to create a sum of all CDF signals. As a trigger condition, this sum has to be at least 13.25 times the single value ("cosmic trigger"), thus corresponding to signals from at least 14 scintillator huts during 150 ns. Readout is started ("event trigger") in case the readout of the precedent event has been completed.
In clear nights with the moon at high zenith angles, event triggers are also generated by the Čerenkov telescopes and the AIROBICC matrix which triggers in case of 6-fold coincidences within 200 ns. The scintillator trigger rate of 12 Hz (14 huts) is increased to 20 Hz in runs including AIROBICC.
As the cable lengths vary due to temperature differences (1-2 ns for the 150 m cables), light pulser runs are performed every 20 min. The ADC pedestals are measured by imitating a number of "empty" triggers not belonging to air showers and averaging over the measured values. After pedestal subtraction, the maximum of the ADC pulse height spectra for each hut corresponds to one MIP: this allows the determination of the conversion factor between ADC pulse height and the particle density in the detector.

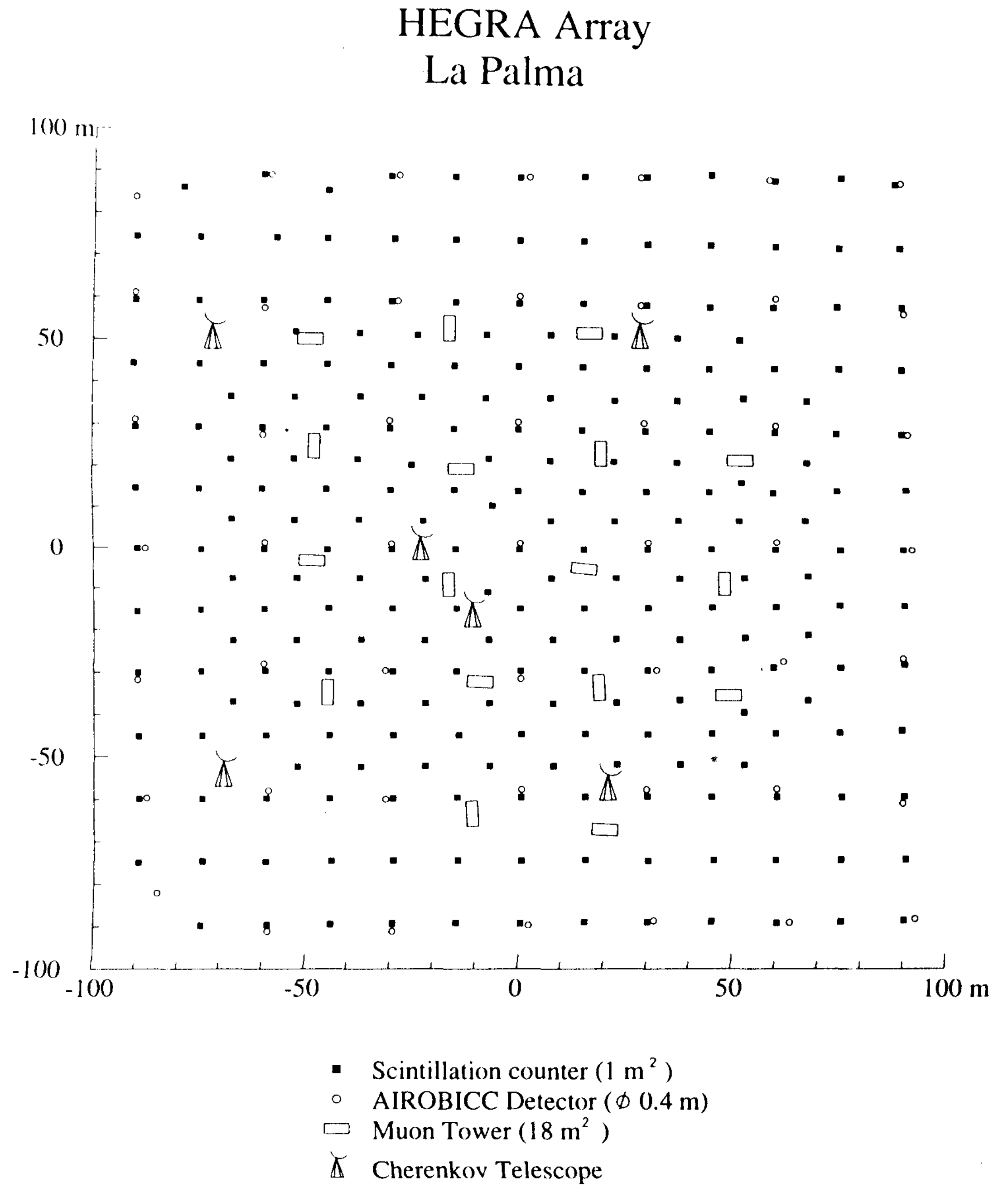

Figure 3.2: **Present layout of the HEGRA detector array at La Palma.**

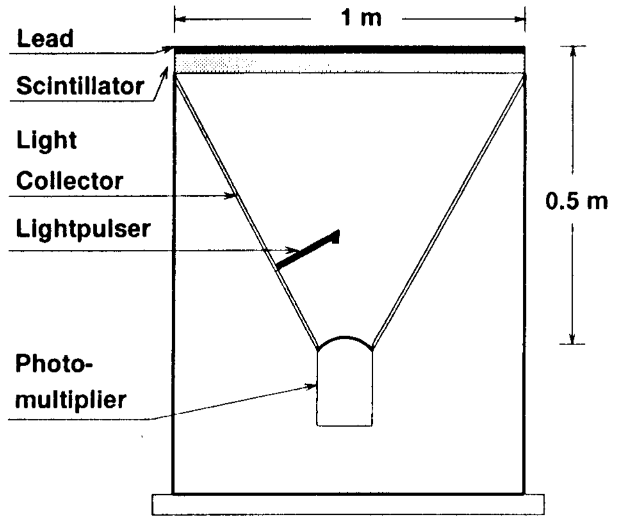

Figure 3.3: **Schematic view of a scintillation counter [91].**

Determination of shower properties

The determination of shower properties by the scintillator matrix includes several steps [91] which are briefly described in this section.
At first, the shower core position, i. e. the point where the prolongation of the primary particle's trajectory intersects the plane of the detector, is determined by a simple center of gravity method which searches for the counter with the highest particle density and calculates the sum of the densities of all counters within a $60 \times 60\,\mathrm{m}^2$ square around this counter. The sum is weighted by the counter density to correct for the different coverage in the inner and outer part of the array. Parts of the square lying outside the array are taken into account by creating virtual huts with the average value of the particle density of the existing huts assigned to them. The accuracy of this method is $\sigma_{63\%} \simeq 10\,\mathrm{m}$ for small showers and increases with increasing shower size.
In the second step, the direction of the incoming primary is determined by fitting a predefined shower front function f to the arrival times. As shown in Fig. 3.4, the electromagnetic particles of an extensive air shower build up a front of conical shape with a slope of $\simeq 13\,\mathrm{ns}/100\,\mathrm{m}$ for the HEGRA conditions.
As described in detail in [91], this direction fit is done by minimizing

$$\chi^2 = \sum_i w\,(f - t_i)^2 \tag{3.4}$$

with t_i denoting the arrival time measured by hut i. w is a weighting function and f is called the shower front function. Whereas it was taken as a simple plane in earlier applications, the direction fit for the upgraded HEGRA array uses f and w depending on the distance r from the previously determined shower core and the number N of particles detected by the counter. As an important improvement, $f(r, N)$ and $w(r, N)$ are determined from the experimental data, a procedure which guarantees an optimal

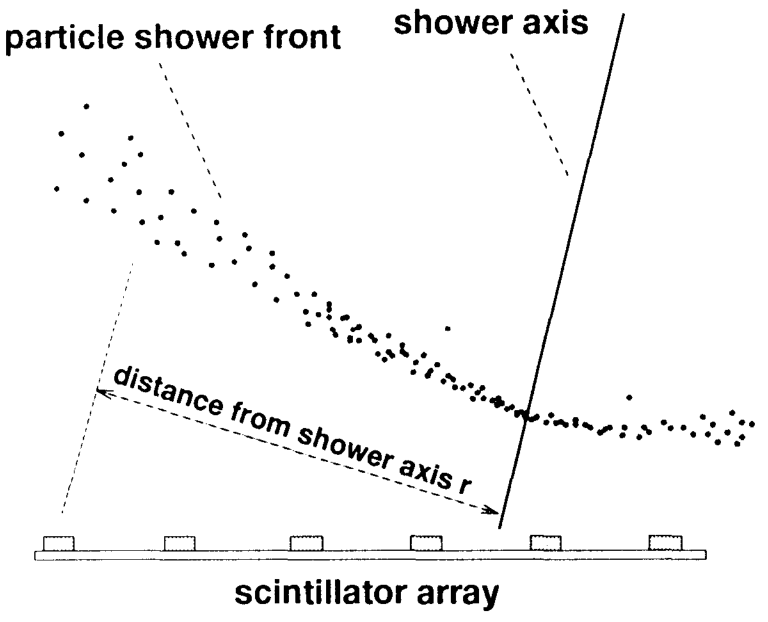

Figure 3.4: **The direction of the primary particle (shower axis) is reconstructed by fitting a shower front function to the arrival times of the particles as measured by the scintillator array [91].**

adjustment to HEGRA conditions.
In a third step, the number of electromagnetic shower particles is determined by fitting the so-called NKG (Nishimura-Kamata-Greisen) function [92] to the electron density $\rho(r)$ in a distance r from the shower core,

$$\rho(r) \propto \frac{N_e}{r_0^2} \left(\frac{r}{r_0}\right)^{s-2} \left(1 + \frac{r}{r_0}\right)^{s-\frac{9}{2}} \tag{3.5}$$

r_0 is the Molière radius (112 m at HEGRA altitude), which is the characteristic lateral scale of the shower. It is dependent on density and indicates the amount of multiple scattering in the atmosphere.
Both N_e and s are free parameters. s is called shower age and has the value 0 at the beginning of the cascade, 1 at the maximum, and ≥ 1 during the dying out phase of the shower development.

The resulting angular resolution of the HEGRA scintillator array can be described as a function of the total number of electrons by

$$\sigma_{63\%}(N_e) = \frac{(104.5 \pm 0.4)^\circ}{\sqrt{N_e}} \ . \tag{3.6}$$

Thus, for a minimum N_e of 10 000, the angular resolution is $\sigma_{63\%} = 1.0°$.
The resolution has been checked by various methods [91]. One of them, the search for

a deficit from the direction of the moon, is also applied in this analysis and described in more detail in Chapter 6.

3.2.2 The Geiger tower sub-array

In HEGRA, the information about the charged particle content and energy distribution is obtained by 17 Geiger towers [87], each consisting of 6 layers of 160 Geiger tubes with quadratic cross section ($1.5 \times 1.5\,\mathrm{cm}^2$) and 600 cm in length. Covering an active area of $270 \times 600\,\mathrm{cm}^2$ each, they are placed in the central part of the HEGRA array as an additional matrix with distances of about 30 m.
A sectional drawing of a HEGRA Geiger tower is shown in Fig. 3.5. The layers are separated by 10 cm of light concrete (density $0.8\,\mathrm{g\,cm}^{-3}$) and 10 cm of air. The first two Geiger tube layers are followed by 4.5 r.l. of lead absorber each, so the Geiger towers work as individual calorimeters supplying information about the particle density and the energy distribution in different distances from the core. The lower planes are used

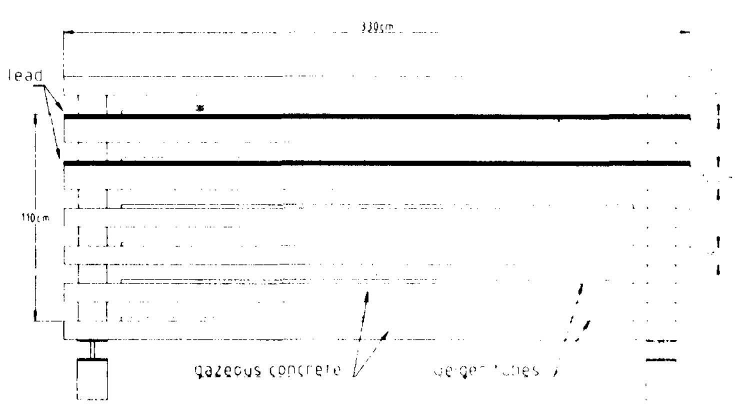

Figure 3.5: **Front view of a Geiger tower.**

for the reconstruction of muon tracks and tracks caused by high energy $e^{\pm}, \gamma$ and – to a small amount – hadrons penetrating the lead absorber.
16 Geiger tubes form a so-called bi-octotube as schematically shown in Fig. 3.6. Each bi-octotube is read out by a 16-channel readout board. The tubes are supplied with a gas mixture of 98.9% argon, 1.0% propan, and 0.1% freon at a flow rate of 6 l/h by a central mixing facility. Past experience has shown that a small percentage of vapor has to be added to counteract the inevitable aging of the wires [93]. Each wire has a positive high voltage of 1150 V resulting in a current of about 1 μA per Geiger tube.
The Geiger tubes together with the readout electronics are remnants from the dismantled Fréjus underground detector, and parts of the electronic had to be re-designed to

Figure 3.6: **Cross section of a Geiger octotube.**

account for the high rates of the HEGRA experiment. As a very important upgrade, an additional edge sensitive secondary readout electronic [94] has been implemented to reduce the accidental background. This is necessary since the typical duration of a Geiger pulse is about $70\,\mu$s and thus a considerable amount of Geiger pulses caused by particles not belonging to the triggering air shower are additionally read out after the trigger signal. To avoid this, each layer of a Geiger tower is equipped with an additional 10-channel readout board with one channel per bi-octotube. In case a Geiger pulse is detected on one of the 16 channels of a bi-octotube, a signal is send to this secondary readout board and triggers another $3\,\mu$s signal. Only in case this $3\,\mu$s signal is in coincidence with the array trigger, a voltage level is applied to an additional CMOS shift register. Apart from the 160-fold Geiger tube status information of each layer, additionally 10 channels per layer now carry information about whether at least one pulse on the corresponding bi-octotube is in coincidence with the trigger signal. If only the hits registered by these bi-octotubes are taken into account, the sensitive time period is shortened from $70\,\mu$s to $3\,\mu$s, thus considerably reducing accidental hits and tracks, which due to their high rate (2.5 kHz) else make the hit information valueless. The towers have been used to determine the integral muon flux at HEGRA altitude, and the experimental value $(0.58 \pm 0.05)\,\mathrm{min}^{-1}\,\mathrm{cm}^{-2}\,\mathrm{sr}^{-1}$ [94, 95] is in good agreement with interpolations of measurements at sea level and 3000 m a. s. l.

Geiger tower and scintillator simulation

For a complete understanding of the capabilities of detectors, a reliable *detector simulation* is crucial, as this is the only way to extract necessary information, e. g. efficiencies for track finding and hadron suppression. A full three-dimensional MC simulation of the relevant detector parts, additionally fine-tuned on experimental data, is furthermore essential for the development of reliable γ/hadron separation techniques.

For the MC simulation of the Geiger tower array, a program based on the well-established GEANT 3.21 [96] code is used. The GEANT code allows to describe the experimental setup by so-called geometrical volumes, with the corresponding material

and tracking medium parameters (atomic weight, atomic number, radiation length, density) assigned to the volumes. For each shower particle reaching the observation level, the particle type, the position, and the momentum vector are passed to the GEANT input routine, and GEANT then takes over the tracking of the particle through the experimental setup. Important parameters used for the Geiger tower event simulation are summarized in Tab. 3.1 and Tab. 3.2. The threshold energies for different particle types given there refer to the kinetic energy of the particles: if it drops below this value, tracking of the corresponding particle is terminated.
Physical effects taken into account during tracking include decay, multiple scattering, muon nuclear interaction, energy loss, photo electric effect, Compton scattering, pair production, bremsstrahlung, annihilation, and hadronic processes.

Table 3.1: **Kinetic energy cuts used for the GEANT detector simulation.**

particle	kinetic energy cuts [MeV]
γ	0.1
$e^{\pm}$	0.1
neutral hadrons	10
charged hadrons	10
$\mu^{\pm}$	30

Table 3.2: **GEANT tracking medium parameters.**

medium	density [$\mathrm{g\,cm^{-3}}$]	radiation length [cm]
air (2200 m a.s.l.)	$0.986 \cdot 10^{-3}$	37 181
ytong	1.0	33.7
aluminium	2 700	8.9
argon	$1.78 \cdot 10^{-3}$	11 000
lead	11 350	0.56

To test the reliability of the detector simulation, the Fréjus test detector was implemented in GEANT and the simulated detector response was compared to data taken during the calibration in electron and hadron beams at DESY and Bonn. Experimental data and MC simulation correspond to a satisfying degree [87].
The additional electronics for suppression of accidental tracks and hits is fully simulated, using the muon flux value quoted above. The simulation additionally includes the scintillator matrix to account correctly for the trigger condition.

Tracks are reconstructed using an algorithm which first groups neighboring hits to clusters, allowing for not more than one "dead" wire between two hits. Half the cluster width is taken as the positional error of the cluster center. The algorithm then loops over all pairs of clusters and accepts only combinations with at least 4 clusters lying on a straight line as track candidates. Using the cluster positional error, weighted linear regression then delivers the track parameters. In a cleaning process, fake tracks are removed by comparing the χ^2 of tracks sharing more than one cluster with other tracks.

The efficiency of this track finding procedure naturally depends on the complexity of the hit pattern. As shown in [87], the reconstruction efficiency near the dense shower core region is only 50 to 60 %, but exceeds 90 % at a distance of more than 30 m from the core. A typical example both of the GEANT simulation of the Geiger array and the track finding algorithm is given in Fig. 3.7 showing the hit pattern of a Geiger tower near the core of a 50 TeV proton induced shower. The track finding algorithm has successfully reconstructed two muons, characterized by a small number of hits per layer. In addition, a high energy electron, positron, or converting γ has produced a subshower with a large number of hits in each layer.

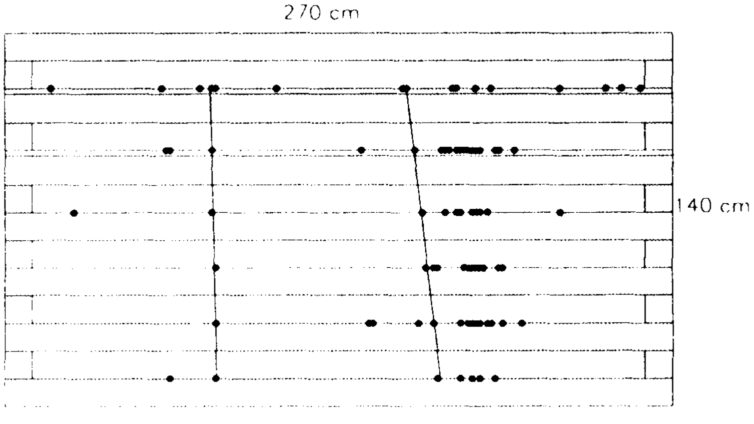

Figure 3.7: **Hit pattern of a Geiger tower near the core of a 50 TeV proton induced shower (MC simulation). Hits in the 160 Geiger tubes per layer are indicated by solid points.**

3.3 γ/hadron separation: Basic Ideas

As the main aim of the subsequent analysis is the search for point sources, it is important to know the dependence of the signal-to-noise ratio on air shower parameters like the exposure time T and the size of the sensitive detector area A.
Clearly the signal is a linear function of T and A, whereas the noise also depends on the angular resolution $\Delta\alpha$ of the detector. Different spectral indices γ_s and γ for the source and the overall cosmic ray spectrum have to be considered. Assuming furthermore a γ/hadron separation which reduces the hadronic background by a factor ϵ_{had} while keeping a fraction ϵ_γ of the signal, the signal-to-noise ratio is

$$\frac{\text{signal}}{\text{noise}} \propto \frac{E^{-\gamma_s}\, A\, T\, \epsilon_\gamma}{\sqrt{E^{-\gamma}\, A\, T\, (\Delta\alpha)^2\, \epsilon_{had}}} = E^{\frac{\gamma}{2}-\gamma_s}\, \sqrt{A\,T}\, \frac{1}{\Delta\alpha}\, Q\ . \tag{3.7}$$

Whereas signal to noise improves only with the square root of observation time and detector area, it linearly depends on the angular resolution $\Delta\alpha$ and the so-called γ/hadron separation quality factor Q defined as

$$Q = \frac{\epsilon_\gamma}{\sqrt{\epsilon_{had}}} , \tag{3.8}$$

which is used in the subsequent chapter for comparing different γ/hadron separation techniques. In addition, source spectra which are considerably flatter than the overall cosmic ray spectrum with $\gamma = 2.7$ would further increase the chance of source detection at higher energies.
In the last years, the major work in HEGRA has thus been devoted to the improvement of the angular resolution and the search for powerful methods to suppress the overwhelming hadronic background.
In the remaining part of this chapter, some basic concepts for a new γ/hadron separation based on the information provided by the Geiger tower array are described. The method itself is evaluated in the next chapter. As the analysis is based on the Monte Carlo generator CORSIKA [81], the next section will give a short outline of the basic features of this code.

3.3.1 The Monte Carlo generator CORSIKA

The Monte Carlo code CORSIKA (COsmic Ray SImulations for KAscade) has been developed for the extended air shower array KASCADE [97] in Karlsruhe and simulates the evolution of air shower cascades in the atmosphere. For the electromagnetic part of the shower, the simulation is taken over by the well-established EGS4 [98] code, which treats $e^\pm$ and γ. Muons do not undergo any nuclear reaction, but only decay.
The simulation of low energy ($E \leq 80\,\mathrm{GeV}$) hadron-nucleus collisions and the calculation of elastic and inelastic cross sections of hadrons is based on the GHEISHA code [99], and for the simulation of high energy interactions, the user may choose between routines based on the Dual Parton Model (DPM) [100] or the VENUS (Very Energetic NUclear Scattering) code [101]. Whereas the DPM routines of CORSIKA are fast and adapted to the (few) experimental data available, VENUS tries to simulate heavy ion collisions in detail based on the creation and fragmentation of strings. Parameters and methods used in VENUS are expected to improve further with new HERA results [102].
A very crucial point for extensive air shower MC is the parametrization of the atmosphere. CORSIKA uses an atmosphere consisting of N_2 (78.1 %), O_2 (21.0 %), and Ar (0.9 %) and a density variation with altitude based on the so-called U. S. standard atmosphere which is composed of 5 layers. In the lower 4 layers, the mass overburden depends exponentially on the height, in the upper layer the dependence is linear. The upper boundary of the atmosphere is at 112.8 km, which is the height where the tracking of the primary particle through the atmosphere starts.
For the following analysis, CORSIKA is used in its version 4.06. For all showers, the full EGS simulation and the VENUS and GHEISHA options are chosen. The Earth's magnetic field at La Palma ($B_x = 29.5\,\mathrm{G}, B_z = 23.0\,\mathrm{G}$) is implemented to account correctly for the deflections of charged particles. Simulation terminates at HEGRA altitude (2200 m a.s.l.).

The full MC simulation of air showers is a time-consuming process, and MC statistics will always be well behind experimental data statistics. As only a small part of the particles reaching observation level are actually detected, it is tempting to multiply MC statistics by shifting the core position n times and thus create n showers from *one* CORSIKA generated shower.

This method may be justified for certain types of analysis, but it is difficult to assess effects resulting from this technique. In order to avoid any biasing on the neural network based separation from this economical but dangerous procedure, every CORSIKA generated shower is used only *once* in the following analyses.

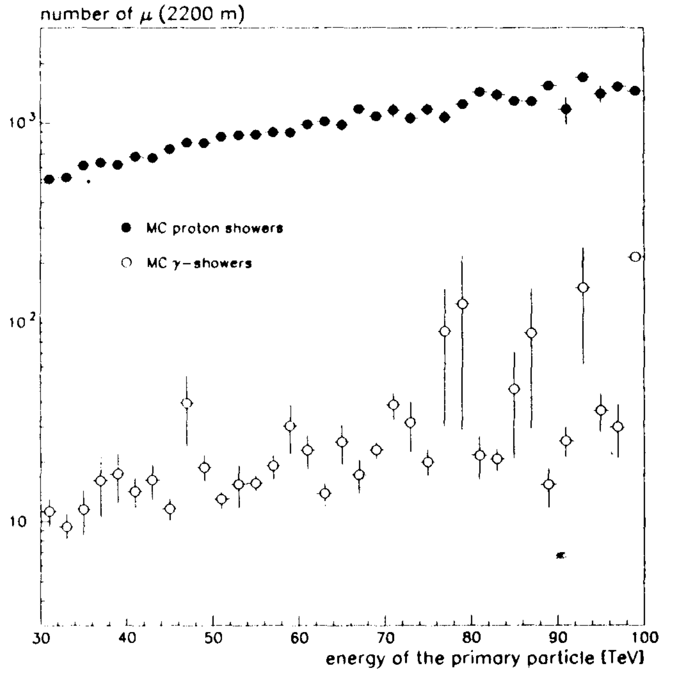

Figure 3.8: **Mean number of muons at HEGRA altitude as a function of the energy of the primary particle for γ- and proton-induced air showers.**

3.3.2 The charged particle content

In γ-initiated air showers, muons are produced at a significantly lower rate than in hadron-induced air showers, as the probability of muon production via processes like

$$\gamma\gamma \longrightarrow \mu^+\mu^- \tag{3.9}$$

or photo-pion production and decay of charm particles is considerably smaller than muon production in the hadronic cascades of showers induced by protons and heavy nuclei. Fig. 3.8 shows the mean number of muons on HEGRA observation level as a

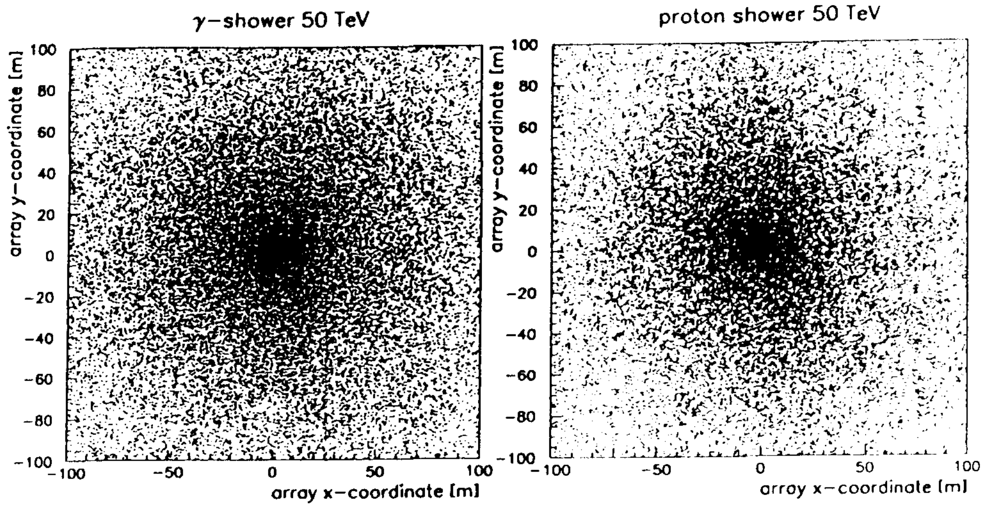

Figure 3.9: **$e^{\pm}$,γ reaching the HEGRA observation level in a 50 TeV γ- and proton induced air shower.**

function of the energy of the primary particle for γ- and proton-showers: the muon content of γ-induced showers is only 1 % of the muon content of proton showers. Furthermore, at least for hadronic showers, the number of muons is a (weak) indicator of the primary energy.

The detection of the muon content of air showers is the classical method of γ/hadron separation, and significant hadron suppression has been achieved by sophisticated methods of estimating the number of muons [103].

Nevertheless, there is a major drawback to this procedure. The muon-sensitive detector sampling density of current air shower arrays is rather small ($\simeq$ 2 % for the HEGRA Geiger sub-array), thus only a small fraction of the muons ($\simeq$ 1 %) can actually be detected.

Expecting only $\simeq$3 muons per hadronic shower, the rather large event-to-event fluctuations make the muon content a poor tool if taken alone. It is therefore necessary to search for additional possibilities of separation. As a crucial advantage, the Geiger towers are not simply tracking tools, but have a large active area and the lead absorber acting as an energy threshold which allows to estimate the energy of the electromagnetic content in different distances from the core. We therefore have to investigate further the $e^{\pm}$ and γ-content of air showers which exceeds the muon content by several orders.

As said before, anisotropies in the shower development label hadronic showers and cause non-uniformities in the longitudinal and thus also in the lateral distribution of electromagnetic particles ($e^{\pm}, \gamma$) reaching the observation level. Computer simulations of the distribution of $e^{\pm}, \gamma$ reaching the observation level of the HEGRA array on an area of $200 \times 200\,\mathrm{m}^2$ for a 50 TeV γ- and proton shower show differently shaped cores (Fig. 3.9). In contrast to hadron showers, the core of γ-showers is more concentrated and the particle distribution is much smoother and without non-uniformities.

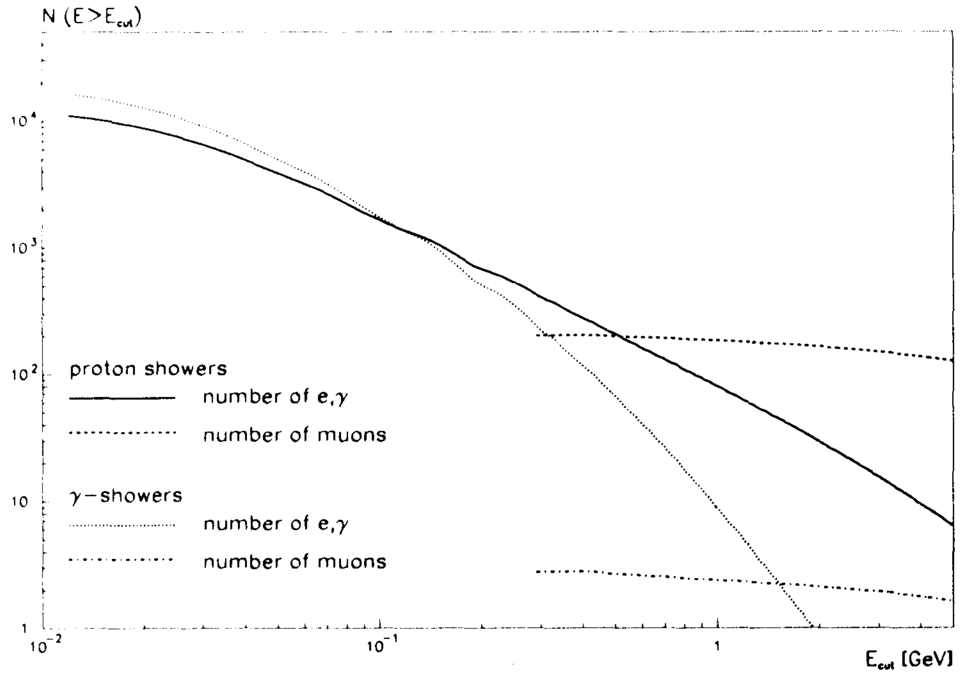

Figure 3.10: **MC studies on the differences between γ- and proton-induced air showers: the number of electromagnetic particles ($e^{\pm}, \gamma$) and muons with energy greater than E_{cut} reaching the HEGRA observation level as a function of E_{cut} in distances between 30 and 100 m from the shower core for proton and γ-induced showers.**

Outside the dense core region with a radius of $\simeq$ 30 m the particle distribution in hadron-induced showers is rather grainy, and the *hot spots* in the distribution strongly correlate with high energy $e^{\pm}$ and γ. This is summarized in Fig. 3.10. The computer simulation shows the mean number of electromagnetic particles ($e^{\pm}, \gamma$) and the mean number of muons with energies greater than a cut energy E_{cut} for 1000 MC γ- and 1000 proton showers as a function of E_{cut}. Only particles reaching the HEGRA observation level within 30 to 100 m from the shower core are taken into consideration. The energy of the primary particle is distributed between 30 and 500 TeV according to an exponential spectrum $dN/dE \propto E^{-\gamma}$, with $\gamma = 2.75$ being the spectral index. There are several results:

1. The muon content of proton showers exceeds the muon content of γ-showers by about two orders of magnitude.

2. The number of low energy electromagnetic particles ($e^{\pm}$,γ) in γ-showers exceeds the corresponding number in proton showers.

3. For particle energies above 400 MeV, the number of $e^{\pm}$ and γ in proton showers is comparable to the number of muons and higher than the corresponding numbers

in γ-showers.

High energy $e^{\pm}$ and γ outside the core thus strongly indicate proton induced showers. We are confronted with the rather striking fact that one of the main shortcomings of "calorimetric" type detectors like the Geiger tower array, the inability of rigorously discriminating between $\mu^{\pm}$ and $e^{\pm}$ (so-called *punch-throughs*), is an advantage for γ/hadron separation: high energy $e^{\pm}$ and – in addition – photons converting into $e^{\pm}$-pairs are indicators of hadronic showers just like $\mu^{\pm}$. When penetrating the lead absorber, they show up as a track or as a small electromagnetic sub-shower within the tower as shown in Fig. 3.7. Summarizing, it is not the *muon track* as such which carries the necessary information, but in general the *track outside the shower core*. The number of detected tracks is in fact almost doubled by the high energy $e^{\pm}, \gamma$ carrying the same information.
As the weak electromagnetic component which carries the major part of the energy of γ-induced showers is almost totally absorbed in the 10 r. l. of lead absorber, only a few hits are expected in the lower layers of the Geiger towers with sufficient distance from the dense core region. A large number of hits in the lower layers thus also indicates hadron showers, even in cases where the high energy particles produce a cascade and no track fitting is possible (see Fig. 3.7). Hence, it is crucial to use the Geiger towers not as mere tracking tools, but also as a detector which records the energy content as a function of the distance from the shower core.
It is a major task of the Geiger tower analysis to extract the relevant information with high efficiency. A possible way to do so is motivated and outlined in the next chapter: the analysis of the Geiger data using computer-simulated neural networks.

Chapter 4

Neural network γ/hadron separation

Detectors like the Geiger towers of the HEGRA array with their multi-layer structure and their rather moderate thickness of absorbing material (9 r. l.) are powerful tools for equally exploiting the calorimetric information contained in the electromagnetic particles and the muon and high energy $e^{\pm}, \gamma$ content of air showers.
Nevertheless, the γ/hadron separation criteria presented in the previous chapter are in fact rather limited tools, since the small detector sampling density ($\simeq 3.5\%$ only) hardly allows to resolve the granularity of hadron showers and prevents a large fraction of the muons from being detected. Exploiting the different energy distributions in a straight-forward cut suffers from the fact that single showers are subject to large fluctuations. Therefore the optimal selection criterion is different in each event and the weights of these criteria are a priori unknown.
As a consequence γ/hadron separation based on *serial cuts* in the number of tracks or hits or any other quantity derived from the hit number faces one of the most severe shortcomings of conventional analysis: the application of various low-dimensional cuts in observed variables is inefficient and time-consuming both in developing the technique and carrying it out. The neural network technique replaces this procedure by parallel handling of the input data and nonlinear cuts in data space.
Neural nets have proven to be an appropriate technique with high efficiency and stable performance in a number of applications (see e. g. [104]). On the other hand, they are often regarded as unreliable and opaque, hence one may hesitate to apply them in data analysis where transparency is required. An understanding of the network cut in terms of classical analysis is indeed difficult, since the network output is a very complicated function of the input data. A large part of this chapter therefore deals with methods helping to gain insight in what at the first glance might look like a black box.
After a general description of the network technique itself and the training algorithm applied here, the criteria actually playing part in the network γ/hadron separation are estimated by artificially disabling input information and testing the resulting performance.
Furthermore, methods from multivariate analysis, principal component analysis and discriminant analysis, visualize the network learning process and help to construct the

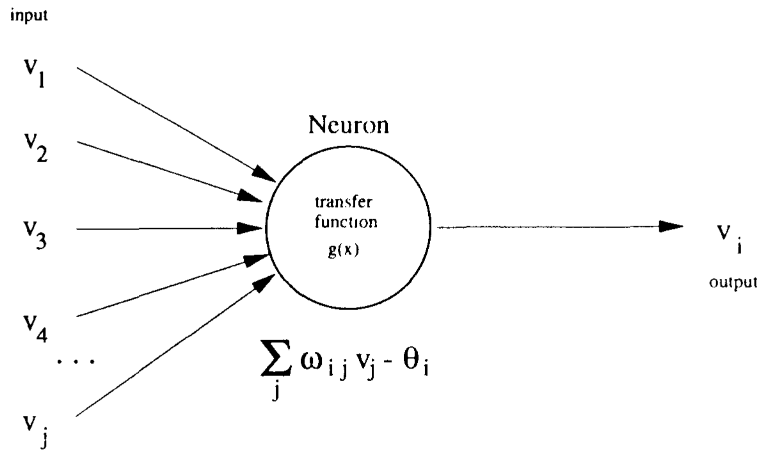

Figure 4.1: **Schematic of a neuron.**

optimal network topology and therefore to minimize the number of arbitrary network parameters.

4.1 Network training

4.1.1 General remarks

In a typical classification problem like the separation of γ- and hadron-induced air showers, a set of p events with k_{max} observed variables each, described by the input vector

$$\vec{x}^{(p)} = (x_1, x_2, \ldots, x_{k_{max}}), \tag{4.1}$$

has to be assigned to output categories y_i using a classification function

$$\vec{y} = \vec{F}(\vec{x}). \tag{4.2}$$

As an example, a separation between signal and background events may be based on a one-dimensional output y_1 with the desired value 0 for signal and 1 for all types of background events.
The neural network training takes over the search for the optimal choice of the classification function $\vec{F}$. The basic element of neural networks is the so-called neuron or node [105] (see Fig. 4.1). A neuron receives input signals v_j from neighbor neurons and computes the weighted sum of its inputs, compares the sum to a threshold value θ and – in case of binary nodes – outputs either "1" or "0" depending on the input sum:

$$v_i = \Theta\left(\sum_j \omega_{ij} v_j - \theta_i\right). \tag{4.3}$$

The weights $\vec{\omega}$ represent the strength of the connections between the neurons. The Heaviside function Θ of the binary neuron is usually replaced by a nonlinear activation function g, thus allowing a graded response instead of a simple "yes/no" decision. A common choice is the continuous differentiable sigmoid activation function

$$g(x) = \frac{1}{2}\left(1 + \tanh\left(\frac{x}{T}\right)\right), \tag{4.4}$$

which for the limit $T \to 0$ reduces to the Heaviside function Θ. The parameter T is called temperature and is usually set to 1. In a feed-forward neural network (as used in this analysis) with k_{max} so-called input nodes, i. e. k_{max} dimensions of the input vector, i_{max} output nodes, and one hidden layer with j_{max} nodes for the internal representation of $\vec{x}$ by the network (see Fig. 4.2), $\vec{F}$ therefore corresponds to

$$F_i(\vec{x}) = g\left(\sum_{j=1}^{j_{max}} \omega_{ij} g\Big(\sum_{k=1}^{k_{max}} \omega_{jk} x_k + \theta_j\Big) + \theta_i\right). \tag{4.5}$$

g and therefore F_i is restricted to values between 0 and 1. To simplify the deviation of the learning rule in the next subsection, thresholds are consequently omitted in the description, as they can always be treated as weights $\theta_i = \omega_{i0}$ with $x_0 = 1$.
The architecture of simple feed-forward neural nets as mathematically described in Eq. 4.5 with adjacent layers fully connected is unequivocally determined by the number of nodes per layer. They are referred to as $k_{max} - j_{max} - i_{max}$ networks in the following sections.
The weights ω_{ij}, ω_{jk} are free parameters adjusted to a training data distribution by minimizing e. g. a mean square error. The whole training data sample is repeatedly presented to the network in a number of training cycles. After the network training an independent test data sample is used to check whether the net is able to generalize the classification to "unknown" data.

4.1.2 The backpropagation algorithm

The application of the neural network technique in data analysis heavily depends on whether it is possible to find a robust method of weight adjustment. The great success of neural networks in the last decade is mainly based on the deviation of an iterative learning algorithm based on gradient descend, the so-called backpropagation algorithm, by Rumelhart in 1985 [106].
The general idea is to adapt the weights by learning a training set of input-output pairs $(\vec{x}, \vec{t})$. The input vector $\vec{x}$ is propagated through the network to create an output vector $\vec{y}$ which is then compared to the desired "true" output vector $\vec{t}$. If $\vec{x}$ does not equal $\vec{t}$, the weights are adjusted by minimizing e. g. the Euclidean distance $|\vec{t} - \vec{x}|$. For a straight-forward deviation of the learning rule, the network shown in Fig. 4.2 is used. It is a two-layer feed-forward network with one hidden layer. The weights ω_{jk} connect input and output layer, the weights ω_{ij} connect hidden and output layer. The activation function of the input neurons is linear, for all other neurons, the sigmoid function 4.4 is used. Start values for the weights are chosen at random to avoid any

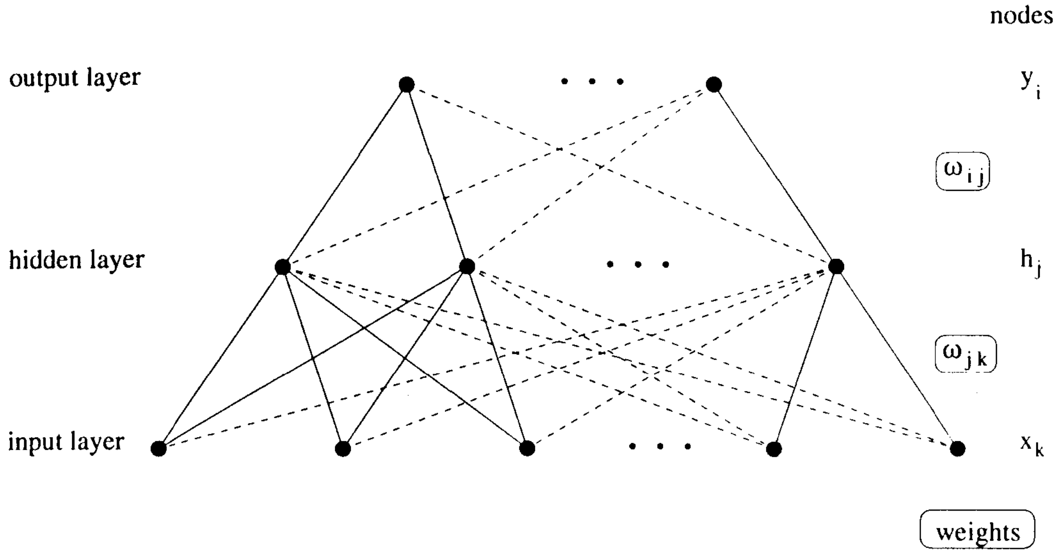

Figure 4.2: **Feed-forward neural network with one hidden layer.**

symmetry at the beginning of the learning process.
With p being an element of the training data sample, the hidden neuron j receives the input

$$h_j^p = \sum_{k=0} \omega_{jk} x_k^p \tag{4.6}$$

and produces the output

$$V_j^p = g(h_j^p) = g(\sum_{k=0} \omega_{jk} x_k^p). \tag{4.7}$$

The output neuron i receives

$$h_i^p = \sum_{j=0} \omega_{ij} V_j^p \tag{4.8}$$

and produces the final output

$$y_i^p = g(h_i^p) \tag{4.9}$$

$$= g\left(\sum_{j=0} \omega_{ij} g\left(\sum_{k=0} \omega_{jk} x_k^p\right)\right). \tag{4.10}$$

To optimize the weights, an error function (or "cost" function) E is introduced. This may be the Euclidean distance

$$E(\vec{\omega}) = \frac{1}{2} \sum_{p,i} (t_i^p - y_i^p)^2 \geq 0. \tag{4.11}$$

The optimal weight values $\vec{\omega}$ minimize E. As

$$E(\vec{\omega}) = \frac{1}{2} \sum_{p,i} \left\{ t_i^p - g\left(\sum_{j=0} \omega_{ij} g\left(\sum_{k=0} \omega_{jk} x_k^p\right)\right)\right\}^2 \tag{4.12}$$

is a continuous differentiable function of $\vec{\omega}$, it is possible to apply gradient descent:

$$\Delta\omega_{ij} = -\eta\frac{\partial E}{\partial\omega_{ij}} \tag{4.13}$$

$$\Delta\omega_{jk} = -\eta\frac{\partial E}{\partial\omega_{jk}}. \tag{4.14}$$

η is the so-called learning rate and controls the speed of weight adjustment. It is the most important parameter of the network learning process.
Gradient descent gives

$$\Delta\omega_{ij} = \eta\sum_p \left(t_i^p - y_i^p\right) g'(h_i^p)V_j^p \tag{4.15}$$

$$= \eta\sum_p \delta_i^p V_j^p \tag{4.16}$$

where

$$\delta_i^p = \left(t_i^p - y_i^p\right) g'(h_i^p) \tag{4.17}$$

is introduced. δ is the Euclidean distance between the actual network output and the desired output value, multiplied by the derivative of the activation function (δ-rule).
For the weights between input and hidden layer, the chain rule is applied

$$\Delta\omega_{jk} = -\eta\sum_p \frac{\partial E}{\partial V_j^p}\frac{\partial V_j^p}{\partial\omega_{jk}}. \tag{4.18}$$

Using Eqs. 4.7 and 4.12 gives

$$\frac{\partial V_j^p}{\partial\omega_{jk}} = g'(h_j^p)x_k^p, \tag{4.19}$$

and

$$\frac{\partial E}{\partial V_j^p} = -\sum_{p,i} \left(t_i^p - y_i^p\right) g'(h_i^p)\omega_{ij} \tag{4.20}$$

$$= -\sum_{p,i} \delta_i^p\omega_{ij}. \tag{4.21}$$

Combining these results gives

$$\Delta\omega_{jk} = \eta\sum_{p,i} \delta_i^p\omega_{ij}g'(h_j^p)x_k^p. \tag{4.22}$$

Introducing

$$\delta_j^p = g'(h_j^p)\sum_i \omega_{ij}\delta_i^p \tag{4.23}$$

leads to the final formula

$$\boxed{\Delta\omega_{jk} = \eta\sum_p \delta_j^p x_k^p.} \tag{4.24}$$

Apart from the definition of δ, Eqs. 4.15 and 4.24 have the same form. In general, the backpropagation learning rule for a feed-forward network with m layers is therefore

$$\boxed{\delta^p_{b,m-1} = g'(h^p_{b,m-1}) \sum_a \omega_{ab,m}\delta^p_{a,m}.} \tag{4.25}$$

Thus the backpropagation algorithm includes the following steps: at first, the input signal propagates through the network until the final output is calculated. Now the δ_m for the output layer is calculated by comparing $\vec{x}$ and $\vec{t}$, and the δ_{m-1} of the preceding layer may be calculated by using δ_m. Whereas the signal propagates in forward direction, the error signal propagates backwards (hence the name *backpropagation*). After all δ have been calculated, the weights are adjusted according to

$$\boxed{\omega^{new}_{ab} = \omega^{old}_{ab} + \Delta\omega_{ab}.} \tag{4.26}$$

Although the learning rules imply that the weights are updated after each training epoch, i. e. after all p patterns $\vec{x}$ have been presented to the network, this is not what is usually done. In practice, the weights are updated after every pattern or after a small subset of patterns (usually 10). Apart from being much faster, this incremental or on-line method is more effective in case of regular or redundant training data and is thus superior in most physics applications.

Depending on the problem, it may also be more appropriate to make the learning rate η a function of time, i. e. to start with a high learning rate and gradually decrease η during the training to allow a fine-tuning of the weights.

For a detailed description of the network technique, the backpropagation algorithm and modifications of the learning rule, see e. g. [107]. A number of alternative algorithms and network architectures have been proposed in the last decade, but for standard physics applications, these methods have not outperformed backpropagation in robustness and efficiency. In fact, it has been shown early in network application that only *one* hidden layer is enough to approximate any *continuous* function $\vec{F}$ [108], and that with at most *two* hidden layers any function $\vec{F}$ can be fitted, with the accuracy increasing with the number of nodes in the layers [109].

4.1.3 Network input

Since for the training and test data sample both input $\vec{x}$ and correct output $\vec{t}$ have to be known for each event, the adjustment of weights and thresholds depends on computer-simulated air showers. For the creation of the training and test showers the MC code CORSIKA (version 4.06) [81] is used.

10 000 CORSIKA generated air showers with primary energy E distributed between 30 and 500 TeV (spectral index $\gamma = 2.75$) passed a full detector simulation based on the GEANT package (version 3.21) [96] as described in the previous chapter. To imitate the experimental data as closely as possible the incident zenith and azimuth angles θ and ϕ are selected at random ($0° \leq \theta \leq 30°$, $0° \leq \phi \leq 360°$), and the core position is randomized over the array.

The MC showers are divided into a training sample (3000 showers) and a test sample

(7000 showers). Since the γ/proton separation is expected to be the most difficult task, the training sample only contains γ- and proton showers in equal shares. Showers induced by heavy nuclei like helium, carbon, and iron also form a considerable part of the hadronic background [80], but the restriction to proton showers during the training phase is justified, as proven at the end of this subsection.
As input variables for a standard feed-forward neural net [110] with sigmoid activation functions 4 values for each of the 17 towers are used:

- the number of hits in the first layer above the lead absorber,
- the number of hits in the second layer after the first 4.5 r.l. of lead absorber,
- the average number of hits in layers 3 to 6 after 9 r.l., and
- the number of reconstructed tracks (mostly muons).

Table 4.1: **Parameters of the network.**

network topology	68-17-1
learning rate η	0.005
decrease in η (per cycle) (bold driver dynamics)	0.999
number of learning cycles	500
initial weights (taken at random)	[-0.1,0.1]
patterns per update	10
overall network temperature T	1

A three-layer net with topology 68-17-1 is trained using the backpropagation algorithm to give the desired output value 0 for γ- and 1 for proton-induced showers. The parameters of the network training are summarized in Table 4.1.
An initial learning rate $\eta = 0.005$ varied during learning using the "bold driver" method with a scale factor 0.999 [111] gives the best results, but the final performance does not depend critically on the actual choice of these parameters. However, if the learning rate η is too high at the beginning of the training process, a considerable number of showers are misclassified from the beginning and the net is not able to correct this during the training, which leads to peaks at the "wrong" side of the output distribution. Using a small η avoids this problem.
The number of hidden nodes is estimated roughly by a principal component analysis applied to the hidden unit activations. This is described in the next subsection.
After about 500 training cycles the γ-shower efficiency reaches a plateau and the performance on test data does not improve any more. The learning process is stable and training and test data differ by only a few percent (Fig. 4.3 (a)). Fig. 4.3 (b) shows the network output for the γ- and proton showers of the test sample.
Although the training sample only contains γ- and proton showers, the features of proton showers are transferred to showers induced by heavy nuclei. Fig. 4.4 (a) shows the efficiency as a function of the cut in the network output for γ- and proton-induced

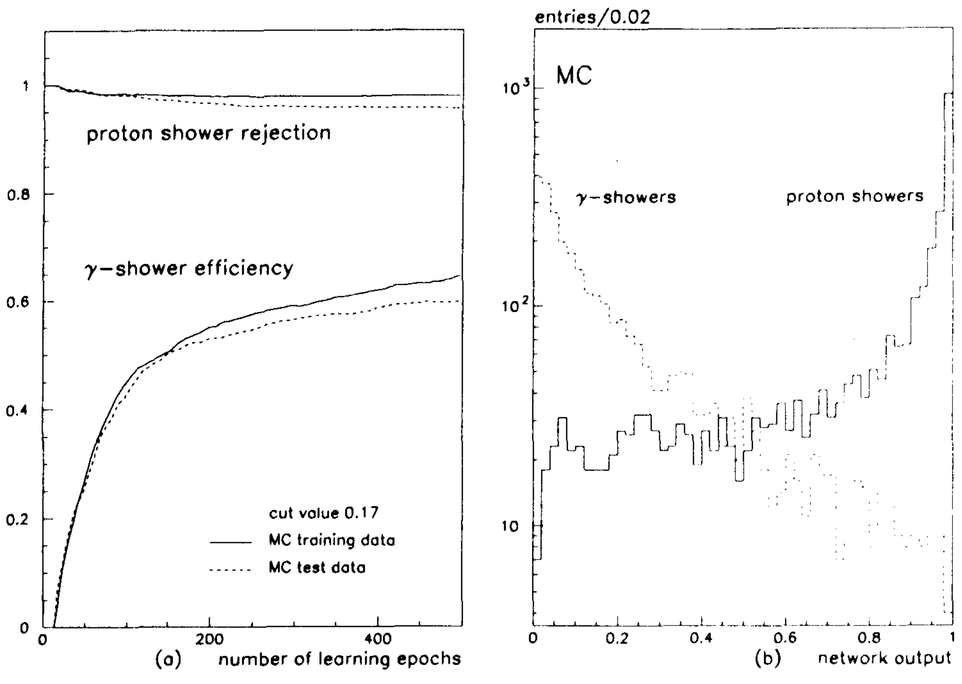

Figure 4.3: **The network performance: (a) shows the γ-efficiency and proton rejection as a function of the learning cycle for both training and test data, (b) shows the network output of 3000 γ- and 3000 proton showers of the test sample.**

showers and for showers induced by helium, carbon, and iron nuclei. The rejection power of the net increases with the atomic weight, which justifies the concentration on proton showers during the training phase.

4.1.4 Checking the net topology

Although the net performance only weakly depends on parameters directing the network learning, the *network topology* should be checked to gain optimal performance. A net with a large number of hidden nodes that do not contribute to the separation may decrease the stability of the network or result in poor generalization.

Principal component analysis (PCA) [112] is a tool from multivariate statistical theory which helps to estimate roughly the number of hidden nodes, i. e. dimensions of hidden unit space, necessary to deal with a given separation problem.

PCA searches for the directions in data space along which the data show maximum variation. The principal components are the eigenvectors of the covariance matrix, and the eigenvector corresponding to the largest eigenvalue indicates the direction in data space with maximum spread of the data points (first principal component), the eigenvector of the second largest eigenvalue gives the direction of maximum spread in the $(n-1)$-dimensional space perpendicular to the first principal component, and so

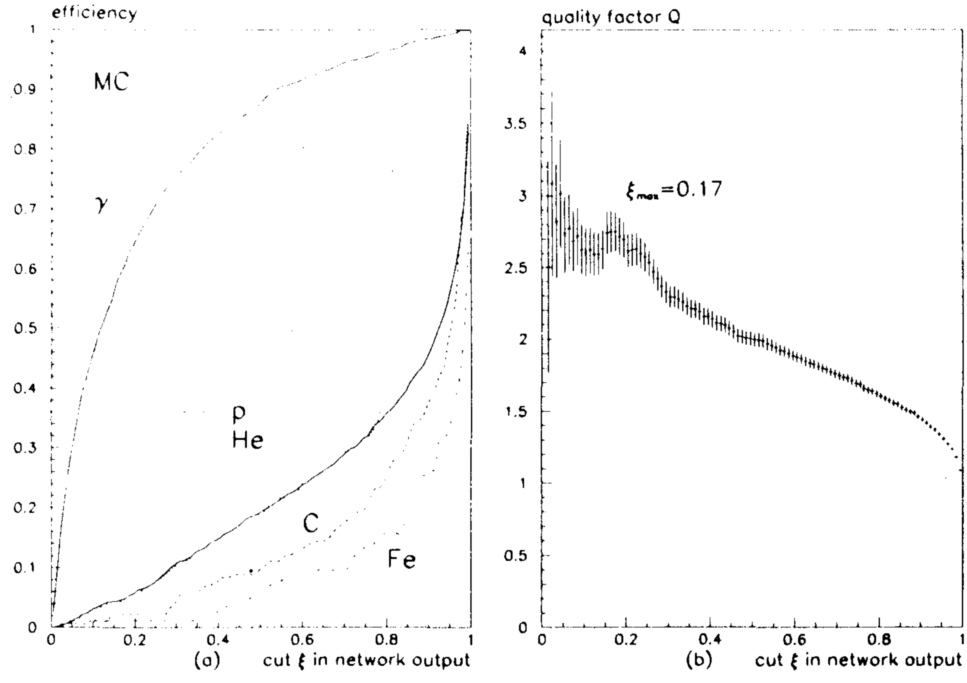

Figure 4.4: **(a) shows the network efficiency as a function of the cut ξ in the net output for proton- and γ-induced showers and showers induced by helium, carbon and iron. (b) shows the quality factor Q as a function of ξ.**

on. As the network training is based on error minimization, regions in hidden unit space which map to different network outputs will be separated as far as possible in hidden unit space, and PCA applied to the hidden unit activations may indicate the directions along which the data points are separated [113].
If n is the dimensionality of the data points d_i

$$d_i = (d_{i1}, \cdots, d_{in}) \ , \tag{4.27}$$

the covariance matrix C is an $n \times n$ matrix where the element C_{ij} is the covariance of the activations of hidden units i and j, so C_{ii} are the variances of the hidden unit values. C is calculated from the data matrix D

$$D = \begin{pmatrix} d_1 \\ \cdots \\ d_p \end{pmatrix}, \tag{4.28}$$

with p being the number of data points, by subtracting the column means

$$m = \left(\frac{d_{11} + \cdots + d_{1p}}{p}, \cdots, \frac{d_{n1} + \cdots + d_{np}}{p} \right) \tag{4.29}$$

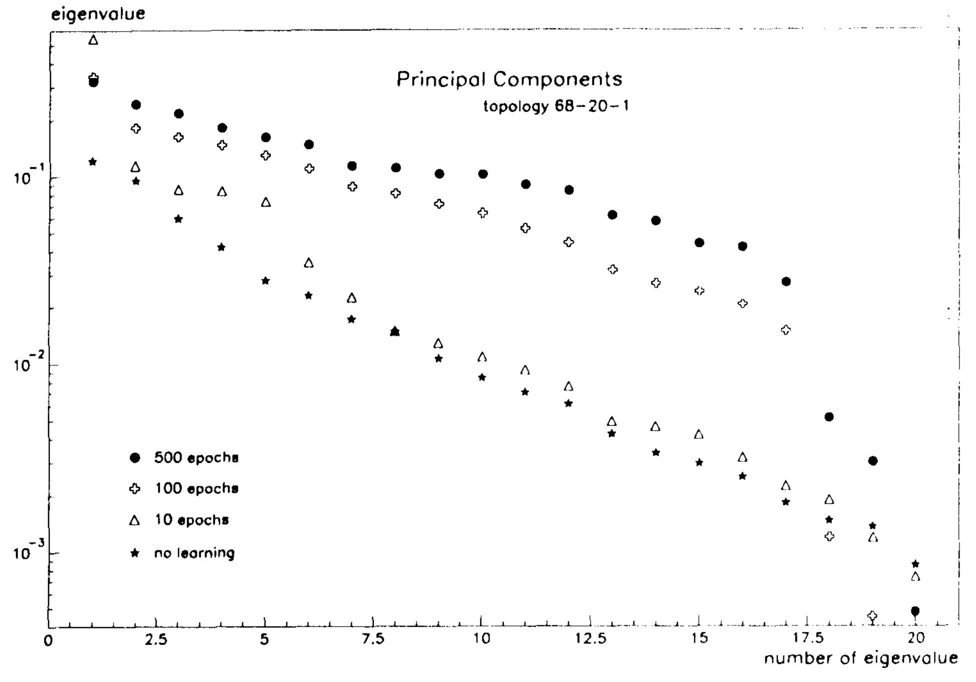

Figure 4.5: **PCA eigenvalues for the hidden unit activations of the 68-20-1 network after 0, 10, 100, 500 learning cycles.**

from each element of a column:

$$V = \begin{pmatrix} d_1 - m \\ \cdots \\ d_p - m \end{pmatrix}. \tag{4.30}$$

As the covariance matrix

$$C = \frac{1}{p-1} \; V \, V^T \tag{4.31}$$

is a real symmetric matrix, the eigenvalues are real and the eigenvectors are orthogonal. PCA is applied to the hidden unit activations of 4000 γ-showers and 4000 proton showers for a network with 20 hidden nodes. Fig. 4.5 shows the 20 eigenvalues for the hidden unit activation after 0, 10, 100, and 500 learning cycles. 3 eigenvalues of the fully trained 68-20-1 net are considerably smaller than the others and indicate that 17 hidden nodes may be enough for separating.
Since the principal components are not necessarily the best directions of discrimination in hidden unit space, the resulting topology has to be checked. In this example a re-training of the 68-net shows that 17 hidden nodes indeed yield the same performance.

4.1.5 Optimization of the net cut value ξ

Proton rejection and γ-efficiency depend on the cut value ξ in the network output. To find the optimal value of ξ, it is convenient to maximize the quality factor Q from Eq. 3.8,

$$Q_{pro} = \frac{\epsilon_\gamma}{\sqrt{\epsilon_{pro}}}, \tag{4.32}$$

with ϵ_γ and ϵ_{pro} being the fractions of γ- and proton showers passing the selection. The significance for the detection of a cosmic ray point source is a linear function of Q (see Chapter 3).

For simplicity, again we use proton showers only. According to Fig. 4.4 (a), $Q_{had} \geq Q_{pro}$, so Q_{pro} is in fact only a lower limit to the actual quality of the hadron suppression.

Fig. 4.4 (b) shows the quality factor Q as a function of the cut value ξ in the network output. The maximum quality factor is $Q = 2.8$, which is considerably better than the rejection achieved by track counting alone: a sharp cut on the number of tracks, which classifies all showers with at least one track as hadronic, yields $Q = 1.9$.

This estimation of Q is done using showers with energy above 30 TeV without considering the array trigger condition. The optimal cut value will change when the actual experimental conditions are taken into account. In the remaining part of this chapter, a cut value $\xi_{max} = 0.17$ is chosen, but this value has to be modified in the next chapter.

The energy dependence of both proton shower rejection and γ-shower efficiency is shown in Fig. 4.6 (a). To cover the whole energy range, 1000 γ-showers with energies between 10 and 500 TeV are added to the test sample. Whereas the different behavior of γ- and proton showers is a consequence of the cut value being well below 0.5, the energy dependence of the γ-efficiency reflects the information content of the events. The mean number of towers having non-zero hit information increases with the energy of the primary particle (Fig. 4.6 (b)), and the γ-efficiency increases almost linearly with the mean number of non-zero towers. This illustrates that the optimal energy region for an efficient use of the Geiger towers is above 50 TeV.

As the Geiger towers are not part of the HEGRA trigger conditions, there are a number of events ($\leq 5\%$) with only very marginal hit information. Events that do not contain the necessary information for γ/hadron separation, mainly events with less than 6 non-zero towers, do not fake γ-showers but populate an uncritical intermediate region at about 0.6 in the network output which indicates neither "γ-like" nor "hadron-like" showers. This is also true for events with no hit information at all.

Including the trigger condition during day-time (at least 14 scintillator huts) in the detector simulation and discarding events not fulfilling these conditions means increasing the γ-efficiency and thus the quality factor of the network analysis (see Fig. 4.6). The γ-efficiency, proton rejection and the *integral* quality factor $Q(E \geq E_{cut})$ for MC showers with simulated scintillator trigger condition is shown in Fig. 4.7. The inset shows that for showers above an energy threshold of 50 TeV, the quality factor is better than 3, provided the performance of the Geiger tower array is not deteriorated by non-working tubes, layers, or towers.

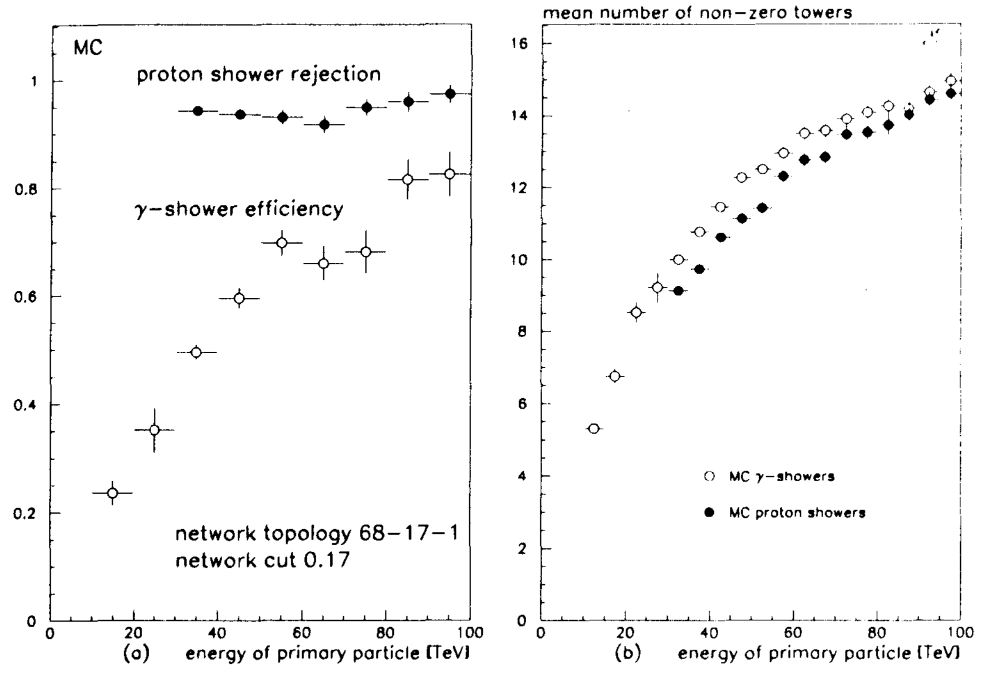

Figure 4.6: **Energy dependence of the network performance: (a) shows γ-efficiency and proton rejection and (b) the mean number of Geiger towers with hit information as a function of the energy of the primary particle.**

4.2 Understanding the network

4.2.1 Physical implications of the network learning

A way to gain the necessary insight into the network separation is to disable artificially parts of the input information and train and test networks on the reduced data.
To check the relevance of the different criteria summarized in Chapter 3, networks are trained and tested on input data

1. only consisting of the number of hits without the explicit number of tracks in the towers (net 4),

2. with artificially eliminated track information (subtraction of the number of hits caused by reconstructed tracks from the total hit number of each layer) (net 5),

3. with the number of hits per tower normalized to 1, thus making a between-tower comparison impossible (nets 2 & 6),

4. without the hits in the first Geiger layer, so the information about the incoming particles before the lead absorber is eliminated (nets 3 & 7),

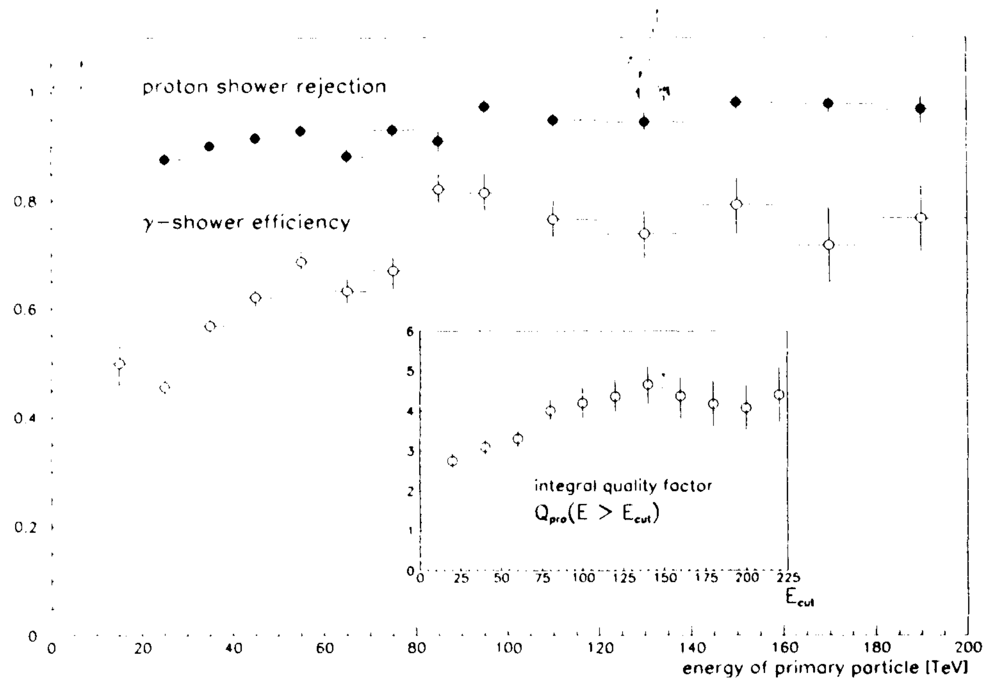

Figure 4.7: **γ-shower efficiency and proton shower rejection as a function of the energy of the primary particle. The scintillator trigger condition (more than 14 huts) is included. The inset shows the integral quality factor as a function of the minimum energy.**

5. with no fixed assignment of towers to input nodes, but with the order of towers interchanged at random for each event (net 8).

Tests (ii) to (iv) are alternatively performed with nets only receiving the hit information (nets 4, 5, 6, and 7) and with nets also receiving the number of reconstructed tracks (nets 1, 2, and 3).
Comparing the quality factors Q of these nets (Table 4.2) yields several important results: eliminating the whole track information considerably deteriorates the performance, showing that this criterion which signals the number of muons is indeed crucial for separation. Nevertheless, the explicit number of tracks is only one part of the relevant information used by the net. This is not a surprise because the number of tracks can to a certain degree be extracted from the number of hits in the lower layers.
As a check for the performance of the net, Fig. 4.8 (a) shows the mean number of tracks per event as a function of the network output for the showers of the test sample: events with a large number of tracks are correctly classified as proton showers. The net without any track information shows almost the same behavior, which indicates the existence of other separation criteria which are not totally independent from the track criterion. The slightly different behavior shows that the 68-17-1 net, which is able to take advantage explicitly of the track information, in fact makes more use of it.

Table 4.2: **Quality factor Q for some nets with different input information. n is the number of input nodes.**

net	n	$Q(\xi_{max})$	ξ_{max}	input information
1	68	2.8	0.17	hits and tracks...
2	68	2.4	0.17	..., but Σ hits/tower= 1
3	51	2.2	0.23	..., but upper layer omitted
4	51	2.1	0.17	hits...
5	51	1.5	0.37	..., but track hits subtracted
6	51	1.5	0.33	..., but Σ hits/tower= 1
7	34	1.4	0.43	..., but upper layer omitted
8	68	2.2	0.12	hits and tracks, but towers assigned to input nodes in random order

As the performance of nets 3 and 7 show, the number of hits in the first layer is an important information, since comparing it to the number of hits in the lower layers (after the energy cuts provided by the lead absorber) gives information about the energy distribution of the incoming particles.
The HEGRA trigger condition accepts showers over an area larger than the instrumented part of the array itself. Certain information about the shower type like the *lateral* distribution of high energy particles strongly depend on the distance from the shower core and can only be exploited if this distance is at least roughly known. Since the core position is not used as input information, a further improvement of the separation may be possible e. g. by sorting the towers in order of distance from the core, with the closest tower always connected to the first 4 input nodes, etc. However, a network trained and tested in this way does not show a better performance. This may indicate that the net intrinsically reconstructs the shower core with a sufficient accuracy and does not need the explicit core position. This is checked by training a 68-17-2 network as a plain fitting machine with the (x,y)-coordinates of the core as desired output values. Being trained using 1000 proton showers with the shower core randomized over the array, the 68-17-2 network in fact reconstructs the core position of 4000 test showers with an accuracy of $\sigma \simeq 10\,\mathrm{m}$ (Fig. 4.8 (b)). Since the towers are placed on a grid with distances of 30 m, this accuracy enables the net to exploit the lateral distribution. Net 8 is trained and tested with no fixed assignment of towers to input nodes, but with the order of the towers interchanged at random for each event, thus making a core reconstruction impossible. The performance illustrates that this information indeed plays a part in the overall separation. Note that the core reconstruction accuracy of the Geiger tower array approximately equals the array accuracy (see Section 3.2.1).
The results of this *a posteriori* analysis show that the network makes use of the different options for γ/hadron separation provided by the Geiger towers: the track number and the comparison between the layers before and after the lead absorber (what might be called the *calorimetric* signal) are indubitable parts of the separation. Furthermore, the net intrinsically determines the core position to reconstruct a shower profile and

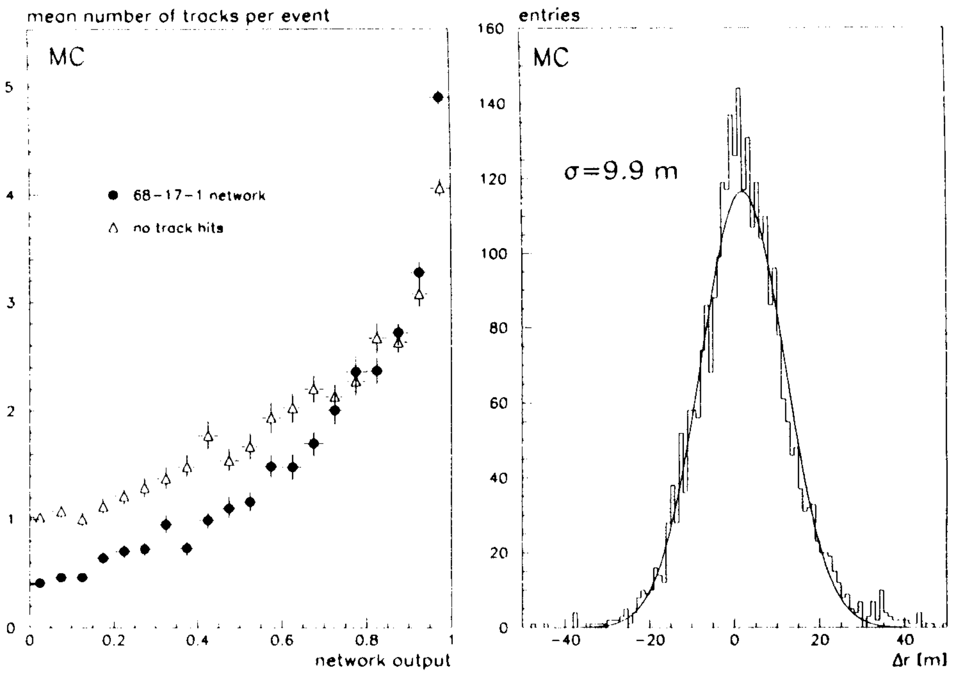

Figure 4.8: **(a) shows the mean number of tracks as a function of the network output for the 68-17-1 network and for the network without track information. (b) shows the performance of the 68-17-2 network used as a plain fitting machine for 4000 proton test showers. Δr is the difference between the reconstructed and the exact core position.**

to take into account the distance from the core when analyzing the energy content and distribution as seen by individual towers.

4.2.2 Uncertainties in the MC simulation and their effect on the network performance

As in conventional data analysis with cuts based on MC studies, the quality of MC trained neural networks necessarily depends on how far the simulation actually describes the experimental data correctly: simulation artifacts may lead to separation criteria which are worthless when applied to experimental data.
The systematic error on the γ-shower efficiency ϵ_γ resulting from two major uncertainties in the MC simulation is analyzed: the unknown spectral index of γ-showers and the description of the first interaction of the cosmic ray primary particle in the Earth's atmosphere.
The network is trained with γ- and proton showers with energies following an exponential law with spectral index 2.75, which is the value for proton showers as estimated by a fit to experimental data in the energy region from 10^{-2} to 10^{3} TeV [80]. The

spectral index for γ-induced showers is a priori unknown and may range from 2.0 to 3.0. Testing the net with γ-showers following a power law with spectral index less than 2.75 increases the γ-efficiency, since the mean energy of the test sample increases.
The systematic error on ϵ_γ due to variations of the spectral index for γ-showers in the range specified above is 6.2%. As the γ-shower efficiency is a function of the energy, and separating the low energy showers is the most difficult task, the optimal choice for the spectral index of the training data sample is 2.75, which means that the data contain equal numbers of low energy γ- and proton showers. Decreasing the number of low energy γ-showers in the training sample by using a spectral index of 2.0 leads to a deterioration of the performance on low energy data. Note that the optimal cut value ξ does not change with the use of test data with different spectral index.
The different possibilities for the simulation of the first interaction of the cosmic ray particle in the Earth's atmosphere may yield another systematic error. As described in Chapter 2, this interaction may either be calculated using the VENUS program for ultra relativistic heavy ion collision, or the Dual Parton Model (DPM). The systematic error of 4.1% on ϵ_γ due to this uncertainty is estimated by applying a test data sample based on the DPM option to the network trained using the VENUS code. The traced errors on ϵ_γ concerning the uncertainties in the MC simulation add up to about 8%, which shows that the network generalization works to a satisfying degree.

4.2.3 Comparing neural network analysis and discriminant analysis

An alternative method of parallel data analysis offered by multivariate statistical theory is discriminant analysis (DA). Applied to different data groups, it searches for the direction in data space that maximizes the separation of the groups and at the same time minimizes the variation of the data points within each group (see [114] for a detailed discussion of the method). After a projection of the γ- and proton showers onto the discriminant axis the separation problem is reduced to one dimension, and the separation capability of DA can be illustrated by plotting the fraction of γ- and proton showers above the cut value on the discriminant axis as a function of the separation cut value.
In contrast to neural network analysis, DA only allows *linear* cuts in data space. A comparison between DA and neural network analysis applied to the same data set may improve the understanding of the net performance by indicating whether non-linear cuts are actually essential for the analysis.
It is therefore important to test if DA is able to separate γ and proton-induced showers by the Geiger tower hit information. Since the number of reconstructed muon tracks is a straight-forward criterion for separation, only the 51 hit numbers are used as input information. The result therefore has to be compared with the 51-17-1 network (net 4).
DA furthermore is applied to the hidden unit activation of the 51-17-1 network before and during training. Fig. 4.9 shows the result for both input data and hidden unit activations of net 4 after 0, 10, and 100 training cycles. For both tests 2000 proton- and 2000 γ-induced showers are used.

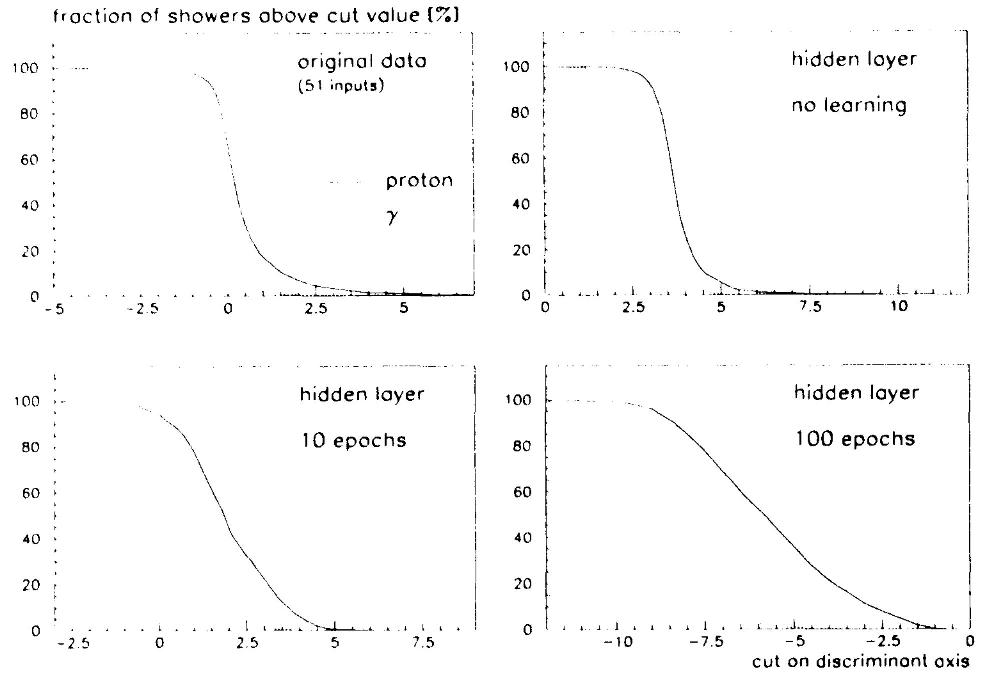

Figure 4.9: **Results of discriminant analysis: the separation problem is reduced to one dimension by projecting the showers onto the discriminant axis. The plots show the fraction of γ- and proton showers above the cut value on the discriminant axis. DA is applied to the 51 original net input values and to the hidden unit activations after 0, 10, and 100 learning cycles.**

The performance of DA if applied to the original input data is only poor. DA with its linear cut in data space does not allow any separation using the hit information. As expected, the relevant information for γ/hadron separation (apart from the muon veto) does not directly come from the number of hits in the Geiger tower layers, but has to be extracted by arithmetic combination of the hit numbers, which is impossible for DA, but easily achieved by the use of multi-layer networks: after only 10 learning cycles it has transformed the input information in a way that successfully allows γ/hadron separation. This illustrates that the analysis takes advantage of one of the main features of the net approach, the possibility of having nonlinear boundaries in parameter space.

Chapter 5

Application to data

This chapter is the link between the description of the separation method and the results achieved by its application. It aims at an understanding of the neural network behavior when confronted with experimental data instead of MC simulated showers.
The γ/hadron separation technique developed in the previous chapter has only been tested with MC showers up to now. As in all data analysis based on MC simulation, it is not a priori clear whether the experimental data are correctly described by the MC to an extent that allows to exploit the criteria used for separation. Apart from "typical" shortcomings of the MC technique, e.g. processes not correctly taken into account or complex calculations oversimplified due to limited computer power (or just our limited knowledge), we have to consider that the detector simulation does not yet include effects resulting from the performance of the Geiger array. Compared to an ideal detector with $17 \times 6 \times 160$ fully efficient Geiger tubes, the actual status of the array with a certain number of non-working tubes, layers, or even towers will certainly affect the quality of the separation. It has to be analyzed in how far the separation quality decreases with Geiger tower quality and which criteria allow to select runs of sufficient quality. Here, the track finding capability of the Geiger towers will help to estimate the quality of all array components used in the following analysis.
After a study of the experimental effects which influence the separation, the network output of experimental data and MC showers is compared, yielding an upper limit on the isotropic γ-radiation. In addition, we search for an enhanced γ-flux from the Galactic plane.

5.1 Understanding the data

5.1.1 Network output and optimal cut value

A crucial parameter of any neural net based analysis is the cut ξ_{cut} in the network output which is chosen to separate the data types. Although any result derived from the analysis, e.g. a γ-flux from point sources, has to be independent from ξ_{cut} after correction for the cut-dependent γ-efficiency, the quality factor Q and thus the signal-to-noise ratio may strongly depend on ξ_{cut}. The possibility of smoothly adjusting the efficiencies to the actual requirements of the analysis by varying ξ_{cut} may be regarded

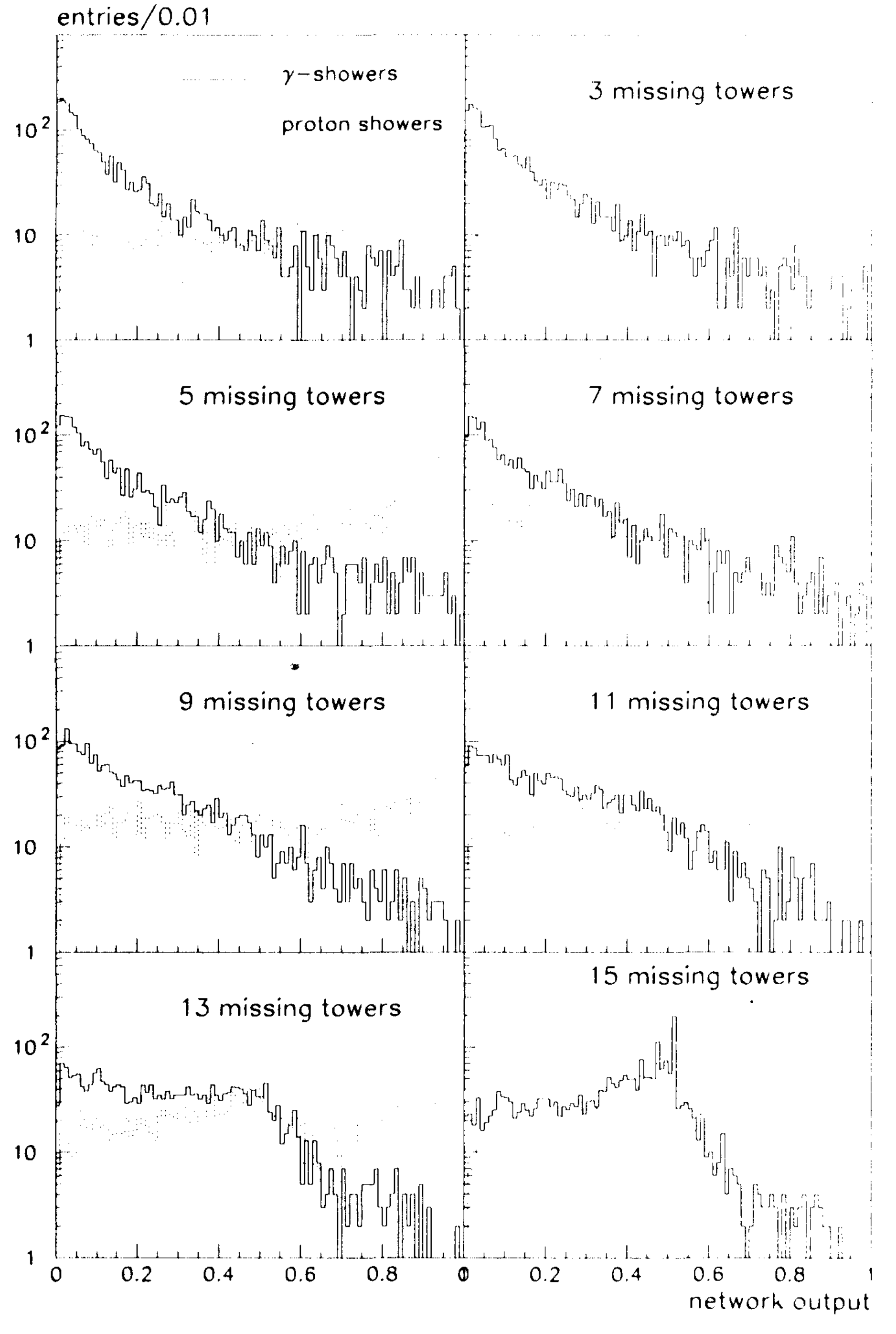

Figure 5.1: **Network output distribution for MC γ- and proton showers after artificially disabling towers.**

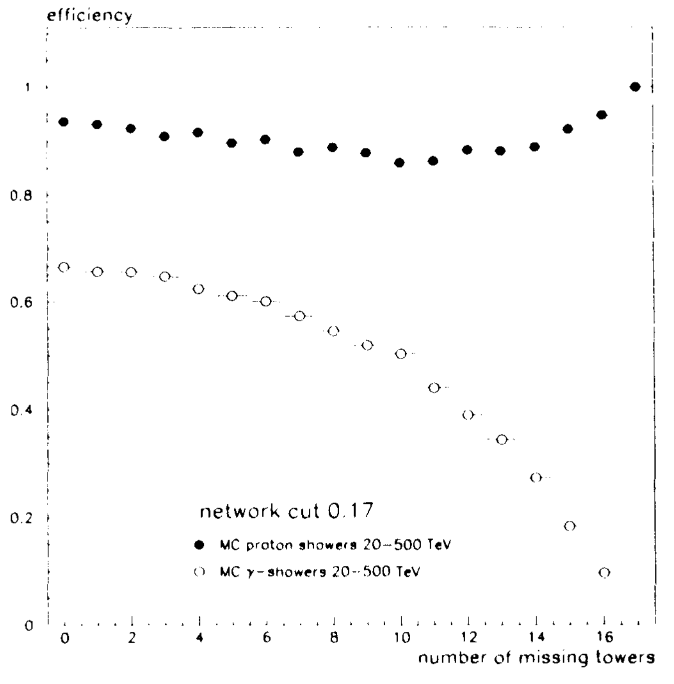

Figure 5.2: **γ-efficiency and proton rejection as a function of the number of non-working towers (average values).**

as an additional major advantage of the neural net approach, as it allows the use of the same net for different goals, but the dependence of the results on ξ_{cut} of course has to be studied.

As shown in Fig. 4.4, there is an optimal value for ξ_{cut} which maximizes the quality factor Q. In order to analyze whether this value is stable when data quality changes, we first study the effect of missing towers on the shape of the γ- and proton shower network output distribution. Fig. 5.1 illustrates that even with as much as 5 non-working towers, the distributions remain largely unaffected. This is very important, as for the data used in the following analysis up to 3 towers per run turned out to be completely inefficient due to hardware problems during the construction phase of the Geiger tower array and due to maintenance problems. Fig. 5.2 summarizes the change in γ- and proton efficiency with fixed network cut as a function of the number of non-working towers. As the actual decrease in γ-efficiency slightly depends on the position of the non-working tower within the array, Fig. 5.2 shows mean values with the excluded towers chosen at random.

Whereas the network performance remains rather stable in case of *completely missing* information, it is much more difficult to estimate the effect of missing layers, octotubes, or single tubes, as this may provide the net with *wrong* information. Inefficient layers below the lead absorber may e.g. imitate γ-showers with their small amount of

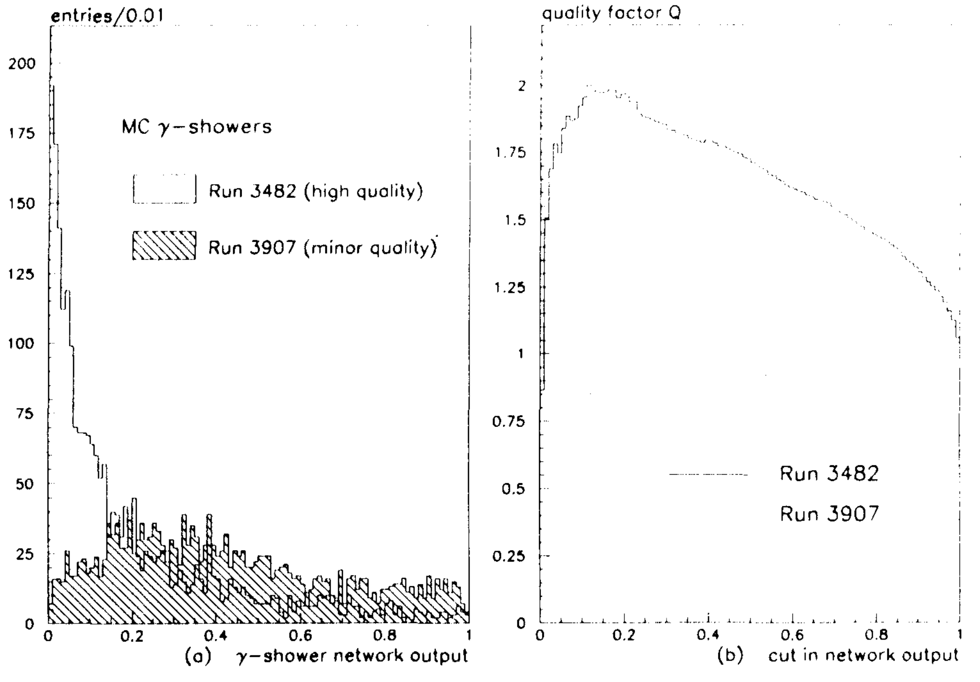

Figure 5.3: **(a) Network output for MC γ-showers and (b) quality factor Q as a function of the cut ξ_{cut} in the net output after folding with the Geiger tube efficiencies of a high and low quality run.**

high energy particles penetrating the lead. On the contrary, events with noisy Geiger tubes in the lower layers may be interpreted as hadron showers. We therefore expect non-working *parts* of towers to be much more dangerous than simply missing towers which do not fake separation criteria.
To estimate the influence of the actual running conditions on the separation quality, we adapt the MC showers to the actual tower status by applying the following procedure: for a pre-defined number of events (20 000), the number of hits of each Geiger tube is compared to the number of hits expected for a fully efficient Geiger tube. The expectation values are derived from the experimental data and naturally depend on the layer, the position of the Geiger tower, and the trigger condition (during AIROBICC runs, the expected number of hits per tube is lower for the same number of events, as a larger number of low energy events trigger data taking). These Geiger tube efficiencies are then included in the full Geiger tower detector simulation, so the MC data represent the actual status of the detector matrix as closely as possible, and the network performance can be checked for every individual run.
To illustrate the power of this method, Fig. 5.3 (a) shows the network output distribution of MC γ-showers after folding with the Geiger tube efficiencies for a run with high and low data quality. As expected, missing parts of the tower information affect the

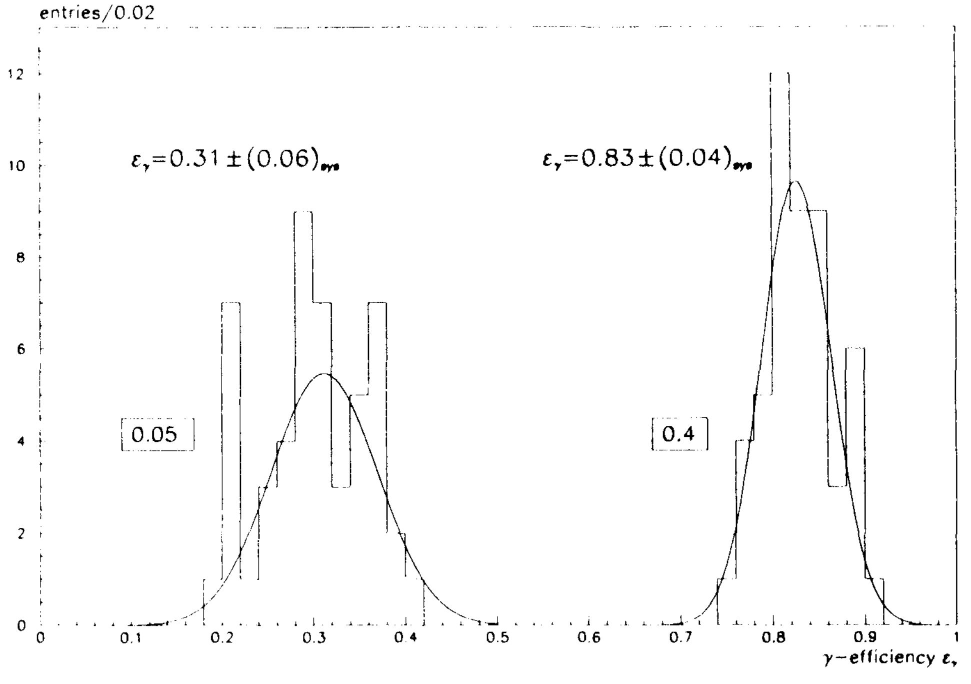

Figure 5.4: **γ-shower efficiency of 50 runs after adapting the MC data to the Geiger tower performance for ξ_{cut} = 0.05 and 0.4.**

network separation harder than completely missing towers. In addition, the optimal cut value ξ_{cut} and the quality factor vary with data quality due to the different shapes of the network output distribution. Nevertheless, Fig. 5.3 (b) shows that even for runs with low quality, network cuts at sufficiently high values of ξ are expected to give rather stable results, which is not true for cut values below $\xi = 0.2$, where minor data quality allows no separation at all. As shown in Chapter 4, this is a general feature of the neural net based γ/hadron separation. For events which are erroneous due to bad Geiger tower performance the net shows the same behavior as for events with low information content: they populate an intermediate output region at about 0.6 which neither indicates γ-likeness nor hadron likeness.

As in data analysis, changes in data quality to a certain degree cannot be avoided, network cuts at $\xi_{cut} = 0.4$ are more sensible than cuts at low output values, although we lose significance for those data with sufficient quality for a cut at small ξ. To estimate the stability of the data quality, ϵ_γ is calculated for 50 different runs by adapting the MC data to the actual Geiger tower quality. For a network cut $\xi_{cut} = 0.4$, the result is rather stable, with a systematic error of less than 5 % (Fig. 5.4). In contrast to this, the systematic error on the γ-efficiency when choosing a cut value $\xi_{cut} = 0.05$ is of the order 20 %.

Furthermore, cleaning the data from noisy Geiger tubes turns out to be crucial for a

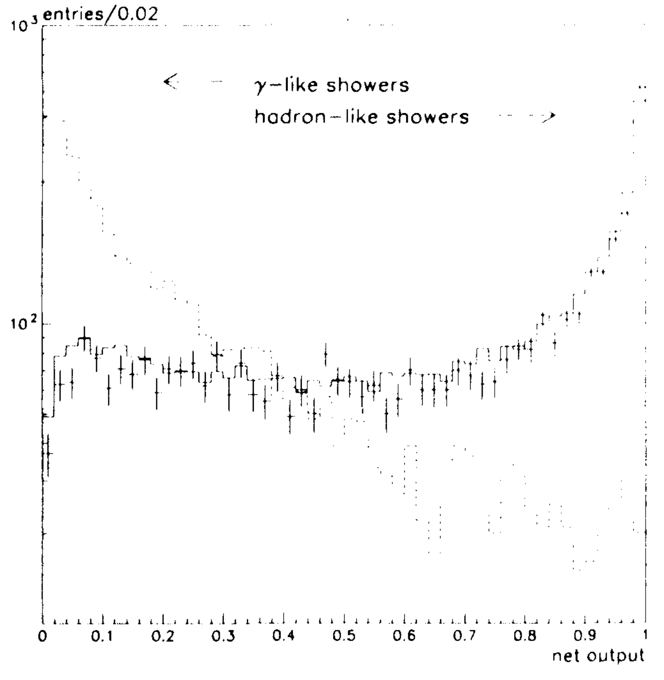

Figure 5.5: **Network output for experimental data (solid line) and MC γ showers (dotted line) and proton showers (dots with error bars).**

stable separation. All Geiger tubes which show more than 1.5 times the number of hits expected for a correctly working tube are excluded.
As we now have a procedure to adapt the MC showers to the actual running conditions, thus including most detector effects in the tower simulation, it is possible to compare the network output of MC and experimental data. This is a first test for the neural network separation, as the major part of the data is supposed to be background. Fig. 5.5 shows the network output for 4425 proton- and 4876 γ-induced MC showers between 20 and 500 TeV (differential spectral index 2.75) fulfilling the scintillator trigger condition and the Geiger tower cut (at least 6 non-zero towers) together with the output distribution for experimental data, normalized to the number of proton showers. There are two major results:

- The MC proton showers describe the experimental data to a satisfying degree,

and

- a description of the data is possible without considering γ-showers at all.

The good correspondence between MC and experimental data indicates that the MC simulation based on CORSIKA generation and GEANT tower and scintillator simulation gives reliable results at least in first order approximation. In fact, the lack of correspondence between experimental data and *pure* MC (without trigger and especially without adaptation to the data quality) indicates that the network output *is* sensitive to incorrect and incomplete data simulation.

5.1.2 Energy threshold

One of the most critical aspects of air shower physics is the sketchy knowledge we have of a very important shower property, the energy of the primary particle. The only way of getting an estimate on this quantity is to use the loose correlation with the shower size N_e, which is a parameter of the Nishimura-Kamata-Greisen formula (Eq. 3.5) fitted to the particle density of the scintillator huts (see Chapter 3).
The energy threshold of an air shower detector is a very important parameter which is necessary for flux (or flux upper limit) calculations and for the interpretation of results in multifrequency spectra. In this subsection, we will study the HEGRA energy threshold for proton- and γ-induced air showers using the MC data sample described above: this sample tries to imitate the data as closely as possible, thus the zenith angle follows the distribution for experimental data, the core is distributed at random, and the energy follows a power law from 10 to 500 TeV (γ-showers) and 20 to 500 TeV (proton showers). Although the spectral index of γ-showers is unknown, 2.75 is chosen both for proton- and γ-showers.
Four different trigger conditions which play a major part in the subsequent analyses are studied:

1. the basic condition with at least 6 non-zero Geiger towers to allow for γ/hadron separation,
2. the scintillator trigger condition ($\geq$ 14 huts),
3. the scintillator trigger condition and the Geiger tower condition, and
4. an additional cut on the shower size, $\log N_e \geq 4.0$.

Fig. 5.6 shows the trigger efficiency as a function of the energy of the primary particle for MC proton and γ-showers. It is obvious that it is not possible to talk about a "threshold energy", as the efficiency increases rather smoothly with energy. We follow the convention of fitting a sigmoid function

$$\epsilon_{trig} = \frac{1}{2}\left[1 + \tanh\left(\frac{E - E_{thresh}}{T}\right)\right] \tag{5.1}$$

to the trigger efficiency in order to define the 50 %-point with $\epsilon_{trig} = 0.5$ as the threshold energy E_{thresh}. With this definition, whether sensible or not, it is at least possible to compare proton and γ-thresholds for different trigger and cut conditions. Tab. 5.1 summarizes the results for the four cuts described above.

1. The intrinsic Geiger tower threshold is 15 TeV for both shower types, showing that running the Geiger tower array in combination with the low threshold detectors of the HEGRA array, like AIROBICC and the Čerenkov telescopes, is physically sensible: although γ/hadron separation power is only marginal at these

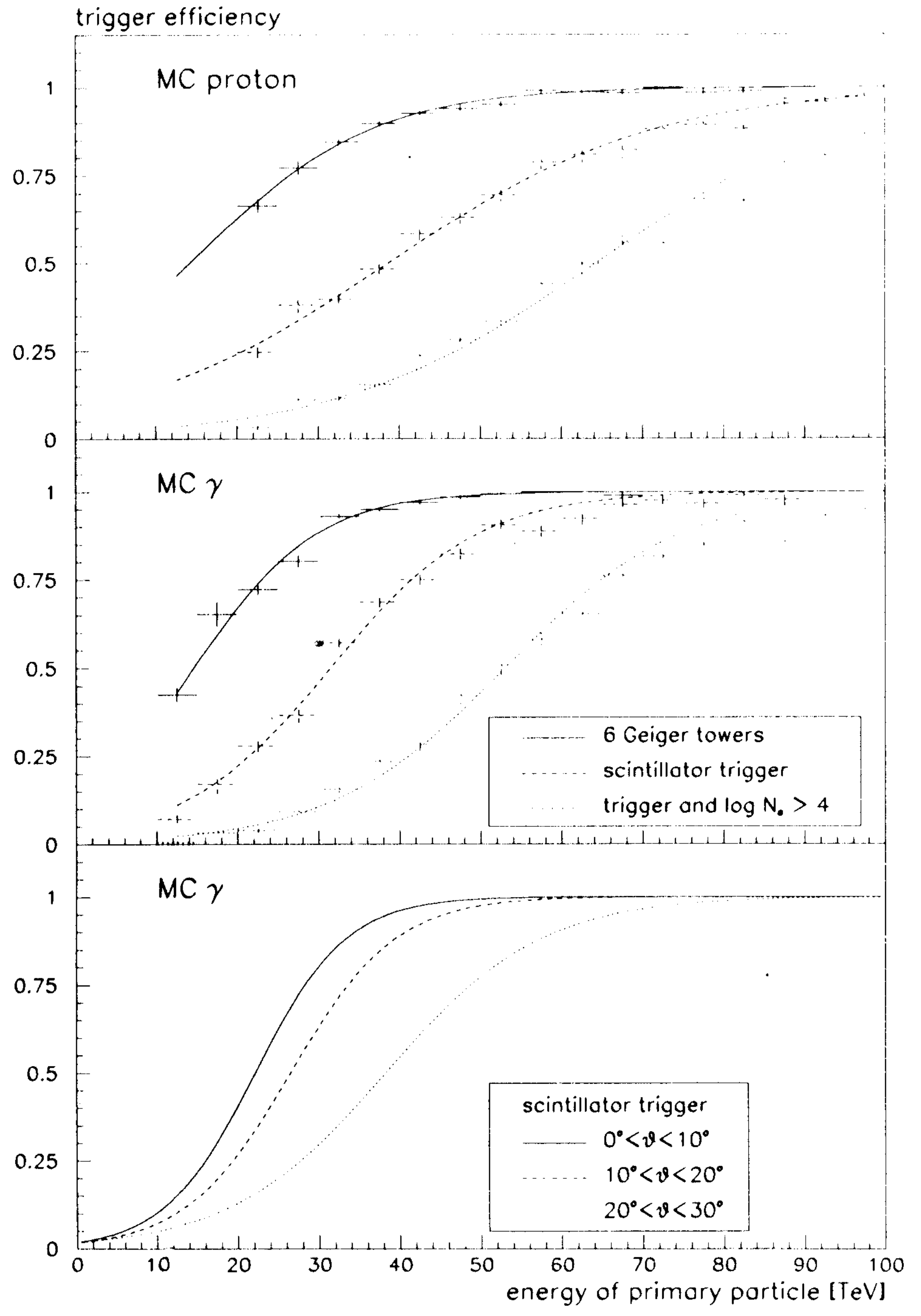

Figure 5.6: **MC estimation of the trigger efficiency for proton- and γ-showers.**

energies, the Geiger tower data may be used to cross-check these instruments independently. This is a possibility of fixing the ill-understood systematics of the Čerenkov technique and its simulation to the robust track reconstruction and the tower simulation based on a well-established MC code.

2. Including a simulation of the scintillator trigger condition yields energy thresholds for γ- and proton-induced showers which differ by about 20 % due to the different particle content, which on average is higher for γ-induced showers (see e. g. Fig. 3.10).

3. As mentioned in Chapter 4, an additional cut on the number of Geiger towers does not increase the threshold energy, thus this condition is not explicitly shown in Fig. 5.6.

4. The cut on the shower size, $\log N_e \geq 4.0$, increases the γ-shower threshold energy to about 50 TeV, which is a region where a stable γ/hadron separation is guaranteed according to Fig. 4.6.

Table 5.1: **MC estimation of the threshold energy (see definition given in the text) for different trigger conditions and cuts.**

	Energy threshold E_{thresh}[TeV]	
	proton showers	γ-showers
≥ 6 Geiger towers	14	15
scintillator trigger (≥ 14 huts)	39	32
scintillator trigger and ≥ 6 Geiger towers	39	32
scintillator trigger and $\log N_e \geq 4$	64	53

Fig. 5.6 furthermore shows that E_{thresh} strongly depends on the zenith angle of the incoming primary. Due to the increasing atmospheric depth, E_{tresh} increases with θ.
It is important to interpret these results correctly. A cut in N_e is only a very weak energy cut, especially as due to the steep spectrum a considerable amount of showers with energy below E_{thresh} pass the trigger. Fig. 5.7 shows the correlation between $\log N_e$ and the primary particle's energy for MC γ-showers. Although the mean values clearly correlate, fluctuations for single showers are large, and it is very dangerous to connect a cut in N_e directly to an energy cut, implying that e. g. $\log N_e \geq 4.0$ means restricting the analysis to showers above 50 TeV.
Nevertheless, a cut in N_e to discard events with small shower size is justified in order to guarantee a good reconstruction quality and a stable γ/hadron separation, as both depend on the *information content* of the event, which is directly connected to N_e. To illustrate this, Fig. 5.7 shows the γ- and proton efficiency of the network as a function of N_e instead of energy (compare to Fig. 4.6). As we have the same dependence on N_e as on energy, both approaches are equivalent. Only when connecting the shower size

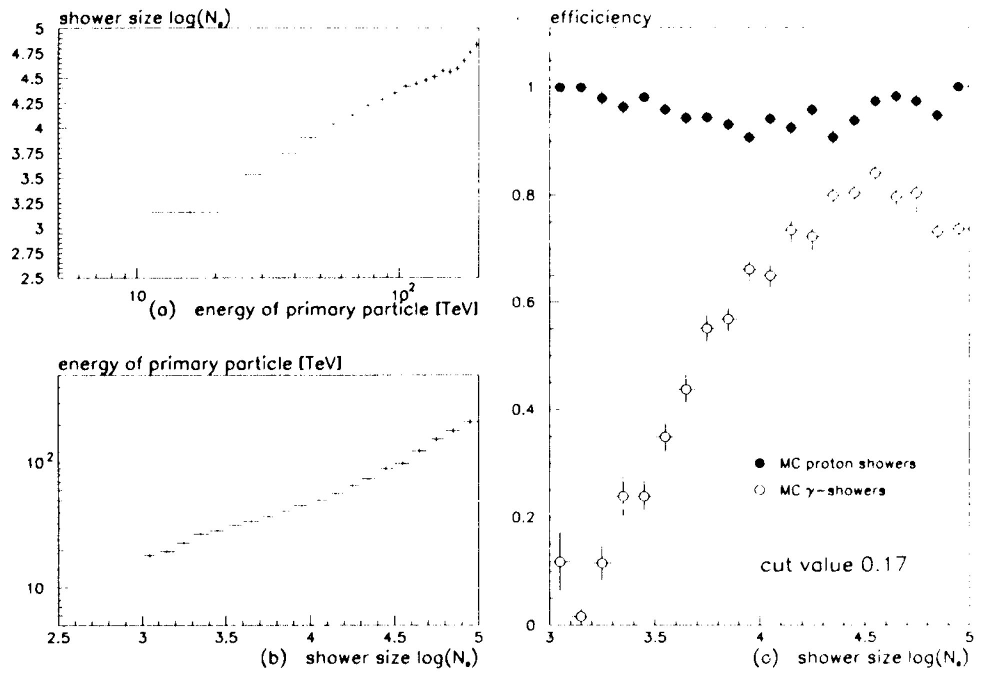

Figure 5.7: **Correlation between shower size N_e and energy of the primary particle (a and b), and network γ-and proton efficiency as a function of the shower size (c).**

to a threshold energy, we have to bear in mind the shape of the trigger efficiency in Fig. 5.6, and the large uncertainty has to be considered when giving systematic errors on E_{tresh}.

5.1.3 Data quality checks

Apart from γ/hadron separation, the major advantage of the Geiger tower subarray is the possibility of checking the pointing accuracy of the scintillator and AIROBICC array on a run-to-run-basis. In contrast to the analysis of the moon shadow, where it is crucial to have sufficiently high statistics, the large number of fitted tracks easily allows to see deviations in the pointing accuracy for each individual run, i.e. on time-scales of hours.

As a single Geiger tower only allows to measure the projection of the track onto the plane perpendicular to the Geiger tubes, the checking of the absolute pointing of the scintillator and AIROBBIC matrix is difficult and requires detailed studies of systematic biasing due to the time-dependent quality of the Geiger array performance [115]. Nevertheless, information about the data quality can be extracted from the projected track angles, too. Fig. 5.8 shows the difference $\Delta\theta_{proj}$ between all reconstructed angles of Geiger tower tracks and the corresponding projection of the shower direction as de-

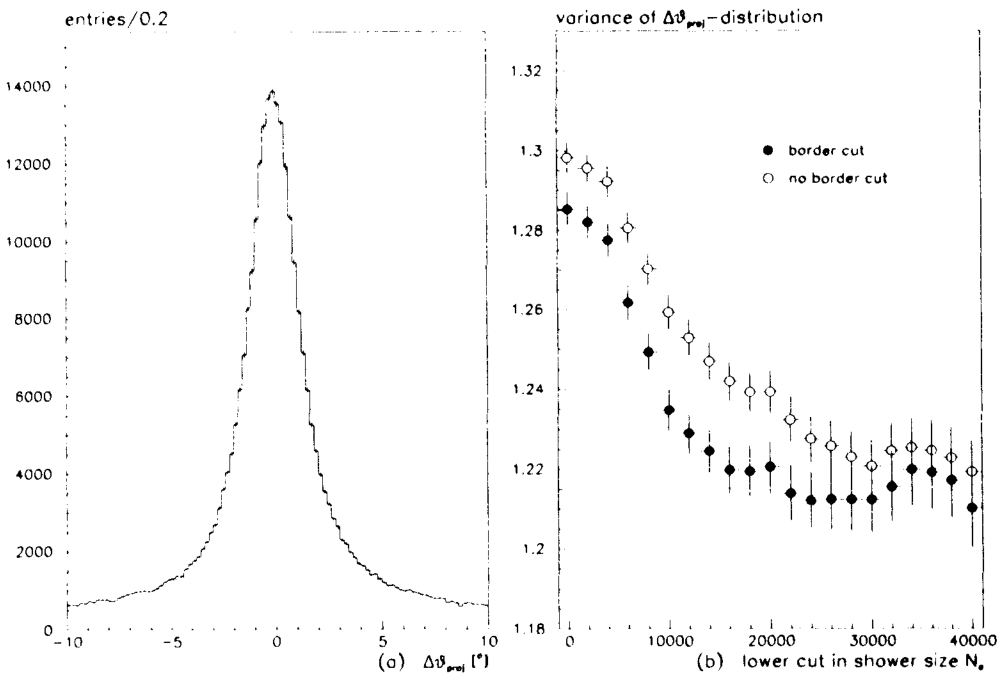

Figure 5.8: **(a) Difference $\Delta\theta_{proj}$ between all reconstructed angles of Geiger tower tracks and the corresponding projection of the shower direction as determined by the scintillator array for a typical run (503 275 events). (b) Variance of $\Delta\theta_{proj}$ as a function of the minimum shower size N_e with and without additional border cut.**

termined by the scintillator array for a typical run ($\simeq$ 500 000 showers before quality cuts) with 421 856 tracks reconstructed by the track finding algorithm. The distribution indicates that only a fraction of these tracks actually correlate with the shower direction. It is fitted by

$$N_{\Delta\theta} = N_0\, e^{-\frac{\theta^2}{\sigma^2}} - a\,\theta^2 \;, \tag{5.2}$$

with the parabola term approximately describing the background. The variance of the Gaussian is 1.25 ± 0.04. To estimate roughly the contamination by background tracks, we integrate the parabola term: from the total number of 220 000 tracks which correlate with the shower direction, i.e. fulfill the condition $|\Delta\theta_{proj}| \leq 2\sigma = 2.5°$, 45 000 tracks, hence a fraction of 0.2, are background. This is in agreement with MC predictions [87]. The background is made up mainly of random tracks not belonging to the triggering shower but crossing the tower during the sensitive period of $3\,\mu$s.
The amount of electromagnetic punch-through ($e^{\pm}, \gamma$) (which does not correlate with the shower direction as closely as the muons) strongly depends on the distance of the tower from the shower core and ranges from $\simeq 10\,\%$ for core distances of less than 20 m to below $5\,\%$ at higher distances [87].
A small fraction of the background is due to unavoidable shortcomings of the track

finding algorithm, which sometimes fits erroneous tracks, especially near the shower core where the hit pattern is rather complex.
The variance of the Gaussian depends on the cuts applied to the data. It decreases from 1.36 ± 0.03 for all showers to 1.25 ± 0.04 for showers after quality cuts, which include a cut on the zenith angle, $\theta \leq 40°$, and a so-called border cut which excludes events with a distance of less than 20 m from the (geometrical) border of the array. The border cut is introduced to avoid a typical shortcoming of core finding algorithms: showers with core outside the array are interpreted as showers *within* the array, but near the border. This leads to an increase in the number of reconstructed cores with decreasing distance to the array border which is considerably higher than expected on the basis of the geometrical increase. For the Geiger tower γ/hadron separation the border cut is crucial, since the separation quality decreases with distance from the tower sub-array.
Fig. 5.8 (b) shows the dependence of the $\Delta\theta_{proj}$-variance on the lower cut in shower size N_e. The accuracy of the shower reconstruction increases with shower size as expected on the basis of MC and moon shadow analysis. The stable value for $N_e \geq 15\,000$ may either indicate that the angular resolution does not increase further with larger shower size or that the comparison between muon track and shower direction is no longer sensitive to improvements, as the intrinsic limit of this method is reached. Without the border cut, the variance increases by $\simeq 0.1°$ due to the larger distance of the muon track from the shower core.
It is important to check the time variance of the parameters of this Gaussian distribution for the data used in the following analysis, as deviations from the average behavior may indicate deteriorated performance of the Geiger towers or the scintillator array. The relevant parameters, mean value and variance of the Gaussian, are shown for each run (and thus as a function of time) in Fig. 5.9. Their distribution is shown additionally in the insets.
As a striking result, the mean value does not center at 0, but is significantly shifted. The actual value of this mean value strongly correlates with the status of the Geiger tower array, i. e. mainly with the number of non-working towers.
The tower array worked with some stability up to run 110, when for a few runs 3 towers were defect and the performance in general began to be instable.
In contrast to this, the variance is only marginally affected by the status of the Geiger array. The large deviation from the mean value for runs 5 to 25 earlier was traced as an error in the scintillator reconstruction program significantly deteriorating the angular resolution (these runs were added in Fig. 5.9 to illustrate the capability of the Geiger array in monitoring the resolution, but were excluded in the following analysis).
In summary, monitoring the shape of the $\Delta\theta_{proj}$-distribution allows to check both the quality of the Geiger array (mean value) and the scintillator reconstruction (variance).

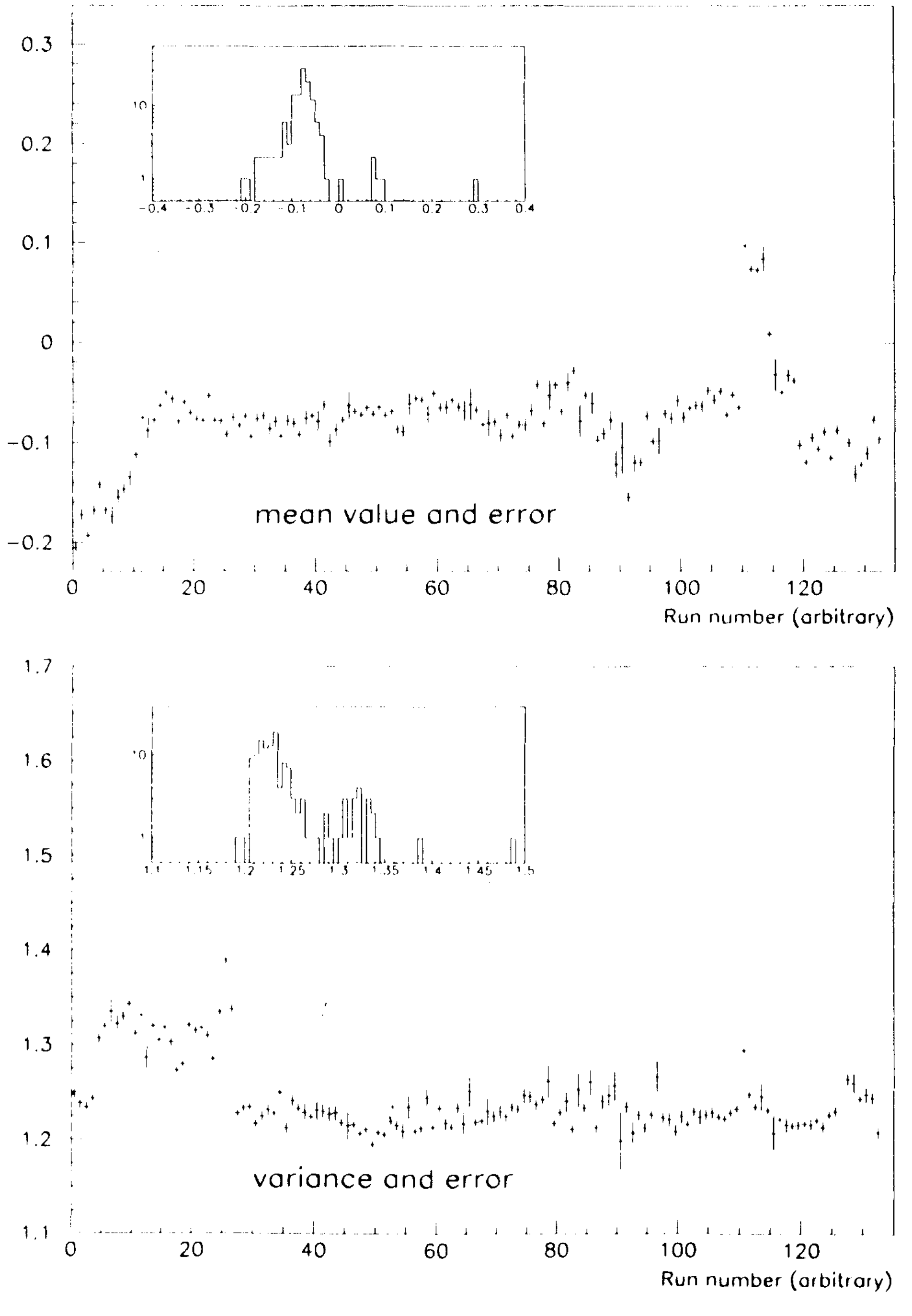

Figure 5.9: **Mean value and variance of the $\Delta\theta_{proj}$ distribution as a function of the data run. The insets show the mean value and variance distributions.**

5.2 Search for diffuse cosmic γ-radiation

As a first application, we use the neural net based γ/hadron separation to search for diffuse γ-ray fluxes of Galactic and extragalactic origin.
Diffuse fluxes of γ-rays are expected from interactions of the highest energy cosmic rays with the cosmic background radiation and interstellar gas. If compact extragalactic sources of γ-rays exist, an *isotropic* diffuse γ-background may result from the interaction of high energy protons with the photons of the microwave background, whereas a diffuse γ-flux concentrated along the Galactic disc may arise from interactions of cosmic rays with gas and dust.
In this section, we use Geiger data taken in November and December 1994 and between February and April 1995 to search both for diffuse isotropic γ-radiation and an enhancement of γ-showers from the direction of the Galactic disc.

5.2.1 Upper limit on the isotropic γ-flux

A very important conclusion from Fig. 5.5, which compares the network output for experimental data to the output for MC showers, is that it is not necessary to include γ-rays in the cosmic radiation to explain the experimental data, as they are well described by proton showers alone.
The fraction f_γ of γ-rays in the cosmic radiation in fact has not been measured up to now, and only upper limits in different energy regions have been derived [116, 103]. The search for the isotropic γ-radiation is nevertheless important as it might provide an indirect step towards the explanation of the origin of cosmic rays and especially of the highest energy events above 100 EeV (see [117] and references therein). Apart from shock acceleration in AGN, also exotic scenarios like the collapse of so-called topological defects are under discussion. Both models differ in the steepness of their γ-spectra and thus in the total amount of γ-rays at high energies.
A rather high isotropic γ-flux is predicted by models based on collapsing topological defects, which are the results of phase transitions in the early universe, caused by spontaneous breaking of GUT symmetries [118]. They may show up as cosmic strings or magnetic monopoles which decay or annihilate in so-called X-particles, e.g. gauge and Higgs bosons or superheavy fermions. As they typically decay into a lepton and a quark with the quark hadronizing into nucleons and pions, the X-particles lead to injection of γ-rays, electrons, and neutrinos from pion decay. The injection spectra caused by topological defects are harder than those caused by Fermi shock acceleration in AGN, thus high values of f_γ would favor a topological defect origin of the highest energy cosmic ray particles rather than acceleration by shock waves in AGN. $f_\gamma \simeq 0.04$ at HEGRA energies is predicted in certain topological defect scenarios [119], whereas more conventional models extrapolating the observed cosmic radiation above 10^{18} eV to higher energies derive values of about 10^{-5} [120].
New calculations of the expected γ-ray flux for several topological defect scenarios based on cosmic strings [121] and annihilation of magnetic monopole-antimonopole pairs [122] are given in Sigl et al. [123], and their predictions are shown in Fig. 5.10. Depending on the strength of the extragalactic magnetic fields, $f_\gamma \simeq 0.1$ is predicted at

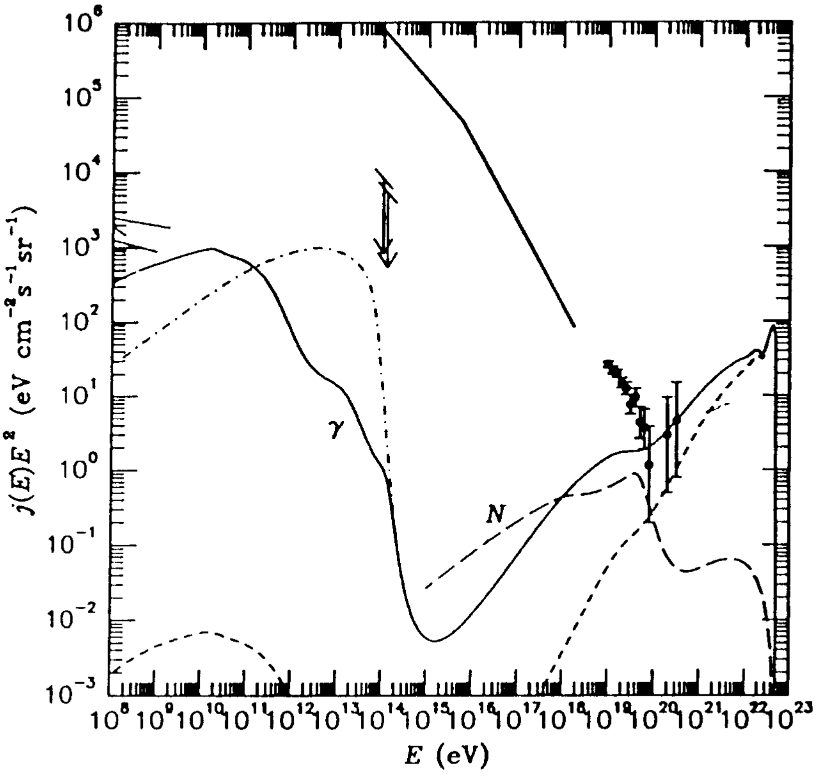

Figure 5.10: **Differential flux of nucleons and γ-rays in topological defect models based on cosmic strings or monopole annihilation. For the dash-dotted line, the infrared-to-optical background has been neglected. Experimental data above 10 EeV (Fly's Eye [124], AGASA [125]) and power law fits to the charged cosmic ray flux (thick solid line) are added. Upper limits in the GeV region (SAS-2, EGRET) are indicated as dotted lines, and the arrows show the HEGRA upper limits. Taken from [123].**

10 EeV, whereas at TeV energies, f_γ is of the order 10^{-3} to 10^{-4}, taking into account the inevitable infrared absorption.

Although the highest values for the isotropic γ-flux are thus predicted at energies above EeV, the HEGRA energy region also is of special importance, as below 100 TeV the γ-radiation of electromagnetic cascades produced by cosmic radiation above the Greisen cutoff is supposed to pile up. The Greisen cutoff at $6 \cdot 10^{19}$eV is the energy where the universe becomes opaque for baryons as they suffer pion photo-production with the microwave background photons

$$p\,\gamma_{3K} \longrightarrow \pi\, N \tag{5.3}$$

(thus the Greisen cutoff is the baryonic equivalent to the γ-cutoff due to microwave background photons at about 100 TeV). As the pions decay into γ's, $e^{\pm}$, and neutrinos, electromagnetic cascades develop and produce a considerable number of photons at lower energies. As soon as the photon energy drops below the 100 TeV threshold, interaction with the microwave background is not possible any more, and the photons should therefore pile up in the energy region just below 100 TeV. Any detection of the isotropic γ-radiation at energies between 50 and 100 TeV (the "cosmological window")

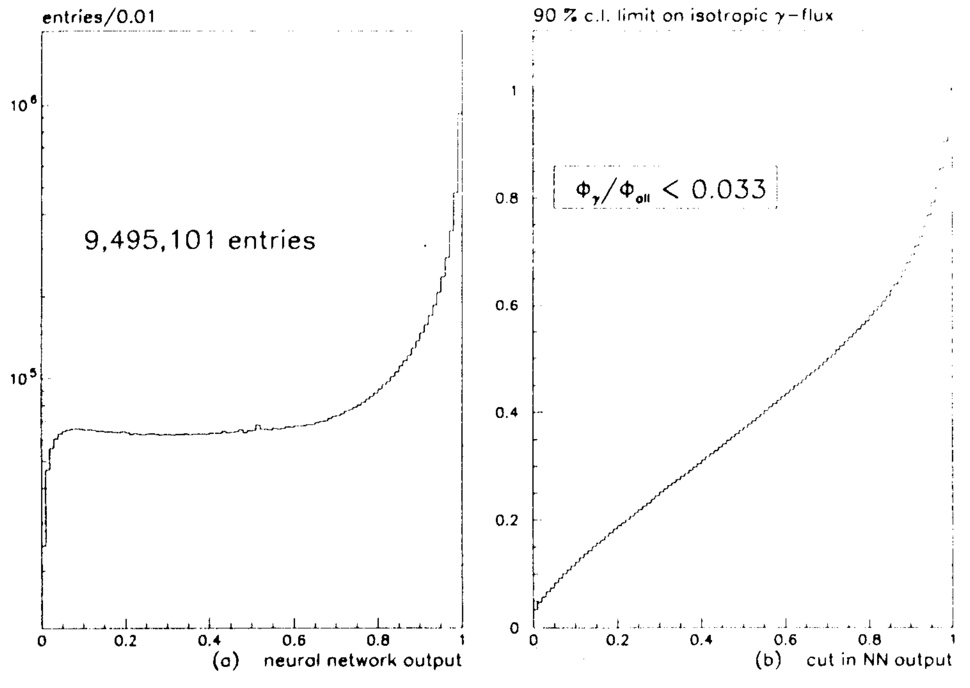

Figure 5.11: **(a) Network output for the events passing the quality criteria for the source search analysis. (b) 90 % confidence level upper limit on the fraction of γ-induced showers to the integral cosmic ray background as a function of the cut in the neural network output.**

would therefore allow conclusions as to the origin of cosmic rays above the Greisen cutoff.

To derive an upper limit on the isotropic γ-ray flux in the energy region between 50 and 100 TeV, we apply the neural network γ/hadron separation to 9 495 101 events chosen for their high data quality. Showers with zenith angle $\theta \geq 40°$ and a shower size $N_e \geq 10\,000$ are discarded as well as showers with a distance of less than 20 m from the border of the array. All cuts guarantee a stable γ/hadron separation.
We assume that all showers with net output below the cut value ξ_{cut} are γ-showers. This is a very conservative assumption, as MC studies show that even for very small values of ξ_{cut} the region below ξ_{cut} is dominated by hadron showers. Nevertheless, the number of experimental showers exceeds the MC sample which may be used to calculate the hadronic contamination below ξ_{cut} by more than 3 orders of magnitude and thus does not allow to give reliable results. Furthermore, extreme network cut values are supposed to leave behind rather untypical "γ-like" hadron showers.
Using the γ-efficiency as a function of ξ_{cut} as shown in Fig. 4.4, but after folding with the actual Geiger array performance, the 90 % confidence level upper limit [126] on

$f_\gamma = \Phi_\gamma/\Phi_{all}$ can be calculated as a function of ξ_{cut} (see Fig.5.11 (b)). For $\xi_{cut} \to 0$, a value of

$$f_\gamma^{90\,\%} \leq 0.033 \tag{5.4}$$

is derived. This value is higher than the present limit of $f_\gamma^{90\,\%} \leq 0.010$ published by HEGRA [116], which is based on the analysis of 2 796 events taken in combination with AIROBICC, but in contrast to the AIROBICC analysis, the Geiger/scintillator analysis in fact covers the whole northern sky as visible for HEGRA and is thus a true "isotropic" flux limit.

This and especially the AIROBICC upper limit is well on the way towards ruling out certain topological defect scenarios predicting high values for f_γ [119], but it should be stressed that this interpretation is dubious as long as the infrared background is not taken into consideration. If it actually has the strength given in Fig. 2.8, the "cosmological window" below 100 TeV in fact does not exist. This is illustrated in Fig. 5.10, where the γ-ray flux at energies from GeV to 100 TeV is calculated with and without accounting for the absorption by photons of the infrared-to-optical background (dash-dotted resp. solid line). Absorption decreases the theoretical γ-flux by 3 orders of magnitude. As a consequence of cascading processes, the absorbed TeV γ-rays pile up below 10 GeV, thus upper limits in this energy region, e. g. by SAS-2 [127] and by EGRET [128, 129], are of great importance. By now they rule out models predicting high values for f_γ [130, 131]. Nevertheless, as shown in Fig. 5.10, scenarios like magnetic monopole annihilation are still unconstrained by current upper limits.

5.2.2 Search for γ-emission from the Galactic plane

Apart from the isotropic emission of extragalactic origin, the most prominent diffuse γ-ray flux correlates with the disc of our Galaxy.

In almost all energy regions, the Galactic plane shows strong large scale emission, which is supposed to arise from the interaction of primary cosmic rays with interstellar gas and the interstellar radiation field. Bremsstrahlung and inverse-Compton scattering are thus the main processes. As a consequence, the γ-ray flux should reflect the distribution of interstellar material, and early measurements of COS-B and SAS 2 have been used to derive the Galactic hydrogen density [132, 133].

More recently, the Galactic plane has been subject of intense studies with the instruments on board the CGRO. Spectra taken with the Oriented Scintillation Spectrometer OSSE (50 keV to 10 MeV), the Imaging Compton Telescope COMPTEL (1 MeV to 50 MeV), and EGRET (30 MeV to 30 GeV) cover the hard X-ray to γ-ray region. Apart from the bright continuum emission from the disc, a few point sources like the Crab supernova remnant can be resolved.

The spectra of the three experiments is found to be consistent with combined bremsstrahlung and inverse-Compton scattering [134]. Whereas the bremsstrahlung component drops off quickly at higher Galactic latitudes, the inverse-Compton component has a broader latitude profile than the gas component and thus dominates for $|b| \geq 5°$. At higher energies, the inverse-Compton radiation is expected to become more dominant because of its harder spectrum, and EGRET in fact observes a flattening of the diffuse

γ-ray spectrum above 1 GeV [135].
Searches for an enhanced γ-flux from the Galactic disc at energies above TeV have up to now only placed upper limits on the ratio of γ-rays to hadronic cosmic rays, I_γ/I_{CR}. The Whipple group [136] gives a limit of $I_\gamma/I_{CR} < 0.01$ at 1 TeV, and the CASA-MIA air shower array places a limit of $I_\gamma/I_{CR} < 8 \cdot 10^{-5}$ for $E > 200$ TeV and $|b| \leq 10°$ by making use of their muon-based γ/hadron separation [103].
We use the Geiger tower data sample to search for diffuse Galactic γ-ray emission in the HEGRA energy region above 30 TeV. Due to the latitude of 28.8°, HEGRA probes the Galactic disc in the region $30° < l < 220°$ in Galactic longitude and therefore does not observe the Galactic center region. In contrast to the analysis of the isotropic radiation in Section 5.2.1, we can now considerably improve our sensitivity by using events of non-Galactic origin ($|b| > b_{plane}$) to estimate and subtract the hadronic background (the so-called ON-OFF method).
It is crucial to avoid systematic errors due to the dependence of the detector performance and the γ/hadron separation on local coordinates (θ,ϕ,t), with t being the hour of the day. In order to obtain the same (θ,ϕ,t)-distribution for on-source and off-source data, we apply the following method: for each event with $|b| < b_{plane}$, a background event with approximately the same local coordinates is taken at random from a background pool with events meeting $|b| > b_{plane}$. The same cuts are applied to the source events and the generic background event. As motivated in Section 5.1.1, a neural network cut $\xi_{cut} = 0.4$ with a γ-efficiency of $\epsilon_\gamma = 0.83$ is chosen.
Fig. 5.12 shows the significance of the excess as a function of the Galactic latitude b. There is no evidence for an enhanced γ-flux from the direction of the disc. Tab. 5.2 gives the number of on-source and background events as a function of the definition of the Galactic disc size, together with the 90 % confidence level upper limit [126] on I_γ/I_{CR}. For $b_{plane} = 10°$, the Galactic disc definition adapted by CASA-MIA for their

Table 5.2: **Results of the search for enhanced emission from the Galactic disc. On-source events, background estimate, total number of events, and the 90 % c.l. upper limit on the ratio of γ-ray flux to hadronic cosmic ray flux are given for various definitions of the Galactic disc size b_{plane}. The γ-efficiency of the network separation is taken into account.**

b_{plane}	ON	OFF	excess u.l. (90 %)	total	I_γ/I_{CR} $[10^{-4}]$
5°	420 212	420 289	1072	1 544 290	8.4
10°	833 387	833 863	1312	3 072 748	5.1
15°	1 238 146	1 237 937	2052	4 584 201	5.4
20°	1 628 927	1 630 234	1549	6 063 627	3.1
25°	2 003 392	2 005 396	1517	7 490 220	2.4

limit, we obtain

$$\frac{I_\gamma}{I_{CR}} \leq 5.1 \cdot 10^{-4} \,. \tag{5.5}$$

In Fig. 5.12 (b), this upper limit and the Whipple and CASA-MIA limits are confronted with theoretical predictions of the diffuse γ-ray spectrum by Porter and Protheroe [137]. The propagation of electrons in the Galaxy is calculated using models of the Galactic

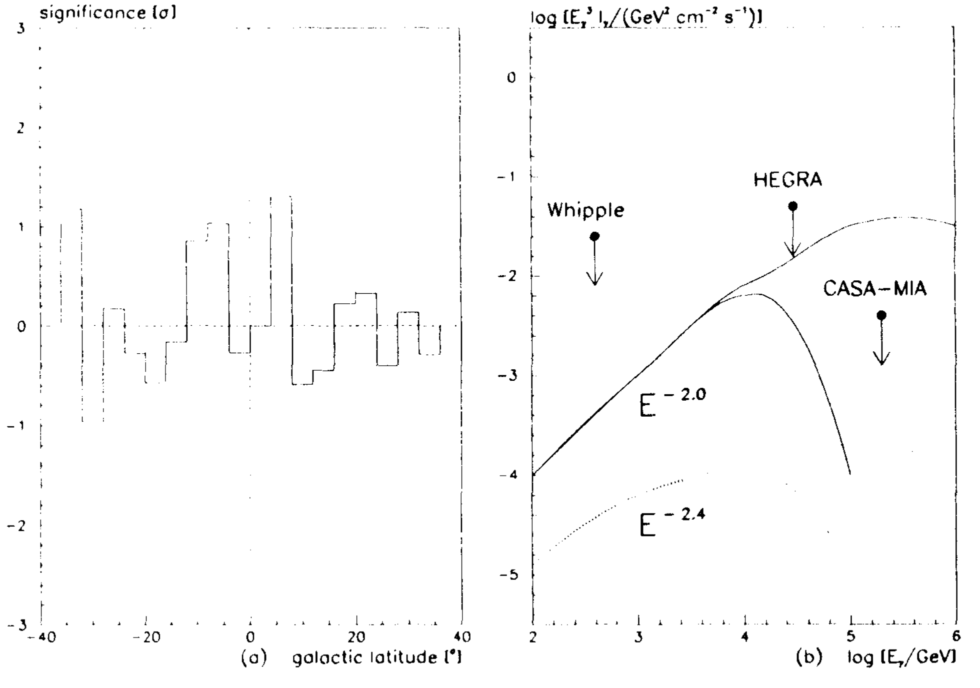

Figure 5.12: **(a) Significance for a γ-excess as a function of Galactic latitude. (b) Diffuse γ-ray spectra for two inverse-Compton injection spectra ($E^{-2.4}$ and E^{-2}) as calculated by Porter and Protheroe [137]. The lower branch of each curve includes a cutoff at 100 TeV. Upper limits from Whipple [136], CASA-MIA [103], and HEGRA (this analysis) are included.**

matter distribution, the magnetic fields and the interstellar radiation fields. Both inverse-Compton scattering and bremsstrahlung are taken into account. As a main result, Porter and Protheroe find that the contribution of inverse-Compton scattering dominates over neutral pion decay from the interaction of cosmic rays with matter (see e.g. [138, 139]). Inverse-Compton scattering as an additional component especially at higher energies may be an explanation for the flattening of the spectrum as observed by EGRET.

The model is calculated using different electron injection spectra. An improvement of the sensitivity of air shower arrays by at least one order of magnitude in the near future may place constraints on the inverse-Compton model and thus allow to actually estimate the injection spectrum.

Chapter 6

Blazar search

As the previous chapter has shown, γ-showers only make up a small part of the overall cosmic radiation. They are accompanied by an overwhelming amount of hadron showers without valid information about their origin. γ/hadron-separation considerably reduces this background and thus increases the signal-to-noise ratio, but nevertheless it remains substantially smaller than 1. Even a sophisticated estimation of the background with small statistical error and a subtraction of the expected background from the data (the ON-OFF-method) therefore may not give significant results on single sources.
Bearing in mind the disappointing results of previous searches with high statistics, all of them resulting in upper flux limits, only a marginal flux from a single source is expected even after γ/hadron separation. It is therefore crucial to increase the sensitivity of the detector array by additional methods.
In this chapter, the so-called stacking method for tagging weak sources is applied to the blazar sample compiled in Chapter 2 and additional source samples with different physical characteristics. After a general description of the stacking method, the neural network technique is applied to Geiger tower data taken in November and December 1994 and between February and April 1995.
We then extend the search to data taken with the HEGRA scintillator array between 1989 and 1992, i.e. in the first 3 years of stable running. No γ/hadron separation is possible for this data set, but the large statistics should compensate this.
In the last section, the results are summarized and compared to theoretical predictions.

6.1 The stacking method

6.1.1 General remarks

One of the main aims of the blazar compilation in Chapter 2 is the creation of a sample of likely candidates for TeV-emission, all of them physically equivalent. This allows to superimpose the sources of the sample to search for a *cumulative* signal from blazars as a class. This stacking method imitates a prolonged observation of a single source: provided the observation times are equal, the superposition of n objects corresponds to an n-fold observation of a single "generic" object having the properties of the sample.

This may increase the significance σ of a positive detection by a factor $\sqrt{n}$, as

$$\sigma \propto \sqrt{T_{obs}} \propto \sqrt{\sum_{i=1}^{n} T_{obs,i}}, \tag{6.1}$$

with $T_{obs,i}$ denoting the observation times of the single sources. The flux or flux limit derived from such a superposition cannot be assigned to a single source but reflects the average flux from the class of objects in the sample. The stacking method is a well-known tool in astronomy applied at almost every wavelength (see e.g. [140, 141] and references therein).

To avoid any bias, it is crucial that the source catalogues analyzed in this way meet two requirements: (1) the sources have to be *equivalent* and (2) the sample should be as *complete* as possible. The source sample and the selection criteria are described in detail in Chapter 2.

Obviously it is hardly possible to fulfill the second requirement. Future catalogue updates and redshift measurements hopefully will enlarge the sample, which at the time of data analysis comprises 12 sources.

Note that the superposition of sources at different distances does not a priori guarantee an increase in significance in cases where a large background contamination is expected. Assuming we deal with "standard candles" and the flux decreases with the distance squared, the source with the smallest z will dominate the sample. If the sources are distributed homogeneously in z, the nearest source is in fact the only one contributing, and a superposition of sources farther away will decrease the significance.

Nevertheless, in the case of the blazar sample, trying a superposition seems promising for several reasons: first, the sources are not homogeneously distributed in z but form two clusters at $z \simeq 0.03$ and $z \simeq 0.055$. In addition, blazars are known to be rapidly and violently variable even at the highest observed energies [142]. We therefore cannot expect them to be "standard candles", especially as typically the more distant sources have a higher luminosity (else they would not have been detected with flux limited detectors). The main dependence on distance will arise from the exponential cutoff by infrared background absorption, and where exactly this cutoff takes effect is unknown. Superimposing means to average both in flux and in time, and this may be one of the main advantages of stacking at TeV energies.

It is self-evident that source stacking must in the first place be regarded as a makeshift solution. When analyzing small data samples, e.g. the Geiger tower data suited for γ/hadron separation, it is a powerful tool for improving the sensitivity, but when analyzing larger data sets (as in the second part of this chapter), we expect a different behavior: On a long-term basis, individual sources will dominate, whereas others will show no significant flux on all time scales.

6.1.2 The source samples

Nearby blazars

The sources of the blazar sample are summarized in Tab. 2.1. Fig. 6.1 shows their position in equatorial coordinates together with the daily observation time. The time

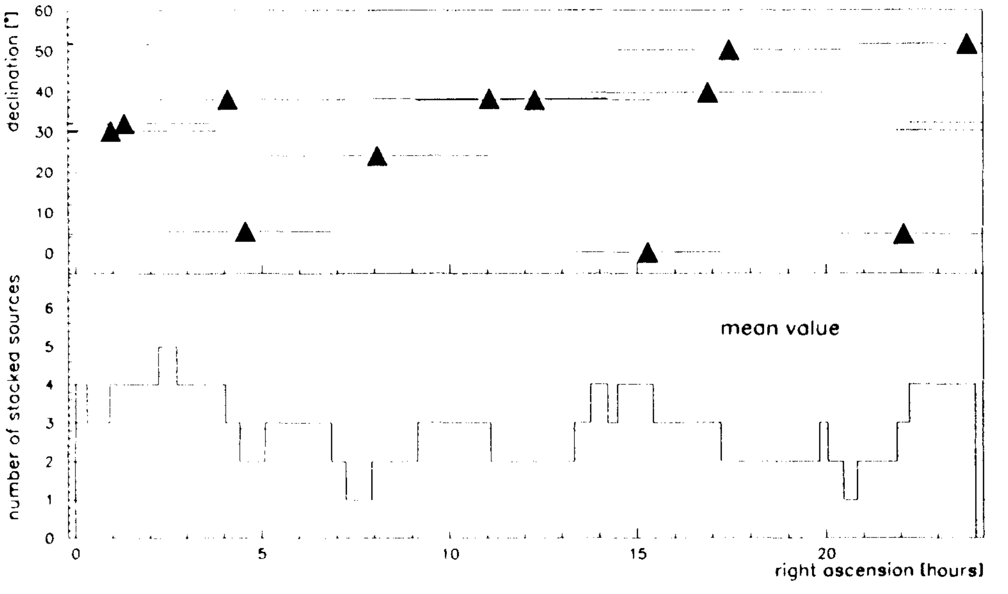

Figure 6.1: **Stacking of the 12 blazars: the upper plot shows the source positions in equatorial coordinates with the bars indicating the daily on-time for HEGRA (zenith angle $\theta \leq 40°$), the lower plot shows the total number of stacked sources as a function of right ascension together with the mean value (dotted line).**

of visibility with zenith angle below 40° strongly depends on the declination of the source: it ranges from 6 hours per day for sources at declinations which approximately equal the HEGRA latitude to 4 hours per day for sources culminating at high zenith angles, like 1514+004. The lower plot of Fig. 6.1 shows the total number of stacked sources as a function of right ascension and thus for 24 hours of observation. On the average, $\simeq 3$ sources are permanently stacked.

Additional source samples

In order to check whether the main selection criteria for the source sample, the blazar classification and the small distance, are indeed crucial for detection with HEGRA, the search is extended to three additional samples with partly different properties, called *anti-samples* in the subsequent analysis:

(i) 19 BL Lac objects with $0.069 \leq z \leq 0.203$ selected from the catalogue of Véron-Cetty & Véron (1995) [18].

(ii) 31 flat-spectrum radio sources with $0.1 \leq z \leq 1.04$ selected from Kühr et al.

(1981) [62] with $5° \leq \delta \leq 51°$.

(iii) 49 nearby ($z \leq 0.1$) steep-spectrum radio sources selected from Kühr et al. (1981) [62].

The sources are listed in Tab. 6.1 - Tab. 6.3 together with their redshifts.

Table 6.1: **19 BL Lac objects with $0.069 \leq z \leq 0.203$ from the catalogue of Véron-Cetty & Véron [18].**

source	z	source	z	source	z
2200+420	0.069	1ES 1212+078	0.136	1ES 0927+500	0.188
1404+286	0.077	1ES 0229+200	0.140	MS 03170+1834	0.190
1ES 1741+196	0.083	1ES 1255+244	0.141	2254+074	0.190
1219+285	0.102	1ES 1239+069	0.150	1402+042	0.200
EXO 1118.0+4228	0.124	1418+546	0.152	1ES 0446+449	0.203
1ES 0145+138	0.125	1ES 1440+122	0.162		
1426+428	0.129	0829+046	0.180		

Table 6.2: **31 flat-spectrum radio sources ($0.1 \leq z \leq 1.04$) selected from Kühr et al. [62].**

source	z	source	z	source	z
0235+164	0.940	1328+307	0.849	2201+315	0.297
0428+205	0.219	1345+123	0.122	2209+080	0.484
0738+313	0.631	1354+195	0.720	2209+236	
0748+126	0.889	1604+159	0.357	2230+114	1.037
0812+367	1.025	1641+399	0.593	2234+282	0.795
0906+430	0.670	1656+053	0.879	2247+140	0.237
0923+392	0.699	1725+044	0.293	2251+158	0.859
0953+254	0.712	1800+440	0.663	2344+092	0.677
1150+497	0.334	1828+487	0.692	2352+493	0.237
1252+119	0.871	1830+285	0.594		
1308+326	0.996	2145+067	0.990		

6.2 Pre-analysis: cuts and methods

The following analysis is based on 48 180 324 events taken with the HEGRA array in two periods of stable Geiger tower performance between October and December 1994 and between February and April 1995.
As described in Chapter 3, the core position and the incident angles are determined by making use of the scintillator information. In order to have stable running conditions, fulfillment of the scintillator trigger condition is therefore also required in runs where the AIROBICC matrix contributes to the trigger.
In addition, several cuts are applied to the data to achieve a high quality of the analyzed data sample. They can roughly be divided into three categories:

Table 6.3: **49 steep-spectrum radio sources ($z \leq 0.1$) selected from Kühr et al. [62]. The 3C number is given if available (else 4C).**

source		z	source		z
3C 31	(0104+32)	0.017	3C 277.3	(1251+27)	0.086
3C 33	(0106+13)	0.059	4C 29.47	(1316+29)	0.073
3C 35	(0109+49)	0.067	3C 285	(1319+42)	0.080
4C 18.06	(0124+18)	0.044	4C 36.24	(1322+36)	0.018
4C 35.03	(0206+35)	0.037	4C 31.43	(1350+31)	0.045
3C 66	(0220+42)	0.021	3C 296	(1414+11)	0.024
3C 75	(0255+05)	0.023		(1422+26)	0.037
3C 76.1	(0300+16)	0.032	3C 306	(1452+16)	0.042
3C 83.1	(0315+41)	0.025	3C 310	(1502+26)	0.054
3C 84	(0316+41)	0.018	3C 317	(1514+07)	0.035
3C 98	(0356+10)	0.030	3C 321	(1529+24)	0.096
3C 109	(0410+11)	0.033	3C 326	(1550+20)	0.089
4C 56.16	(0745+56)	0.036	4C 35.40	(1615+35)	0.029
3C 189	(0755+37)	0.043	3C 338	(1626+39)	0.030
4C 32.25	(0828+32)	0.051		(1743+55)	0.031
4C 31.32	(0844+31)	0.067	3C 386	(1836+17)	0.017
3C 227	(0945+07)	0.085	3C 388	(1842+45)	0.092
3C 236	(1003+35)	0.099	3C 402	(1940+50)	0.025
	(1040+31)	0.036	3C 442	(2212+13)	0.027
4C 29.41	(1113+29)	0.048	3C 449	(2229+39)	0.018
3C 264	(1142+19)	0.021	3C 452	(2243+39)	0.082
4C 22.33	(1204+22)	0.065	4C 36.47	(2244+36)	0.081
3C 270	(1216+06)	0.007	4C 11.71	(2247+11)	0.026
3C 272.1	(1222+13)	0.003	3C 465	(2335+26)	0.030
3C 274	(1228+12)	0.004			

- cuts increasing the data quality,
- cuts necessary to obtain a stable γ/hadron separation, and
- physically motivated cuts to increase the sensitivity of the γ-source search.

The quality cuts include a cut on the zenith angle of the incident shower ($\theta \leq 40°$) and a border cut restricting the core position to an area of $150 \times 160\,\mathrm{m}^2$ around the center of the array.

The accepted zenith angle range is larger than in the network training where $\theta \leq 30°$ is chosen. The 40°-cut for the experimental data is sensible to achieve a smooth angular distribution even for those sources with declination above 50° and below 6°. The network efficiency only slightly decreases for zenith angles up to 40°.

The border cut is further illustrated in Fig. 6.14, where the core position of accepted events is shown together with the position of the scintillator huts. In addition to improving the angular resolution, this cut is necessary to increase the γ/hadron separation quality, as for showers with core far outside the Geiger sub-array, the towers do not carry enough information for an efficient separation. For the same reason, events with a shower size $N_e \leq 10\,000$ are discarded (see Fig. 5.7), thus the energy threshold for γ-showers is about 50 TeV. Apart from guaranteeing a stable separation power, this

cut also improves the angular resolution, as $\sigma_{63\%} \propto 1/\sqrt{N_e}$ (see Eq. 3.6).
Before neural network processing, noisy Geiger tubes are excluded as they otherwise considerably deteriorate the network performance. An additional cut has to be applied to account for the fact that a γ/hadron separation using the Geiger towers cannot be achieved in events where less than 6 towers record any hit information at all. As shown in Chapter 5, this condition does not increase the threshold energy significantly, as it is fulfilled for 98.6 % of the events triggered by the scintillator array.
The final cut is motivated by physics. As described above, no γ-showers are expected above 100 TeV due to absorption in the cosmic microwave background. We therefore discard events with a shower size $N_e \geq 30\,000$. Due to the rather loose correlation between the shower size and the primary energy, this is a rather dangerous cut, and in order to assess its influence, the analysis is also performed without it. Nevertheless, if a γ-like excess is actually observed, its significance inevitably *must* increase when large shower sizes are excluded. The analysis of this cut may therefore serve as an important check for the reliability of any signal seen in the data.

After all cuts, the data sample is reduced to 12 529 705 events.
The runs used for this analysis are selected for their rather high quality Geiger performance. Runs with deteriorated neural network separation due to bad tower performance are consequently excluded from the data sample. This procedure guarantees a quality factor which is stable within 20% for all accepted runs. Nevertheless, due to at least two missing towers and various inefficient layers, the expected quality factor Q is only about 2, depending on the cut value.

6.2.1 Background estimation and significance calculation

Several methods of estimating the hadronic background are applied in air shower physics. The easiest method is to simply extrapolate the number of entries in neighboring bins to the source bin by e.g. averaging between 2° and 5° angular distance from the source position. There are several major drawbacks from this method, as it does not take into account that the acceptance of the detector array is not uniform in horizontal coordinates θ and ϕ (and thus not uniform in right ascension α and declination δ either). Fig. 6.2 shows the total number of showers both in horizontal coordinates θ and ϕ and in equatorial coordinates α and δ. The non-uniformity in right ascension partly reflects the interruptions in observation time of the Geiger sub-array due to detector maintenance and deteriorated performance. Any procedure for background estimation has to take into account the dependence of the detector efficiency and the γ/hadron separation on local coordinates. A method which automatically removes such systematics has been proposed by Alexandreas et al. [143]: the number of expected background events in the source bin is determined by connecting the actual event time with incident angles taken at random from the (θ, ϕ)-distribution of the data. In the following analysis, typically 50 000 events from the same (or a neighboring) run are stored to create a background pool. For each event, a number of n background events are taken from this pool, and right ascension and declination are calculated using the horizontal coordinates of the pool event and the actual event time. For both original

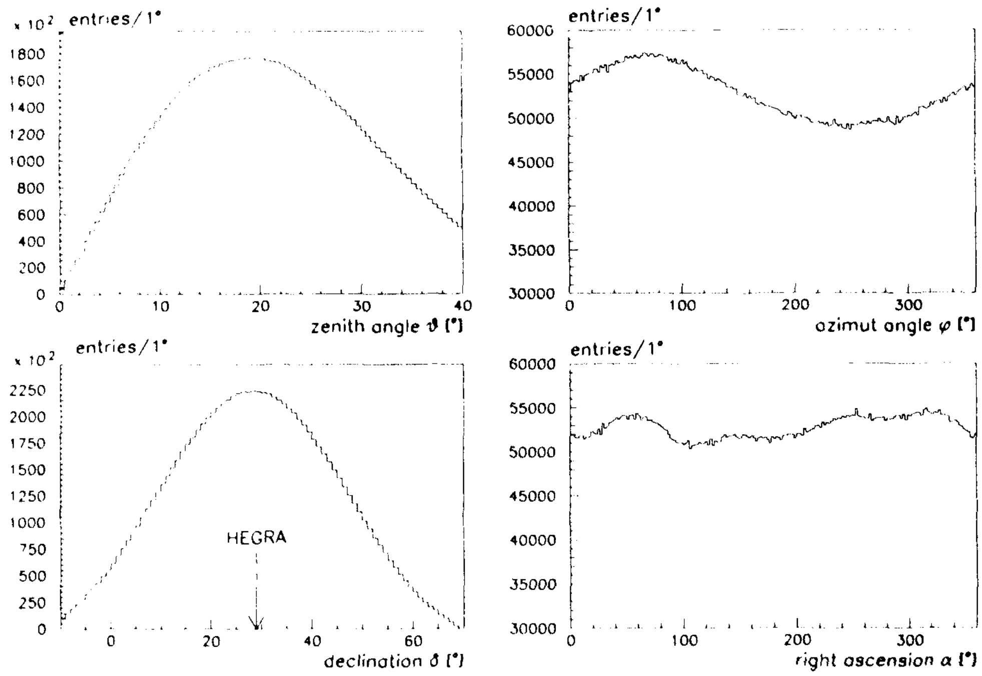

Figure 6.2: **Total number of showers in horizontal coordinates θ and ϕ and equatorial coordinates α and δ. The latitude of the HEGRA array (28.8° N) is indicated.**

event and background events, the same cuts (neural network output, minimum number of towers, etc.) are applied. As a major advantage this method guarantees that the (θ, ϕ)- distribution for original data and background are identical, so it automatically accounts for systematics in local detector coordinates, e. g. the dependence of reconstruction and separation on the zenith angle.
The calculation of the significance of an excess or deficit in the source bin depends on the number of random events n used for the background estimation. Choosing $n = 10$ or $n = 20$, as in the following analyses, means that the background estimate N_{off} has a smaller statistical error than the number of source bin events N_{on}. This has to be taken into account when calculating significances. The method applied here has been proposed by Li and Ma [144] and evaluates the significance of an observation (N_{on}, N_{off}) by a maximum likelihood ratio test. With $\alpha = 1/n$, the significance of the excess is given by

$$S = \sqrt{2}\left\{N_{on}\ln\left[\frac{1+\alpha}{\alpha}\left(\frac{N_{on}}{N_{on}+N_{off}}\right)\right] + N_{off}\ln\left[(1+\alpha)\left(\frac{N_{off}}{N_{on}+N_{off}}\right)\right]\right\}^{0.5}. \tag{6.2}$$

The formula gives reliable results compatible with Gaussian probabilities at least for $N_{on}, N_{off} \geq 10$.

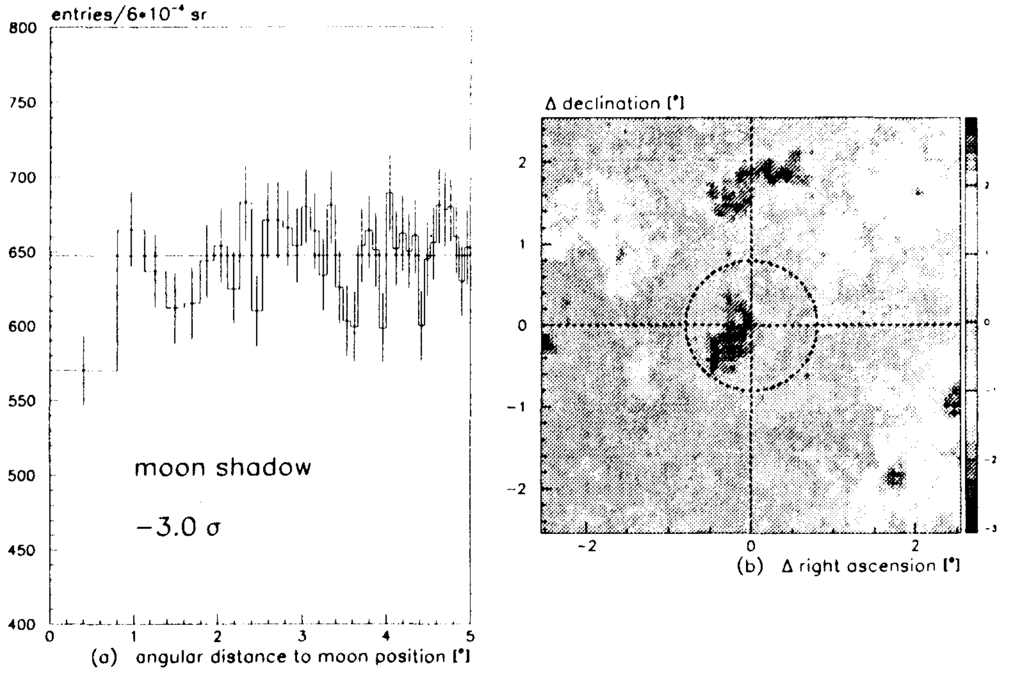

Figure 6.3: **Moon shadow: (a) number of showers as a function of the angular distance from the moon position. (b) Significance of the moon shadow as a function of the position of the source bin center. In both plots, a source bin size of** $0.8°$ **is chosen.**

6.2.2 Angular resolution and moon shadow

The angular resolution of the extended HEGRA scintillator array has been determined to

$$\sigma_{63\%} = \frac{(104.5 \pm 0.4)°}{\sqrt{N_e}} \tag{6.3}$$

(see Eq. 3.6) with respect to the total number of electrons N_e. This implies an angular resolution of $\sigma_{63\%} = 1.0°$, containing 63% of the source events. As the angular resolution for γ-showers is $\simeq 10\%$ better than for hadron showers, the following analysis is based on an estimated resolution of $\sigma_{63\%} = 0.9°$. If the source is point-like, the dispersion of the signal is solely a result of the finite angular resolution of the detector and may therefore be described by a Gaussian. In this case, the optimal source bin size, i. e. the source bin size which maximizes signal-to-noise, is $\sigma_{72\%}$ (see e. g. [143]). We thus choose $\sigma_{72\%} = 1.0°$, so the corresponding solid angle is

$$\Omega_{\sigma_{72\%}} = 2\pi(1 - \cos\sigma_{72\%}) = 1.0 \cdot 10^{-3}\text{sr}. \tag{6.4}$$

If the γ-ray spectrum of point sources is flatter than the overall cosmic ray flux, the amount of higher energy γ-events in the data is enhanced and the optimal source bin size is in fact smaller than the value derived above. As the spectral index is unknown

in the energy region relevant for this analysis and probably also depends on the source, it is not possible to include this effect.
For all runs, the stability of the scintillator data reconstruction is monitored by comparing the shower direction to the direction of tracks detected by the Geiger tower array (see Chapter 5). Whereas this procedure allows a pointing check for each individual run, an independent test is applied by searching for a deficit of showers from the direction of the moon (see e. g. the results of the Tibet group [145]). With a diameter of $\simeq 0.5°$, the moon is a beam dump for cosmic rays and the moon shadow should be visible in the data. The method has been applied as a test for the θ, ϕ-reconstruction of the HEGRA array, and within 5 months of data taking, a deficit at the $5.5\,\sigma$ level has been found [91].
To check the moon shadow for the 12 529 705 events of this analysis after all cuts, a source bin radius of 0.8° (corresponding to [91]) has been chosen. Fig. 6.3 shows the number of events as a function of the angular distance from the moon position. Here and in the following radial plots, the first bin is called source bin and contains the source in its center, and the bin size is chosen to obtain equal solid angles for each radial bin.
Fig. 6.3 shows a deficit of showers from the moon direction of $3.0\,\sigma$. Within the statistical errors, this is in correspondence with expectation: the moon with a radius of 0.25° covers a fraction of

$$\frac{1-\cos 0.25°}{1-\cos 0.8°} \simeq 0.1 \tag{6.5}$$

of the 0.8°-source bin area. Instead of 647 ± 8 expected events, we actually observe 570 ± 24 events, thus indeed a fraction of $\simeq 0.12$ of the events are missing.
To estimate the pointing accuracy of the scintillator reconstruction, we also plot the moon position two-dimensionally in equatorial coordinates. For every bin in Fig. 6.3 (b), the significance of the deficit is calculated for the area of the circle with the bin center as central point by counting on- and off-source events as described in Section 6.2.1. Note that in this "sliding bin" method, neighboring bins are highly correlated. The two-dimensional significance distribution indicates that the moon shadow is slightly shifted by $\simeq 0.3°$, mainly in right ascension.
As the data sample is rather small, Fig. 6.3 (b) does not allow to claim a pointing error unambiguously and to develop methods of correcting it, but the source bin size of the following analysis is rather large, thus a shift of this order of magnitude does not seriously affect the results. Nevertheless, we have to check the dependence of the source significances on the source bin size, as any pointing error will inevitably shift the maximum of the significance to higher source bin radii. A similar pointing error of 0.2° to 0.3° has been found in earlier analyses of HEGRA data [74].

6.2.3 Energy threshold for the generic sources

In high energy astrophysics, integral fluxes or upper limits on fluxes from point sources $\Phi(E > E_{thresh,\gamma})$ are commonly calculated by comparing the number of excess events

$$N_{excess} = \frac{N_{on} - \alpha N_{off}}{\epsilon_\gamma} , \tag{6.6}$$

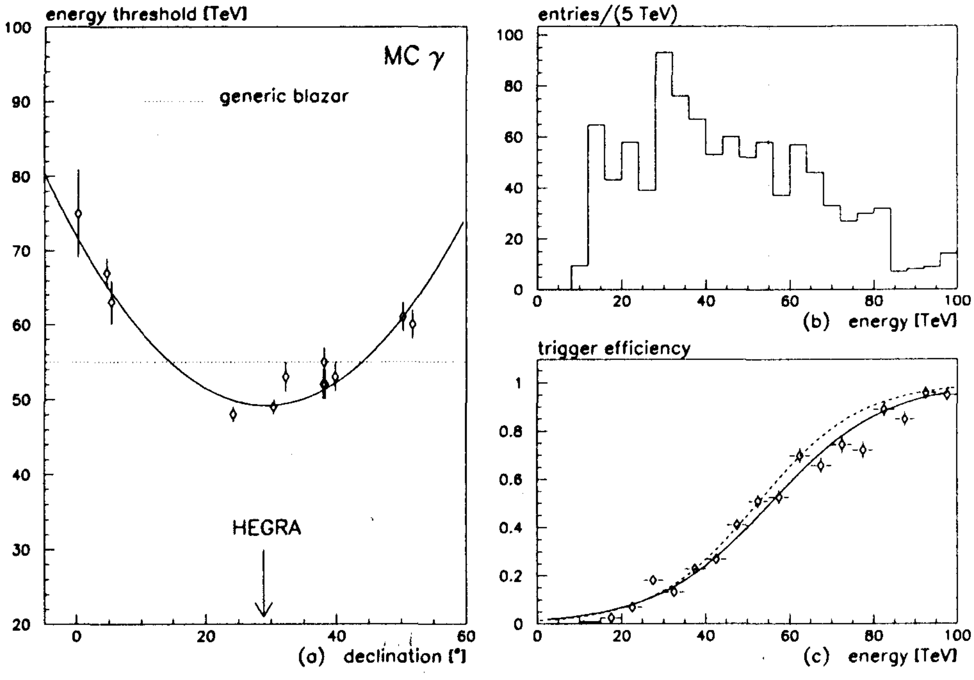

Figure 6.4: **(a) γ-threshold energy as a function of the source declination for the blazars. (b) Expected energy distribution for the generic blazar. (c) Trigger efficiency of the generic blazar with and without the neural network γ-cut $\xi \leq 0.4$ (solid resp. dashed line).**

resp. the upper limit on N_{excess}, to the total number of events N_{sb} in the source bin. As N_{sb} is produced by the total cosmic ray flux above the threshold energy of the detector and N_{excess} is produced by the γ-flux,

$$\frac{\Phi(E > E_{thresh,\gamma})}{\Phi_{CR}(E > E_{eff,CR})} = \frac{N_{excess}}{N_{sb}} \tag{6.7}$$

holds and allows a flux calculation avoiding the determination of the effective area of the detector array which usually does not equal the geometric size.
The integral cosmic ray flux is taken as calculated in [80] on the basis of all available experimental data,

$$\Phi_{CR}(E > E_{eff,CR}) = \Omega \cdot (1.52 \pm 0.01) \cdot 10^{-5} E_{\mathrm{TeV}}^{-1.67 \pm 0.02}\ \mathrm{cm}^{-2}\mathrm{s}^{-1}\mathrm{sr}^{-1}, \tag{6.8}$$

with Ω denoting the solid angle of the source bin.
Application of Eq. 6.7 requires the knowledge of the threshold energy E_{thresh} for γ-showers. As shown in Section 5.1.2, E_{thresh} strongly depends on the zenith angle θ, thus the θ-distributions of the sources differ due to the different declinations δ. In order to derive E_{thresh} both for the individual blazars and for the generic sources which

comprise objects with a large variety in declination, we have to adopt the θ-distribution of the MC γ-showers to the θ-distribution of each source.
In the first step, we simulate the expected θ-distribution of each source by calculating the zenith angles during 24 hours in right ascension, assuming a constant, i. e. time independent flux from the sources. The resulting zenith angle distribution of each source is used to create MC γ-shower samples with the same θ- distribution. As usual, core position and energy (10 to 500 TeV, spectral index 2.75) are taken at random to imitate the experimental data. The uncertainty in the spectral index is included in the

Table 6.4: γ- **and proton threshold energies ($E_{thresh,\gamma}$ resp. $E_{thresh,p}$) of the generic sources as derived from MC simulations.**

source	$E_{thresh,\gamma}$ [TeV]	$E_{thresh,p}$ [TeV]
blazar	55	65
BL Lac	56	66
flat-spectrum	54	65
steep-spectrum	55	65

systematic error on E_{thresh}.
We now dispose of the γ-shower distribution expected from the direction of each source, thus applying the same cuts to the MC data as to the experimental data enables us to determine the threshold energy of the individual blazars and the generic sources. In addition to the cut on the shower size and the minimum number of scintillator huts and Geiger towers, we include the neural network γ/hadron separation cut $\xi \leq 0.4$, as we expect it to slightly increase the threshold energy: the separation is more efficient at higher energies and may thus enhance the fraction of showers above 50 TeV.
Following the definition in Section 5.1.2, we derive threshold energies for the generic sources as given in Tab. 6.4. The thresholds for the individual blazars are listed in Tab. 6.6. Fig. 6.4 (a) shows E_{thresh} for the 12 nearby blazars as dots with error bars from the fitting of the sigmoid function to the trigger efficiency (see Fig. 6.4 (c)). E_{thresh} ranges from below 50 TeV for sources culminating near $\theta = 0°$ to more than 70 TeV for 1514+004 with $\delta \simeq 0°$. As expected, E_{thresh} has a minimum for sources with $\delta \simeq 29°$, the latitude of HEGRA. The dotted line indicates the threshold energy of the generic blazar.
Apart from the advantage of automatically including effects from the γ/hadron separation and the steep energy spectrum of the sources, this MC method allows to estimate the expected energy and N_e-spectrum of the γ-showers passing the trigger and the separation. As shown in Fig. 6.4 (b), 69 % of the showers have energies *below* 55 TeV, and the "most likely" value of the γ-shower energy is between 30 and 35 TeV. We have to keep this in mind when interpreting flux values.
Fig. 6.4 (c) shows that the effect of the γ/hadron separation on E_{thresh} is rather marginal: it increases the threshold energy from 52 TeV (dashed line) to 55 TeV (solid line). This is well within the rather large systematic error of 10 TeV which is again mainly a consequence of the unknown spectral index of γ-rays. A flatter spectrum will shift the threshold energy to higher values.

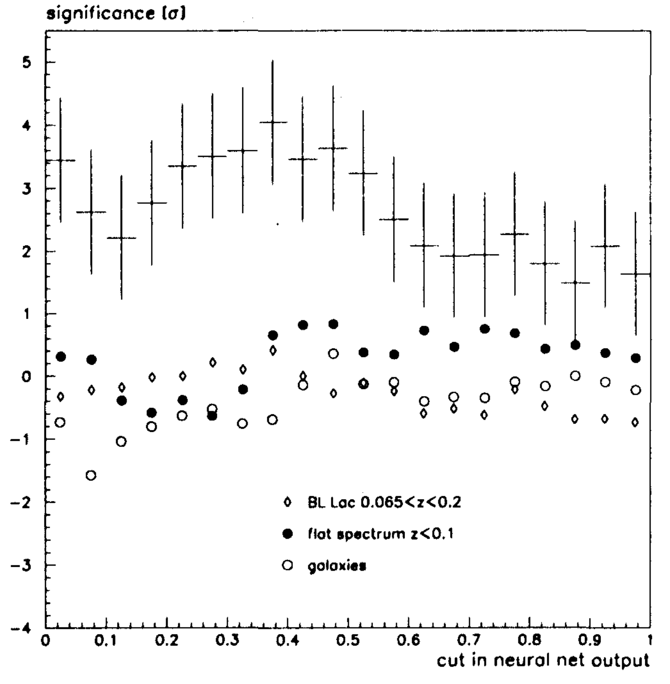

Figure 6.5: **Significance of the excess as a function of the cut in the net output for the blazar superposition and the 3 anti-samples.**

6.3 Results of the Geiger data analysis

Following Chapter 5.1.1, a network cut at $\xi_{cut} = 0.4$ is the optimal choice for data with the quality of the sample used in this analysis. In this region, statistical and systematic errors in the MC predictions are small due to the large γ-shower efficiency of more than 0.8.

Before applying this cut to experimental data, we first study the significance as a function of ξ_{cut} for the four generic sources described in Section 6.1.2. As shown in Fig. 6.5,

- there is no significant cumulative excess from the 3 anti-samples *for any network cut.*

In a striking contrast to this,

- the generic nearby blazar shows an excess $\geq 3\,\sigma$ for any $\xi_{cut} \leq 0.5$, i.e. in the region where γ-showers are expected.

In correspondence with this, a comparison of the network output distribution for source bin events and background estimate shows no significant differences for the 3 anti-samples, whereas both distributions considerably differ for the blazar superposition.

This is illustrated in Fig. 6.6, where (a) shows the network output distribution for the source bin events (solid line) and the background estimate (dotted line). Both distributions significantly differ below $\xi = 0.4$. In Fig. 6.6 (b), the significance of the difference is shown for each bin of (a). The main deviation of almost $3.5\,\sigma$ is below 0.05, i. e. in the region where the major part of the γ-showers are expected to pile up according to network training and testing. There is also a considerable amount of excess events with $0.05 \leq \xi \leq 0.4$ indicating both the tail of the γ-shower distribution and the effect which runs of deteriorated quality have on the network output. The break-in of the significance at network cuts $\xi_{cut} \simeq 0.2$ in Figs. 6.5 and 6.6 (b) reflects the composition of the data sample: the peak at low cut values is dominated by high quality runs, the plateau above $\simeq 0.2$ by lower quality runs.
In order to check whether the expected efficiencies for γ-detection and hadron rejection are actually achieved, we *treat the excess as a signal* and calculate the efficiencies as a function of ξ_{cut}. As shown in Fig. 6.6 (c)-(d), results are compatible with MC expectations. Note that for all comparisons between experimental data and MC, the MC has been adjusted to the deteriorated performance of the Geiger tower sub-array.

Table 6.5: **Results for the different source samples ($n = 10$). Φ is the upper limit on the integral flux above E_{thresh}.**

	no separation			separation			$\Phi^{90\%}_{u.l.}(> E_{thresh})$
source	N_{on}	$10 \cdot N_{off}$	sign. [σ]	N_{on}	$10 \cdot N_{off}$	sign. [σ]	[cm^{-2}s^{-1}]
$10\,000 \leq N_e \leq 30\,000$							
BL Lac	38 895	389 997	-0.5	9 911	98 688	0.4	
flat	69 456	694 419	0.2	17 703	176 135	0.7	
steep	115 002	1 150 932	0.0	28 428	285 494	-0.7	
$10\,000 \leq N_e$							
BL Lac	55 017	554 165	-1.7	13 944	139 232	0.2	8.6 10^{-14}
flat	98 244	984 243	-0.5	24 938	248 635	0.4	7.2 10^{-14}
steep	162 537	1 626 206	-0.1	40 262	402 416	0.3	4.8 10^{-14}

Flux limits and significances

For the further analysis of the source sample, we apply a network cut at $\xi_{cut} = 0.4$, regarding all showers with $\xi \leq 0.4$ as γ-induced.
Fig. 6.7 shows the number of entries as a function of the angular distance from the source position for the three anti-samples together with the background estimate. For these generic sources, 90% confidence level upper limits on the flux are calculated using the method of Helene [126]:

$$\Phi^{BLLac}_{90\%}(E \geq 56\text{TeV}) = 8.6 \cdot 10^{-14}\text{cm}^{-2}\text{s}^{-1} \quad (6.9)$$

$$\Phi^{flat-sp.}_{90\%}(E \geq 54\text{TeV}) = 7.2 \cdot 10^{-14}\text{cm}^{-2}\text{s}^{-1} \quad (6.10)$$

$$\Phi^{steep-sp.}_{90\%}(E \geq 55\text{TeV}) = 4.8 \cdot 10^{-14}\text{cm}^{-2}\text{s}^{-1}. \quad (6.11)$$

As these upper limits refer to the *integral* flux above 50 TeV, they are calculated using the event numbers without restrictions on the upper shower size, thus without the cut

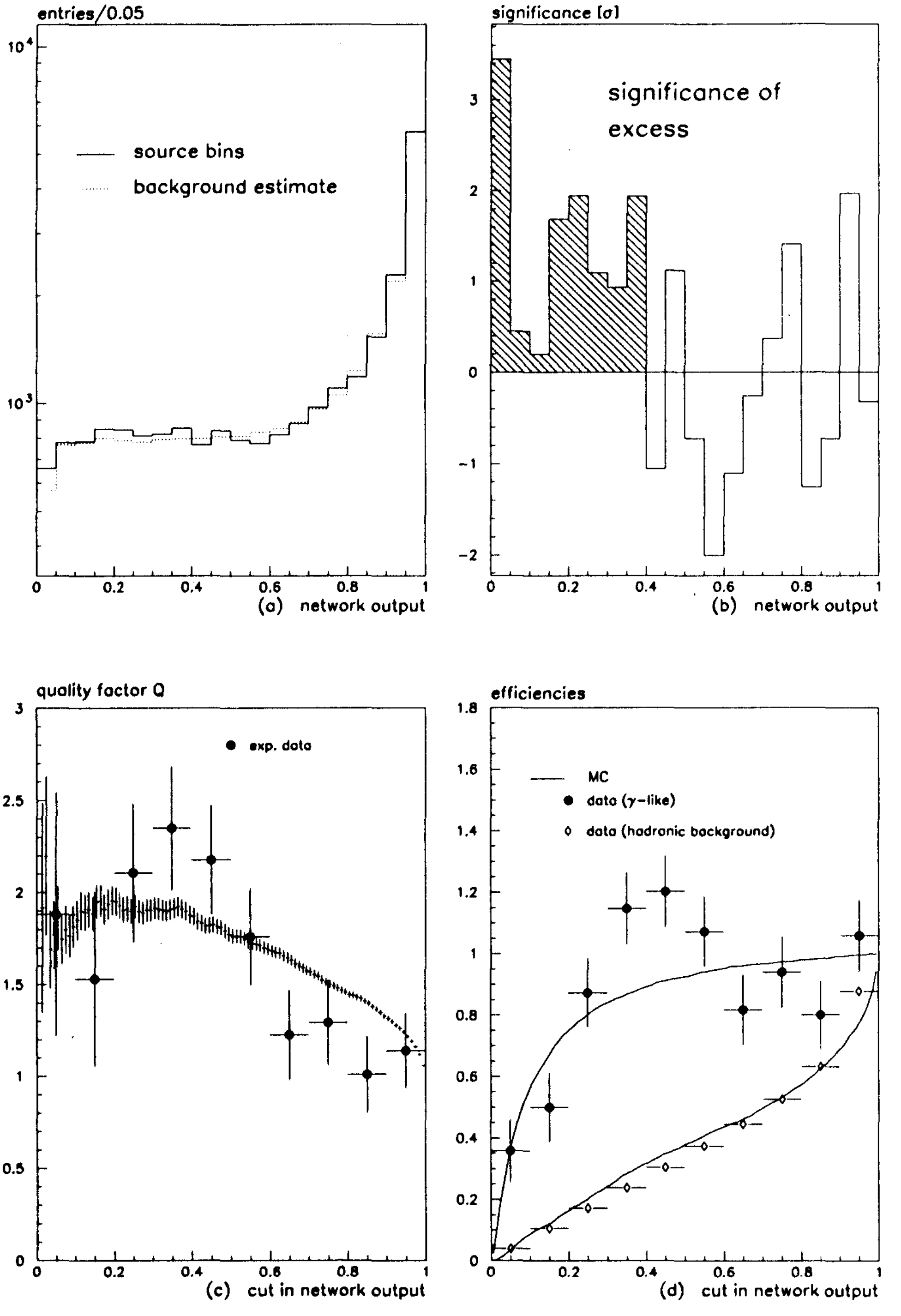

Figure 6.6: **(a) Network output distribution for the source events and the background estimate (dotted line). (b) Difference between source events and background distribution in σ as a function of the net output. (c) Quality factor Q and (d) γ- and hadron-efficiency as a function of the cut in the net output for MC and experimental data.**

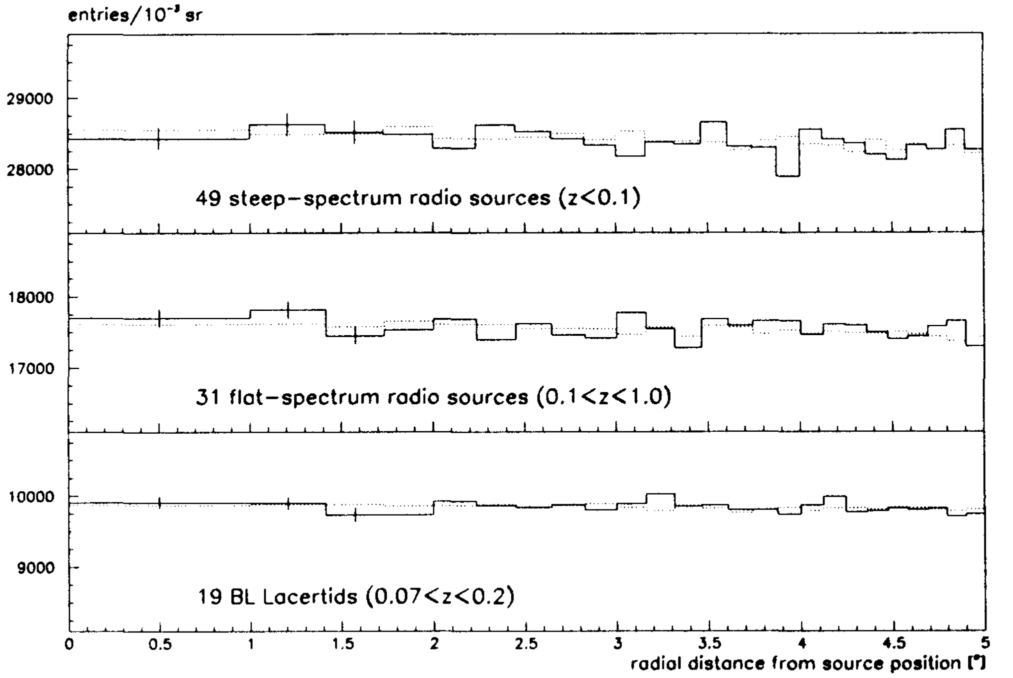

Figure 6.7: **Results for the samples with 19 BL Lac objects, 31 flat-spectrum and 49 steep-spectrum radio galaxies.**

$N_e \leq 30\,000$.

Fig. 6.8 shows the cumulative excess from the superposition of the 12 nearby blazars as a function of the angular distance from the source position with and without γ/hadron separation. The results are summarized in Tab. 6.5.

The separation reduces the number of hadron showers in the source bin from 26 288 to 6 884 in good accordance with the hadron rejection derived from MC calculations.

The excess of the blazar sample is regularly accumulated over the whole period and not a result of short periods of high rates. As shown in Tab. 6.6 and Fig. 6.10, which summarize the blazar results both for the individual sources and the superposition, the excess is not dominated by single sources. There is in fact no object with a significance $\geq 2.2\,\sigma$ in all 4 samples. This is in accordance with expectation, as the Geiger tower data analysis covers only a short period of data taking.

To verify that the excess of the blazar sample is a true *cumulative* excess, the significances of the single sources are histogrammed in Fig. 6.9 both for the 99 galaxies, BL Lacertids, and flat-spectrum radio sources forming the 3 anti-samples and the 12 nearby blazars. As a striking result, the significance distribution for the 12 blazars is considerably shifted to a positive mean value 1.4 ± 0.4 (variance 0.9 ± 0.6), whereas the anti-sample distribution has a mean of -0.1 ± 0.2 (variance 1.4 ± 0.2).

To sum up, the neural network analysis based on the Geiger tower data strongly indi-

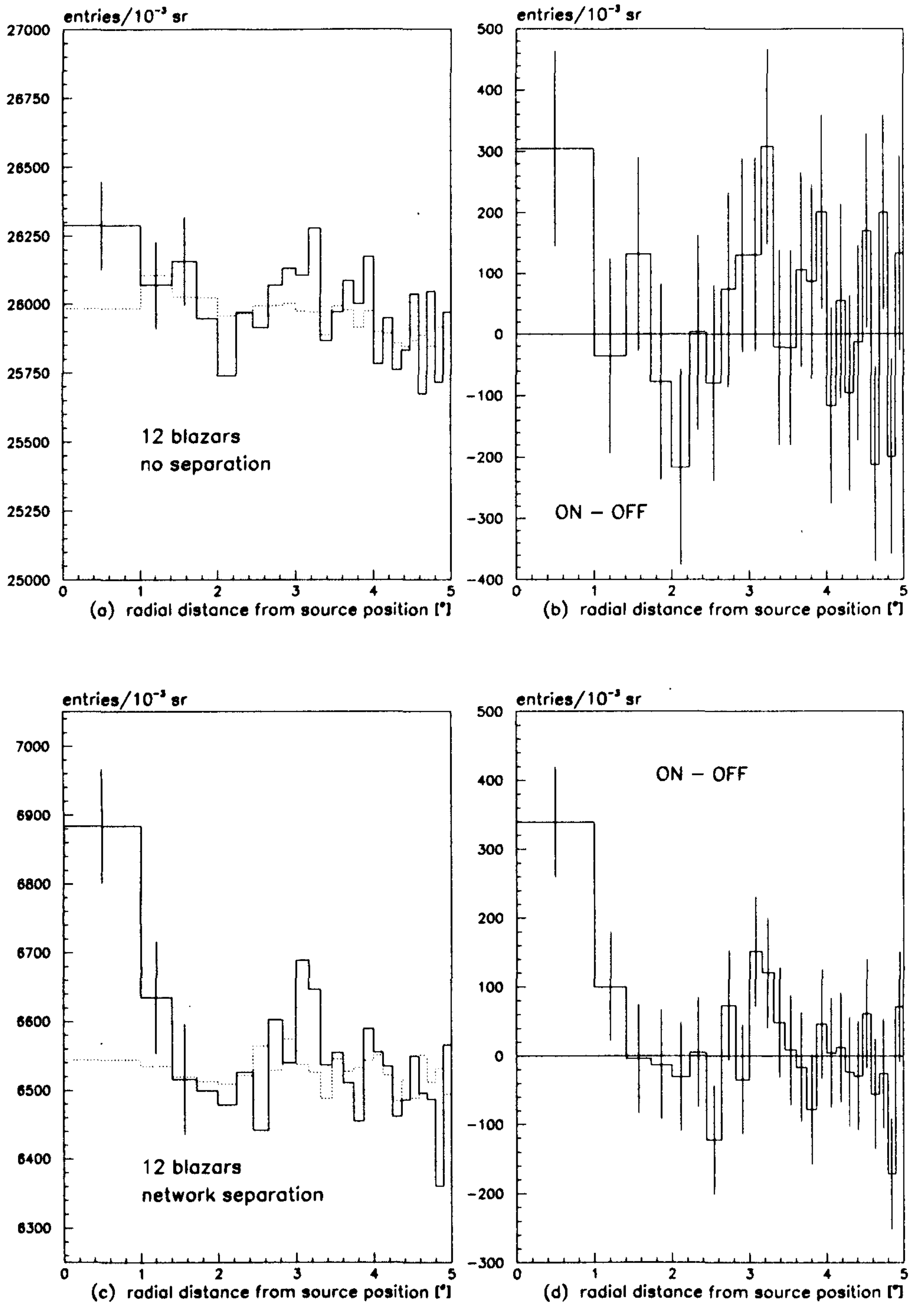

Figure 6.8: **Superposition of the 12 nearby blazars with and without γ/hadron-separation: (a) shows the number of events as a function of the angular distance from the source position. The dotted line is the background estimate, which is subtracted from the event distribution in (b). In (c) and (d), γ/hadron-separation is applied.**

Table 6.6: **Results for the blazar sample ($n = 20$).**

source	$E_{thresh,\gamma}$ [TeV]	time [s]	no separation N_{on}	$20 \cdot N_{off}$	sign. [σ]	separation N_{on}	$20 \cdot N_{off}$	sign. [σ]
$10\,000 \leq N_e \leq 30\,000$								
0055+300	49	1 154 836	2804	55826	0.2	714	13637	1.2
2201+044	67	838 931	1083	20784	1.3	343	6229	1.7
1101+384	52	1 186 793	2788	56931	-1.1	710	13291	1.7
0430+052	63	894 245	1082	21193	0.7	317	6214	0.3
1652+398	53	1 177 671	2951	57990	0.9	721	14389	0.0
2344+513	60	1 091 607	1691	32811	1.2	489	9527	0.6
1514+004	75	741 659	722	14183	0.5	248	4514	1.4
0402+379	55	1 206 493	2769	55163	0.2	711	13288	1.7
1727+502	61	1 122 608	2039	39994	0.9	588	11103	1.3
0116+319	53	1 171 718	2766	54970	0.3	705	12998	2.1
0802+243	48	1 129 836	2631	52313	0.3	635	12176	1.0
1214+381	52	1 198 954	2962	57512	1.6	703	13528	1.0
Σ blazars	55	12 915 351	26 288	519 670	1.8	6 884	130 894	4.1
$10\,000 \leq N_e$								
0055+300			3913	78097	0.1	987	18830	1.4
2201+044			1605	31025	1.3	506	9405	1.6
1101+384			3961	79812	-0.5	959	18504	1.1
0430+052			1541	30688	0.2	466	8853	1.1
1652+398			4155	81638	1.1	1021	20019	0.6
2344+513			2406	46796	1.3	717	13635	1.3
1514+004			1048	20807	0.2	342	6552	0.8
0402+379			3838	77762	-0.8	977	18799	1.2
1727+502			2914	57337	0.9	819	15886	0.8
0116+319			3857	77747	-0.5	969	18681	1.1
0802+243			3720	72675	1.4	899	17196	1.3
1214+381			4116	81701	0.5	964	18885	0.6
Σ blazars	55	12 915 351	37 074	736 085	1.4	9 626	185 245	3.7

cates that the unseparated cumulative excess is dominated by "γ-like" showers.

6.3.1 Analysis of the excess

In the following subsections, we have to review the two major cuts we introduced,

- the upper limit on the shower size, $N_e \leq 30\,000$, and
- the restriction to sources with redshift $z \leq 0.062$.

Both cuts are motivated by physics, but there is a certain ambiguity when fixing the actual cut value, as N_e only loosely correlates with the energy and the γ-ray horizon is only roughly known. It is thus important to check whether the result crucially depends on the actual cut value chosen for data analysis.
Due to the strong dependence on MC studies, also the angular resolution and thus the

- influence of the source bin size on the significance

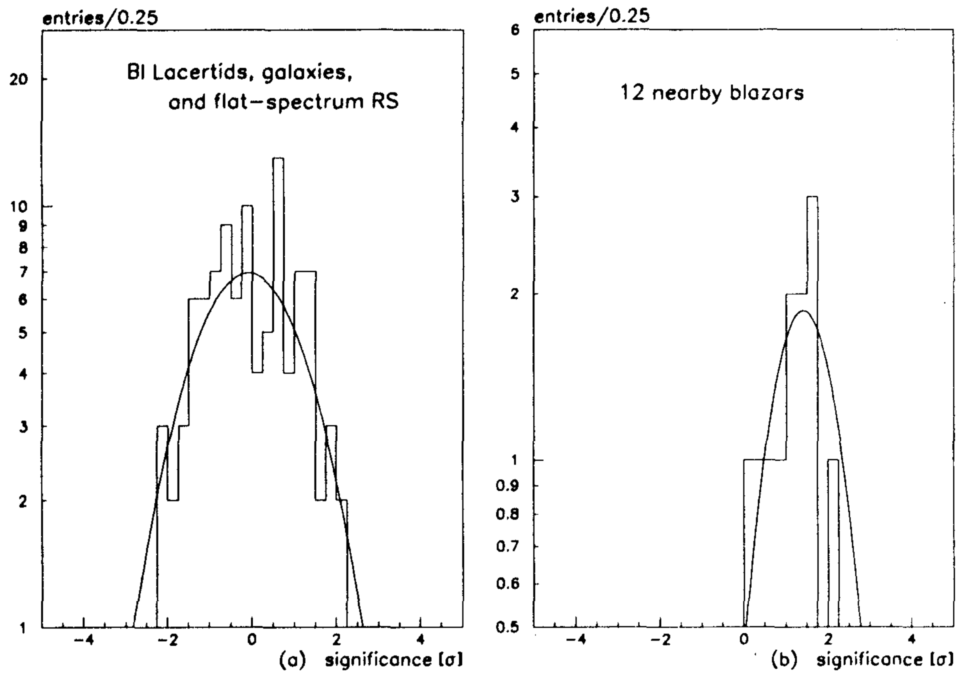

Figure 6.9: **Significance distribution for the galaxies, flat-spectrum radio sources, BL Lacertids (a), and the nearby blazars (b).**

has to be analyzed to verify that indeed $\sigma_{72\%} = 1.0°$ maximizes the signal. This also allows to discover possible deviations from the behavior expected for point-like sources.

Cut on shower size

The upper cut in N_e is motivated by our knowledge of the absorption of γ-rays in pair production processes with the microwave background. Whereas there is no doubt that a cut on the maximum primary energy is sensible, a cut in N_e with its somewhat problematic correlation to the energy (see Chapter 5) has to be analyzed further.
To study the influence of this cut, the blazar search is repeated without the upper restriction on N_e. As shown in Fig. 6.11 (a), the superposition yields an excess at the $3.7\,\sigma$ level with 9 626 on-source events and a background estimate of 185 245 ($n = 20$). This is about $0.4\,\sigma$ less than achieved in the analysis where events with $N_e \geq 30\,000$ are discarded, but as a remarkable result, the number of excess events is approximately the same with and without the cut. The decrease in significance is thus not due to a smaller excess, but caused by the higher background level accompanying the excess. This implies that no excess events are added when including large showers, an observation which is in accordance with expectation.
As a further support, Fig. 6.11 (b) shows the N_e-distribution of the excess events, i. e. the N_e-distribution of the source bin events after subtraction of the distribution for the

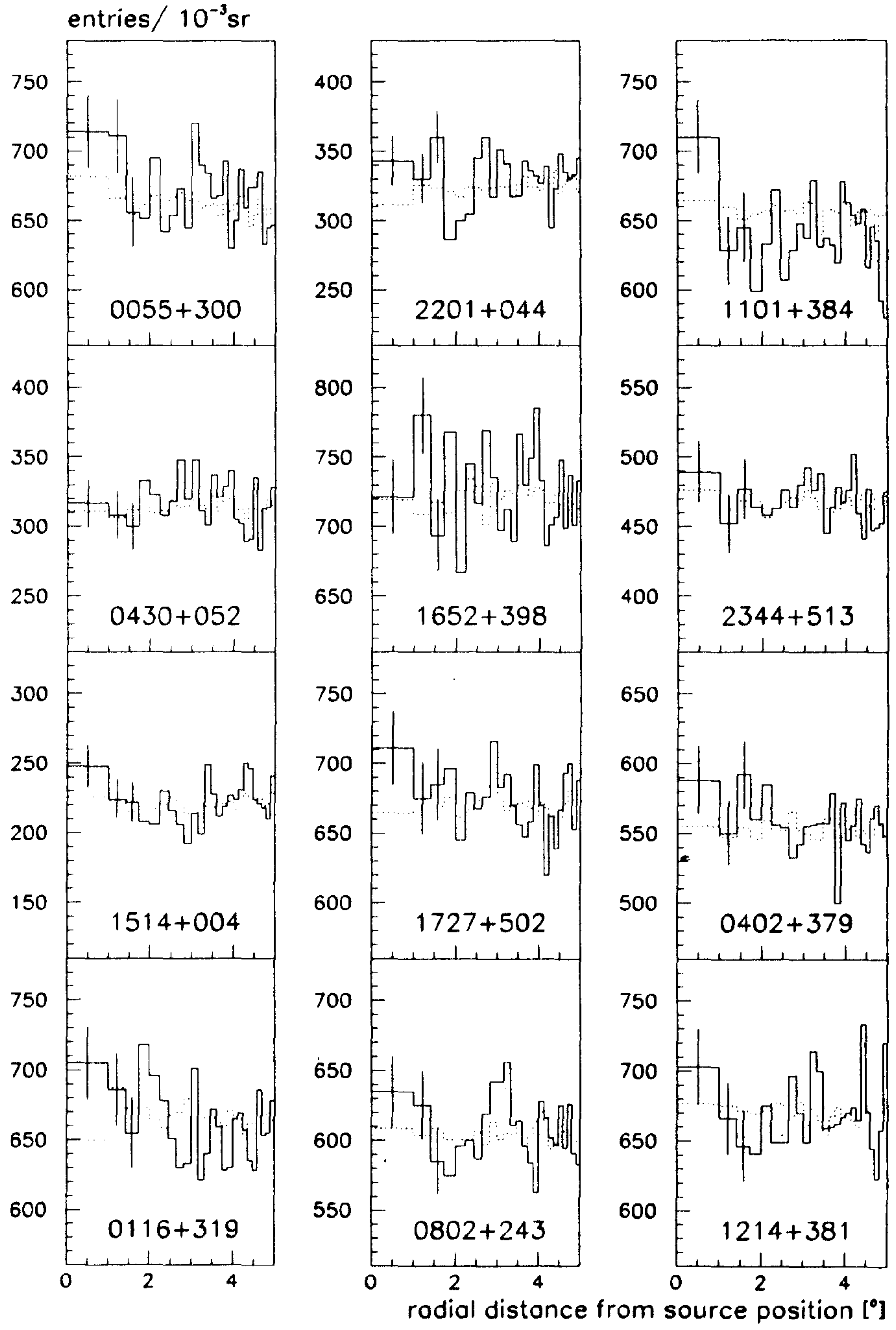

Figure 6.10: **Results for the single sources after γ/hadron separation: number of events as a function of the distance from the source position (solid line) and background estimate (dotted line).**

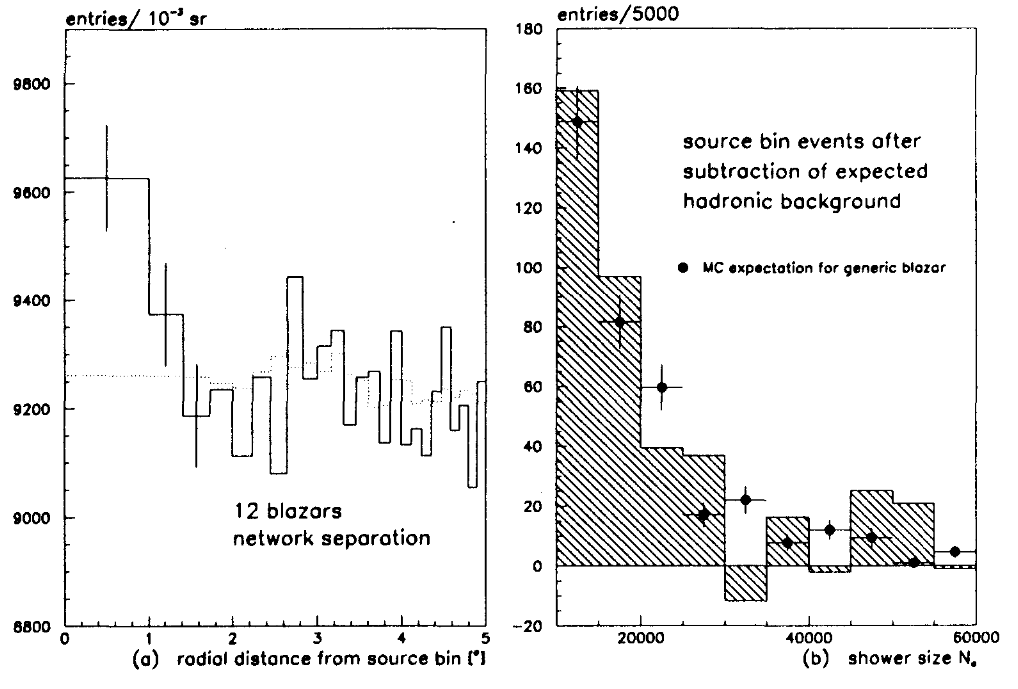

Figure 6.11: **Results with neural network separation, but without upper cut on shower size N_e: number of events as a function of the radial distance from the source position (a), and N_e-distribution of the source bin events after subtraction of the N_e-distribution for the background estimate (b).**

events making up the background estimate. The excess is clearly produced by showers of small size, and showers above $N_e = 30\,000$ mainly increase the background level.
We can now directly compare the N_e-spectrum of the excess events with the MC N_e-spectrum generated for the generic blazar applying the method described in Section 6.2.3. Fig. 6.11 (b) shows that the MC estimate (dots with error bars) is in good agreement with the experimental data. With respect to the results of the MC pre-analysis of the energy distribution of accepted events described in Section 6.2.3, we conclude that the major part of the showers has energies between 30 and 40 TeV. This has to be taken into account when discussing the implications on the actual strength of the infrared-to-optical background.

Redshift cut

In Chapter 2, we accounted for the necessity of restricting the analysis to *nearby* blazars. As it is nevertheless not at all well-defined what *nearby* means in terms of redshift, any cut on z remains arbitrary. We therefore have to study the dependence of the cumulated significance on the upper bound on z.
To extend the study to higher redshifts, we include the BL Lacs with $0.069 \leq z \leq$

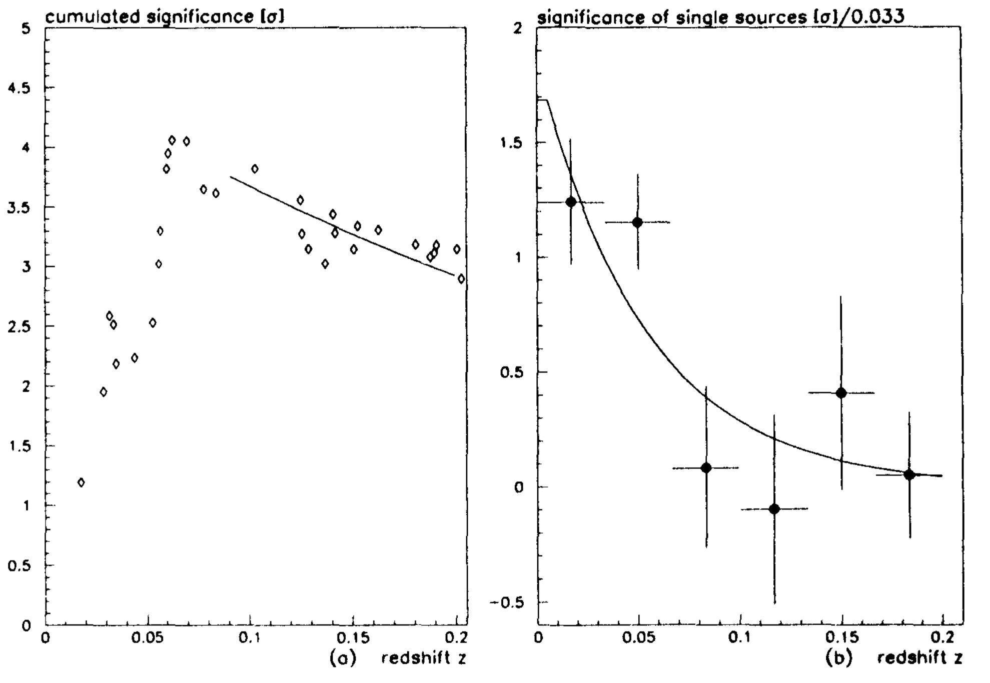

Figure 6.12: **Significance as a function of redshift for the cumulative signal (a) and the single sources (b). In (a) the line indicates the decrease in significance if no additional excess is accumulated.**

0.203, so the extended sample of 31 physically equivalent sources comprises all BL Lacs below 0.203 from [18] and the source distribution is rather homogeneous in redshift.
As illustrated in Fig. 6.12 (a), the cumulated significance increases rapidly up to $z \simeq 0.07$ and then starts to decrease rather slowly. The behavior for $z \geq 0.07$ equals the decrease expected in case no more excess events are accumulated: the solid line indicates the slope for $N_{off} = N_{on}$.
In fact, $z \simeq 0.06 \ldots 0.07$ is the cut value which approximately maximizes the significance, and we can divide the sources into two samples with only the nearby objects below $z \simeq 0.07$ contributing to the excess.
Fig. 6.12 (b) shows the significance of the *single* sources as a function of redshift, grouping the sources in bins with $\Delta z = 0.033$ to smooth the large spread of the individual significances. The dependence of the significance on z is very weak below $z \leq 0.06$, i.e. the region of the original blazar sample. For the whole range of redshifts up to 0.2, nevertheless there is a clear decrease in source significance with a mean value compatible with 0 above $z \simeq 0.07$.
It is tempting to interpret the decrease in significance and the non-detection of BL Lacs above $z \simeq 0.1$ by pair-absorption due to the infrared background, especially as the sources of the BL Lac anti-sample are physically equivalent to the blazars. Intrinsic differences between the sources of the two catalogues can thus be excluded if we assume

that luminosity evolution does not play a significant role below $z \leq 0.2$.
In fact, external absorption is more likely than apparent geometrical weakening, as a flux $\propto 1/d^2$, with d being the distance, is only expected for "standard candles". Apart from the fact that the excess for sources below $z \simeq 0.06$ only weakly depends on the distance (see Fig. 6.12 (b)), there is another major drawback to this scenario. The geometrical decrease can easily be covered by the large lever arm provided by the (unknown) spectral index of the source: for two sources with equal flux at 1 TeV, a difference of 0.4 in the spectral index is sufficient to compensate a factor 2 in distance and to give equal flux at 50 TeV. According to the proton blazar model prediction, the spectral index for the blazars as predicted in [11] varies from 2 to 3.2, with a mean value of 2.8 ± 0.4, and the change may even be larger in high states of γ-emission: *we are in fact not dealing with "standard candles".*
The most likely reason for the cutoff therefore is *external absorption* becoming relevant for $z \geq 0.07$. As in this case, $I \propto e^{-\tau_{\gamma\gamma}}$ with $\tau \propto d$ (see Eq. 2.31), a *sharp* cutoff is expected. The excess accumulated in this analysis does not yet allow to settle this point or to derive limits on the infrared background. More sensitive observations are required to substantiate these conclusions. We will return to this topic in the discussion of the combined results from the 1994/95 Geiger tower and the 1989-1992 scintillator analysis in Section 6.5.

Check of angular resolution

In Section 6.2.2 we have shown that from MC predictions and moon shadow analysis, the angular resolution of the HEGRA scintillator array for γ-shower sizes above $N_e \geq 10\,000$ is expected to be $\sigma_{63\%} = 0.9°$. Hence the optimal source bin size yielding maximum sensitivity is $\sigma_{72\%} = 1.0°$. In order to check whether the excess is in accordance with expectation and to study possible deviations from point-source behavior, we calculate the significance for source bin sizes from 0.1° to 2.0°. Fig. 6.13 illustrates that indeed the maximum is at $\sigma_{max} = 1.0°$. The solid line indicates the expected curve if the sources are point-like and the dispersion of the signal is solely a result of the finite angular resolution of the instrument. In this case, the smearing has Gaussian shape and signal-to-noise follows

$$\frac{\text{signal}}{\text{noise}} \propto \frac{\text{prob}(\sigma \leq \sigma_{sb})}{\sqrt{\Omega_{sb}}} \propto \frac{1 - e^{-\frac{\sigma_{sb}^2}{2\sigma^2}}}{\sigma_{sb}}, \tag{6.12}$$

(see Eq. 3.7) with σ_{sb} being the source bin size and $\Omega_{sb} = 2\pi(1 - \cos\sigma_{sb})(\propto \sigma_{sb}^2$ for small $\sigma_{sb})$ the corresponding solid angle. For the dotted line, the pointing error of $\simeq 0.3°$ from the moon shadow analysis has been taken into account by enlarging the source bin size. Within the statistical error, both curves are in accordance with the experimental data. Note again that a γ-ray spectrum flatter than the overall cosmic ray spectrum leads to a better angular resolution for γ-rays and may thus counteract the deterioration by pointing inaccuracies. Fig. 6.13 nevertheless confirms the expectation that the results are not affected by pointing errors of the order 0.3°.
Fig. 6.13 also indicates that the behavior of the excess is in agreement with the expectation for point-like sources and shows no evidence for any extension, but this would

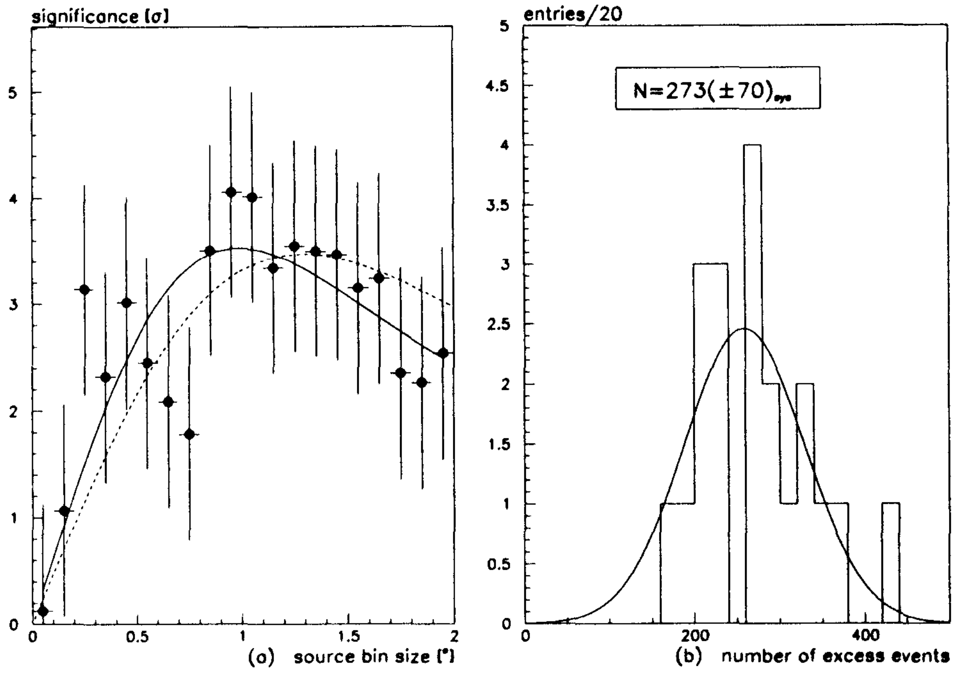

Figure 6.13: **(a) Significance as a function of the source bin size. The lines indicate the expectation for point-like sources with and without taking into account a pointing error of $\simeq 0.3°$ (dotted resp. solid line). (b) Number of excess events after efficiency correction.**

hardly be expected as the predicted halo sizes in [39] (see Section 2.2.4) cannot be resolved with the angular resolution of current scintillator arrays. This remains a challenge to future high resolution detectors.
Fig. 6.14 shows the core position of the source bin events together with the position of the scintillator huts. As a consequence of the quality cuts, the core distribution is relatively smooth.

6.3.2 Flux calculation

The a priori assumption of this analysis is the equality of the individual sources of the sample. For the calculation of the flux corresponding to the observed excess, a weighting of the sources with respect to their individual observation time is therefore inconsistent, as the different energy thresholds for the sources according to their declinations have been considered by calculating the threshold for the "generic" blazar.
Furthermore, a rescaling of the flux of individual sources to a common energy threshold is dangerous, as no individual source has a significant excess. It is therefore the most consistent way to take the overall excess of the whole sample and calculate a flux using

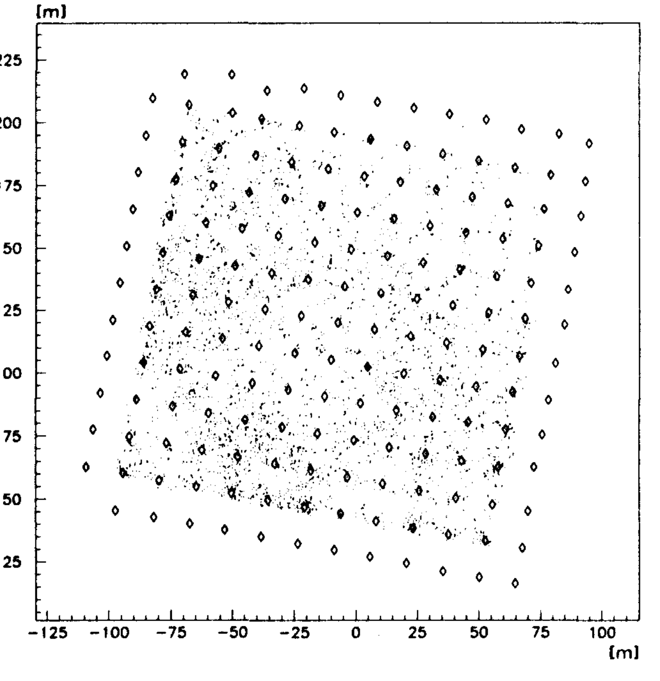

Figure 6.14: **Core position of the source bin events (in coordinates of the reconstruction program). The rhombs indicate the positions of the scintillator huts (without the dense inner array).**

the threshold energy of the generic blazar. We use Eq. 6.7

$$\Phi(E \geq E_{thresh,\gamma}) = (1.52 \pm 0.01) \cdot 10^{-5} E_{\mathrm{TeV}}^{-1.67 \pm 0.02}\ \Omega\ \frac{N_{excess}}{0.72\, N_{sb}}\ \mathrm{cm}^{-2}\mathrm{s}^{-1}\mathrm{sr}^{-1} \quad (6.13)$$

with

$$N_{excess} = \frac{N_{on} - \alpha\, N_{off}}{\epsilon_\gamma}, \quad (6.14)$$

where the correction factor 0.72 has to be applied as the source bin contains only 72% of the source events. Note that to calculate an *integral* flux for $E \geq E_{tresh,\gamma}$ we have to use the values for N_{excess} and N_{sb} determined without upper cut on N_e.
Apart from the error in Φ_{CR} two other quantities enter with a systematic error, ϵ_γ and N_{excess}. The systematic errors on ϵ_γ were analyzed in Chapter 4 and 5 and add up to

$$\epsilon_\gamma = 0.83 \pm 0.01 \pm 0.09 \quad (6.15)$$

for a network cut $\xi_{cut} = 0.4$, including both MC and detector effects as far as their influence is known and can be estimated.
This error is far too small to account for the dependence of N_{excess} on the cut value ξ_{cut} in the network output. Whereas the quality factor and the significance of the excess

depend on ξ_{cut} in a way consistent with MC expectation, the flux and therefore the number of excess events should be independent from ξ_{cut}. The spread of N_{excess} is an intrinsic error of the neural net analysis and by far the most important systematic error on the flux. To determine N_{excess} and its systematic error due to the ambiguity of the network cut, we histogram N_{excess} for 20 equidistant cut values from 0.05 to 1. The result is shown in Fig. 6.13 (b). The number of excess events in fact can only be estimated with an accuracy of about 30 %:

$$N_{excess} = 273 \pm 16 \pm 70. \tag{6.16}$$

Note that applying this procedure gives a number of excess events and thus a flux *independent of the cut value*, with the dependence on ξ_{cut} being included in the systematic error.
Summarizing all values derived above gives an integral flux of

$$\Phi(E \geq E_{thresh}) = (1.4 \pm 0.4\ ^{+1.0}_{-0.7}) \cdot 10^{-13}\text{cm}^{-2}\text{s}^{-1}. \tag{6.17}$$

As about 300 events are accumulated in 150 days of full-time observation, the daily excess rate of the generic blazar is 2. This illustrates again the enormous effort which is necessary to separate the relevant showers from the hadronic background.
A rough calculation of the flux by simply dividing the number of excess events by the geometric size of the array ($150\times160\,\text{m}^2$) and the total observation time after correcting for the dead time gives a flux of $1.2 \cdot 10^{-13}\text{cm}^{-2}\text{s}^{-1}$. This cross-check indicates that indeed the geometric array size equals the effective size after the rather severe border cut.

6.4 Analysis of 1989-1992 scintillator data

In the precedent section, a significance of about 4σ with 50 000 000 events and a γ/hadron separation quality factor $Q \simeq 2$ has been achieved. As shown in 3.7, signal-to-noise in air shower analysis behaves like

$$\frac{\text{signal}}{\text{noise}} \propto \sqrt{A\,T}\,\frac{1}{\Delta\alpha}\,Q\,, \tag{6.18}$$

i. e. a quality factor of 2 corresponds to 4 times the observation time T of an analysis without γ/hadron separation.
Between August 5, 1989, and June 5, 1992, the HEGRA scintillator array was operated with a total observation time of 697 days (60 243 598 s), during which 250 000 000 events were taken and analyzed [74]. As a major difference to the upgraded array operated since 1992, HEGRA did not include the dense inner region at that time.
Upper limits on the flux of various extragalactic sources have been derived, but only Mrk 421 with an upper flux limit $\Phi(90\%) = 1.8 \cdot 10^{-13}\text{cm}^{-2}\text{s}^{-1}$ and Mrk 501 with $\Phi(90\%) = 9.9 \cdot 10^{-14}\text{cm}^{-2}\text{s}^{-1}$ [74] are also included in the blazar source sample. In this section, these scintillator data are re-analyzed to search for an excess both from the blazar and the BL Lac sample with $0.069 \leq z \leq 0.203$. If the excess obtained after

application of the Geiger tower γ/hadron separation is in fact due to a γ-ray excess from the blazar sample, the archival scintillator data without separation but with 5 times more events should give an excess with a significance of the same size.
The angular resolution in this period has been determined with various methods, including a moon shadow analysis which yields a 6σ deficit. Including an absolute pointing error of 0.2° to 0.3° derived from the moon shadow position, $\sigma_{63\%} = 0.99°$ at $\log N_e \geq 4.0$ is taken for this analysis. The source bin size is therefore 1.12° instead of 1.0°, but this only slightly deteriorates the sensitivity.
The following cuts are applied to search for a blazar signal below 100 TeV:

- Only events with at least 13 scintillator counters contributing to the signal are accepted. This condition guarantees stable trigger conditions even when AIROBICC is working.
- The shower size is restricted to $10\,000 \leq N_e \leq 30\,000$.

In order to prevent showers with higher energy but large zenith angle θ from imitating small showers, a zenith angle cut $\theta \leq 25°$ is applied in the original analysis [74]. As one of the sources (1514 + 004) is completely discarded by this cut, we adopt the zenith angle cut $\theta \leq 40°$ from the Geiger tower analysis. The larger zenith angle range gives flat radial distributions for all sources, including those with extreme declinations compared to the latitude of the HEGRA array. This minimizes systematic errors in the background estimation.
In addition,

- showers with a core at a distance of less than 20 m from the border of the array are discarded.

This cut is more severe than the original border cut of 10 m in [74], but it is motivated by the observation that the number of shower cores per unit area increases significantly faster when approaching the border than expected from pure geometry. This indicates that a considerable amount of showers with core outside the array incorrectly piles up within $\simeq$ 20 m. As the reconstruction of the primary particle's direction makes use of the core position (see Chapter 3), including these showers deteriorates the angular resolution especially for small showers. The 20 m border cut applied in the following analysis roughly corresponds to the border cut used in the Geiger data analysis, where it was motivated by the actual size of the Geiger matrix. With this cut, the effective array size approximately equals the geometric size.
The background is derived by a parabola fit to the radial distribution between 1.94° and 4.3°. In order to check the reliability of this method, the background is also estimated by analyzing pseudo-sources at the same declination as the original source, but shifted by 3.6° in right ascension. This allows to check whether a possible excess is due to systematic effects resulting from the source's declination.
Tab. 6.7 gives the results for the generic nearby blazar and for the BL Lac anti-sample with and without the cut on the maximum shower size.
The results on the individual blazars are summarized in Tab. 6.8, and the superpositions of the 12 blazars and the 19 BL Lacs are shown in Fig. 6.15. The significance of the

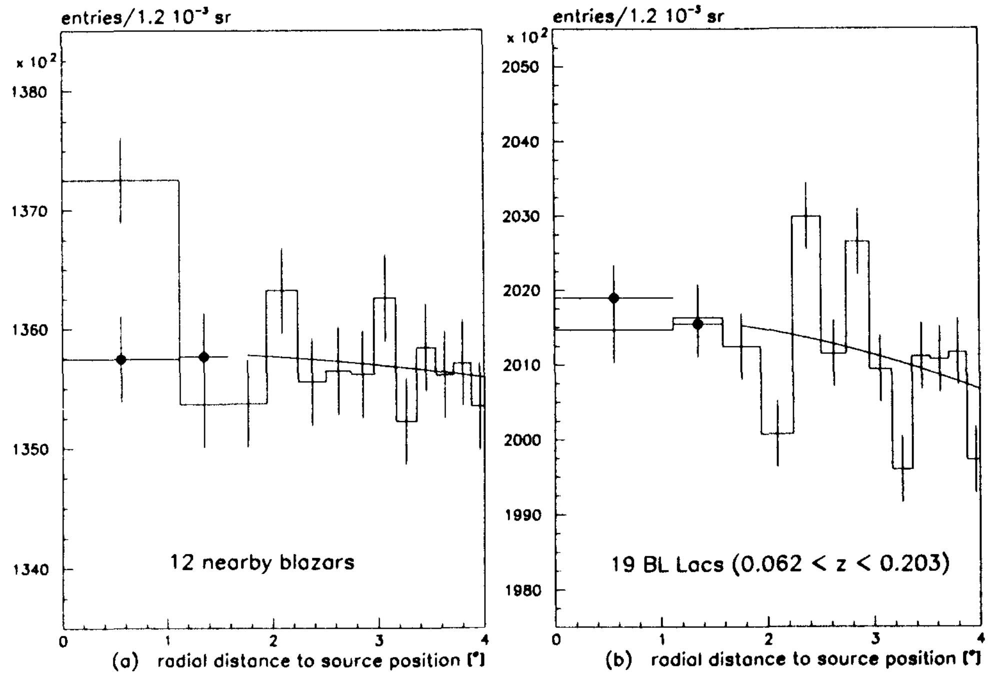

Figure 6.15: **Superposition of the nearby blazars (a) and BL Lacs with $0.069 \leq z \leq 0.203$ (b) (1989-1993 scintillator data). Dots with error bars indicate the result for the superposition of pseudo-sources with $\alpha_{pseudo} = \alpha + 3.6°$.**

generic blazar is $3.2\,\sigma$ for $N_e \geq 10\,000$ and increases to $3.7\,\sigma$ if the shower size is limited to $10\,000 \leq N_e \leq 30\,000$. Both methods of background estimation lead to similar results, thus the excess is not an artifact of the source positions.
Again, the anti-sample with BL Lac objects at redshifts $0.063 \leq z \leq 0.203$ shows no significant excess, whereas the significance of the generic nearby blazar is $3.2\,\sigma$ for $N_e \geq 10\,000$ and $3.7\,\sigma$ for $10\,000 \leq N_e \geq 30\,000$. The integral flux

$$\Phi(E \geq 50\mathrm{TeV}) = (1.5 \pm 0.4\ ^{+1.0}_{-0.7}) \cdot 10^{-13}\mathrm{cm}^{-2}\mathrm{s}^{-1} \tag{6.19}$$

is in accordance with the flux estimated for the Geiger tower data sample. As no

Table 6.7: **Results for the generic nearby blazar and the BL Lac with $0.069 \leq z \leq 0.203$ for $\theta \leq 40°$ with and without upper cut on the shower size ($N_e \leq 30\,000$).**

	$10\,000 \leq N_e \leq 30\,000$			$10\,000 \leq N_e$			$\Phi^{90\%}_{u.l.}(> 50\,\mathrm{TeV})$
source	N_{on}	N_{off}	sign. [σ]	N_{on}	N_{off}	sign. [σ]	[$\mathrm{cm}^{-2}\mathrm{s}^{-1}$]
blazar	137 250	135 837	3.7	290 791	288 977	3.2	
BL Lac	201 466	201 730	-0.5	430 520	430 130	0.5	$7.4 \cdot 10^{-14}$

γ/hadron separation is applied in the scintillator data analysis, the systematic error is

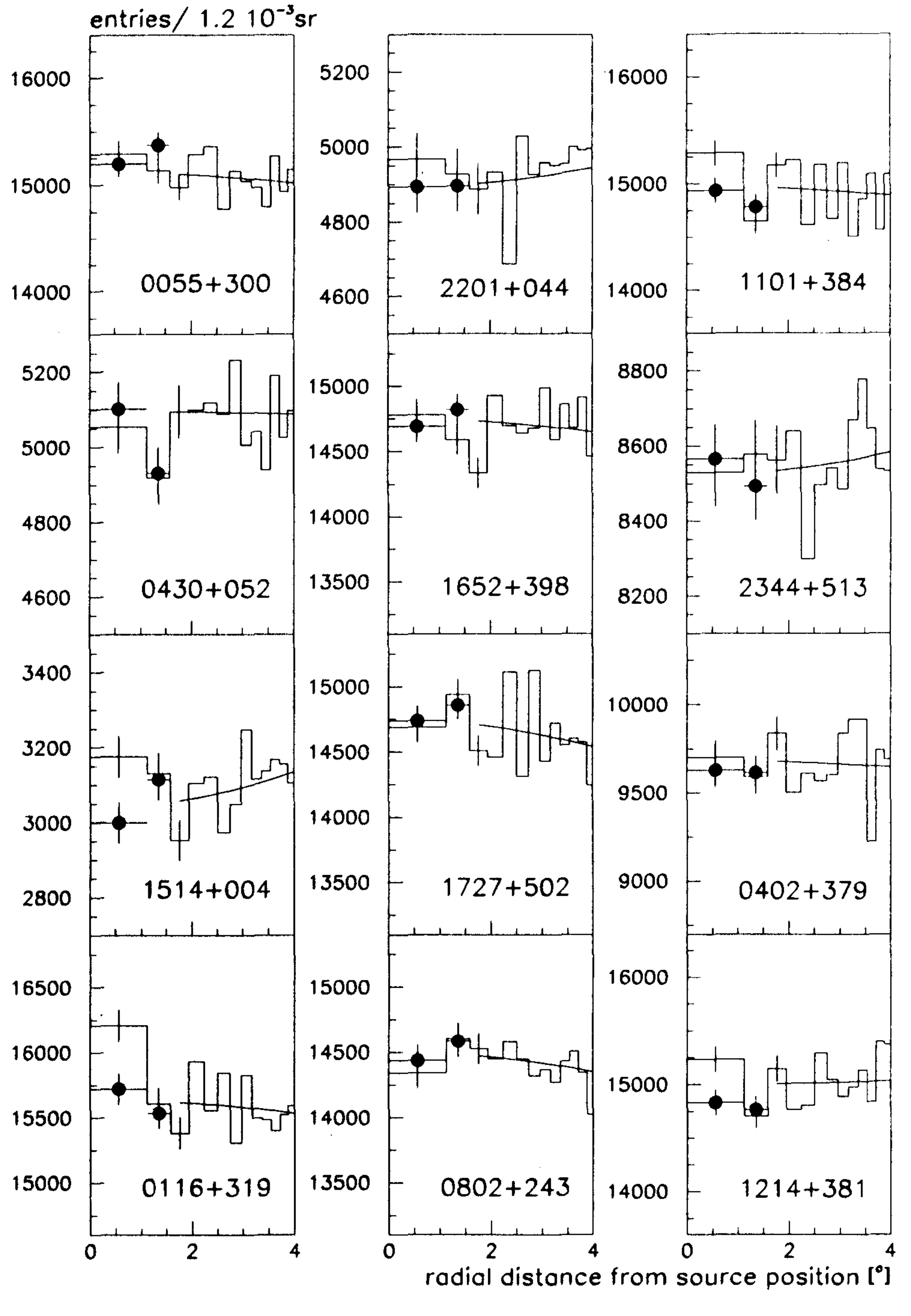

Figure 6.16: **1989-1992 results for the individual blazars. Dots with error bars indicate the result for pseudo-sources with $\alpha_{pseudo} = \alpha + 3.6°$.**

slightly smaller, but as uncertainties remain large, we quote the same values as above. The Geiger tower data and the 1989-1992 scintillator data are statistically independent, thus it is possible to combine both results. Fig. 6.17 shows the *combined* significance as a function of redshift (see Fig. 6.12). The total significance of the generic blazar is $5.5\,\sigma$, and again the maximum value is at $z \simeq 0.07$.
Comparing the significances of individual sources (Fig. 6.16) yields an interesting result: 0116+319 at $z = 0.059$ has an excess of $4.4\,\sigma$ and thus dominates the overall excess.

Table 6.8: **1989-92 results for the blazar sample.**

		$10\,000 \leq N_e \leq 30\,000$			$10\,000 \leq N_e$		
source	z	N_{on}	N_{off}	sign. $[\sigma]$	N_{on}	N_{off}	sign. $[\sigma]$
0055+300	0.017	15287	15220	0.5	32058	31808	1.3
2201+044	0.028	4967	4864	1.4	11184	11169	0.2
1101+384	0.031	15288	14977	2.4	31874	31498	2.0
0430+052	0.033	5053	5114	-0.8	11315	11459	-1.3
1652+398	0.034	14778	14699	0.6	31507	31366	0.8
2344+513	0.044	8529	8522	0.1	18991	18641	2.4
1514+004	0.052	3175	3008	2.9	7285	7070	2.4
1727+502	0.055	9699	9712	-0.1	21231	21209	0.1
0402+379	0.055	14691	14665	0.2	30682	30616	0.4
0116+319	0.059	16206	15622	4.4	33647	32801	4.4
0802+243	0.060	14342	14497	-1.2	29340	29694	-2.0
1214+381	0.062	15235	14937	2.3	31677	31646	0.2
Σ blazars		137 250	135 837	3.7	290 791	288 977	3.2

This is especially interesting if we compare the significances of the individual sources derived in the 1994/95 Geiger data analysis and the 1989-92 scintillator analysis. The inset of Fig. 6.17 illustrates that in both data sets, 0116+319, 1101+384, and 1514+004 are the most significant sources: the combined significance of 0116+319 is $4.9\,\sigma$. We will review this result after a short summary of additional analyses of the blazar sample.

Summary of further blazar searches

Following the discovery of small evidence for $\geq$50 TeV γ-ray emission from the 12 blazars, also data taken in combination with the AIROBICC detector have been tested for a cumulative excess. AIROBICC has a smaller angular resolution of $\simeq 0.4°$ and a lower energy threshold of $\simeq$ 20 to 30 TeV for γ-showers [86]. As a major drawback, it is only operated in clear, moonless nights. For source stacking, the small duty cycle is a severe shortcoming, as not all sources are monitored each day like in the combined scintillator/Geiger analysis. The composition of the generic source hence is a function of time, and only about 5 sources are actually stacked each night.
When searching for an excess in AIROBICC data, a sufficiently large observation time has to be accumulated to smooth the on-time distribution of the sources, but even then there is a high probability of missing periods of high emission.
A re-analysis of the data taken in the first year of stable AIROBICC performance, i. e. between March 1992 and March 1993, with most of the data from the latter months of this period, yields an excess of $3.9\,\sigma$ for the generic blazar [146]. Cuts applied in

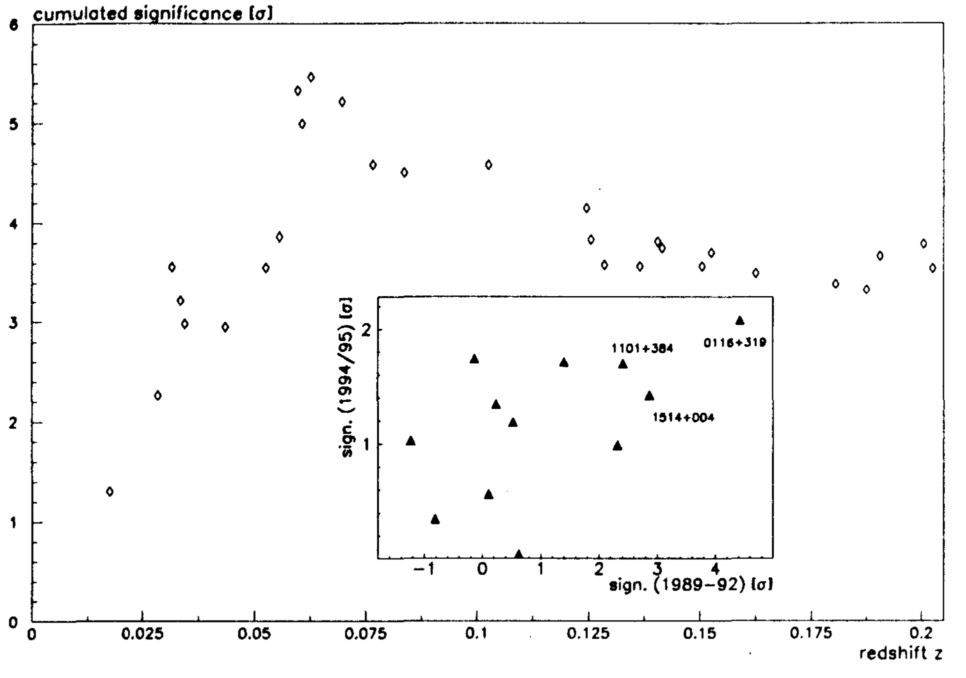

Figure 6.17: **Combined cumulated significance (1994/95 Geiger data analysis and 1989-92 scintillator analysis) as a function of redshift. The inset shows the individual significances of both data sets.**

this analysis include a restriction of the light density L_{90} at a distance of 90 m from the shower core to $8000\,\mathrm{photons/m^2} \leq L_{90} \leq 22000\,\mathrm{photons/m^2}$ corresponding to the 50 to 100 TeV energy window also chosen for the Geiger tower analysis. No γ/hadron separation has been applied to the early AIROBICC data.
As a striking result, the significance is considerably smaller when the energy threshold is lowered to 30 TeV or less. This behavior is not yet fully understood, but a possible explanation may be the lower quality of the detector performance below 50 TeV.
The analysis of AIROBICC data taken between December 1993 and September 1995 does not yield an excess of the expected size: with a source bin radius of 0.41° and new γ/hadron separation techniques [147], the excess is $1.7\,\sigma$. $2.4\,\sigma$ are in fact achieved with a bin size of 1.0°, but it is not possible to account for this source bin size unless AIROBICC suffers from a rather large pointing error. A small smearing of the excess is expected when sources with different declinations are stacked, but the effect should not be so high.
In 13 months of pure scintillator data taken between 1994 and 1996, only a marginal excess is seen. Quality checks both for the 93-95 AIROBICC data and the 94-96 scintillator data are in progress.
The results are summarized in Tab. 6.9.

Table 6.9: **Summary of blazar search results above 50 TeV.**

	time period	$\sigma_{72\%}$	Q	sign. [σ]
scintillator and Geiger array	11/94-3/95	1.0°	$\simeq$2	4.1
scintillator array	8/89-6/92	1.12°	-	3.7
scintillator array	3/94-4/95	1.0°	-	1.2
AIROBICC	3/92-3/93	0.4°	-	3.9
AIROBICC	12/93-9/95	0.41°	$\simeq$2	1.7
		1.0°	$\simeq$2	2.4

6.5 Discussion

The evidence for $\geq$50 TeV γ-emission from a sample of blazars with moderate redshift is a remarkable result for several reasons:

- γ-ray flux at these energies is strong support for proton acceleration in jets and thus the proton blazar model, which in contrast to models based on synchrotron-self-Compton mechanisms *generally* predicts high energy flux.

As outlined in Chapter 2, a γ-energy of 10 TeV is the "demarcation line" [148] between models based on synchrotron-self-Compton emission of electrons and the proton blazar model. In order to produce $\geq$10 TeV γ-rays, the acceleration in SSC models would have to take place in the immediate vicinity of the black hole, but the dense infrared background in this region would not allow the γ-rays to quit without severe energy loss. In contrast to this, TeV γ-emission is a compelling attendant of proton acceleration.
In Fig. 6.18, the flux estimation for 10 of the 12 blazars is confronted with the prediction based on the proton blazar model as given in [11]. The experimental flux approximately equals the prediction for the average blazar flux if *no* external absorption takes place and if we assume that the stacking method slightly overestimates the blazar flux. This is not unlikely, as the theoretical predictions show blazars in quiet states of γ-emission (the data for the multifrequency spectra were taken non-simultaneously), whereas the experimental flux may be dominated by blazars in high states of emission. Although there is no evidence for periods of rapid increase, HEGRA detection may strongly depend on high emission states. In this case, the stacking method may give rates which do not represent "typical" blazars.
The evidence for $\geq$50 TeV γ-emission and the striking fact that the observed flux equals the *non-absorbed* proton blazar prediction has another important implication:

- γ-ray emission of the observed intensity at 50 TeV rules out any scenario predicting a high diffuse infrared background (e. g. the estimates of Stecker et al. [9]).

This has been verified independently by recent Whipple observations of Mrk 421 at high zenith angles, showing that the spectrum continues up to at least 10 TeV [150] (note that the analysis of Stecker et al. is actually based on the apparent cutoff in the Whipple data for Mrk 421). HEGRA telescope detections of Mrk 421 [115] furthermore

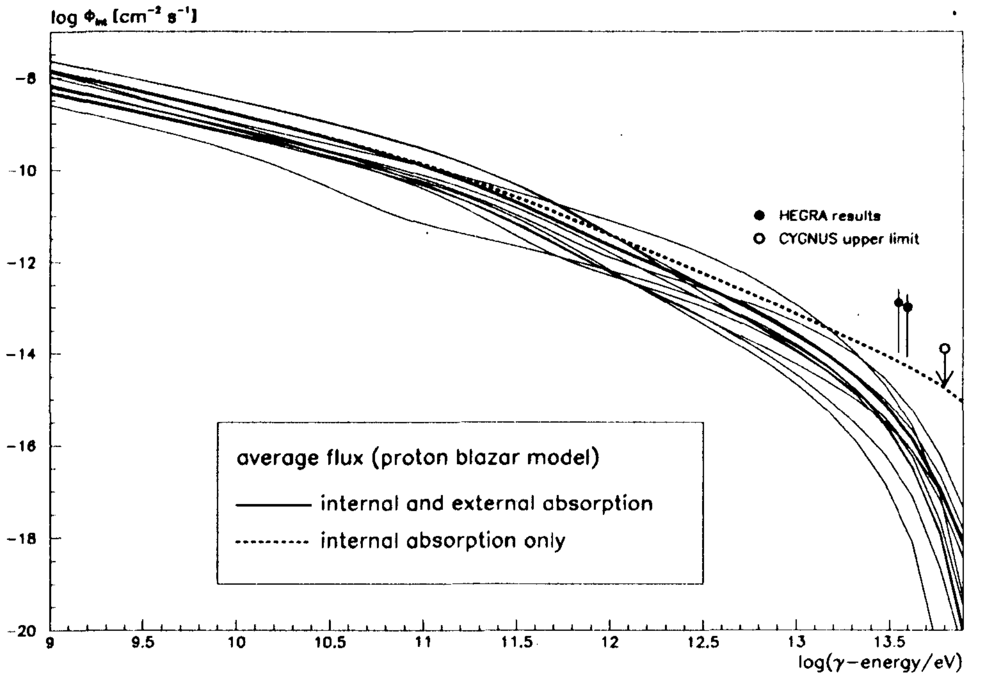

Figure 6.18: **HEGRA flux values and theoretical predictions for the blazars taken from [11]. The thin solid lines indicate the flux of individual blazars with internal and external absorption, the thick solid line is the average. The dotted line shows the average flux without external absorption. The CYGNUS upper limit on the blazar sample is added [149].**

show a steepening of the spectral index in the TeV region which has not been taken into account by these authors. Their value thus turns out to be an upper limit rather than a measurement.

Does the result imply that there is *no* absorption by infrared photons ?

In fact, there are lower limits to the diffuse infrared background provided by IRAS number counts, and the optical depth at 50 TeV for an extragalactic source at a distance of 120 Mpc ($z = 0.03$, $H_0 = 75\,\mathrm{km\,s^{-1}\,Mpc^{-1}}$) therefore has a minimum value of $\tau \simeq 3$.

Although the excess hardly allows to derive values for the infrared background at energies where HEGRA is sensitive, the results are not in contradiction to infrared background estimates: from Fig. 6.4 (b), we know that γ-rays detected by HEGRA pile up at low energies, thus HEGRA actually probes the infrared background at $\epsilon \simeq 0.01\,\mathrm{eV}$. We can now qualitatively pin down the infrared background at this energy by taking together the two main results of the precedent analysis: (1) no sources are detected above $z \simeq 0.07$, and (2) an excess at the $5\,\sigma$ level is observed for 0116+319 at $z = 0.059$. Both results imply that if the non-detection of the BL Lacs at higher redshift is due

to external absorption, 0116+319 indicates the border $\tau_{\gamma\gamma} = 1$ in Fig. 2.10. As the mean γ-ray energy is 35 TeV, $\tau_{\gamma\gamma} < 1$ for $z = 0.059$ requires a background radiation density $\epsilon^2 n(\epsilon) \lesssim 2 \cdot 10^{-4}\,\mathrm{eV\,cm^{-3}}$ at $\epsilon = 0.01\,\mathrm{eV}$, thus a detection of 0116+319 implies that $\epsilon^2 n(\epsilon)$ at 0.01 eV is a factor of 3 lower than given in Fig. 2.10. This is of course neither a measurement of $\epsilon^2 n(\epsilon)$ nor a confirmation of models predicting low values for $\epsilon^2 n(\epsilon)$: it only shows that a detection of nearby γ-ray sources above 30 TeV is not in contradiction to current theoretical estimates: note that Fig. 2.10 shows the *average* infrared photon density for various CDM and CDHM models.
In addition, cascade processes as described in Chapter 2 may counteract the absorption and increase the source luminosity even at TeV energies, mainly by inverse-Compton scattering of $e^{\pm}$ produced in absorption processes off the 3 K radiation. Furthermore, there are other processes which may increase the flux. In the proton blazar model as used for the flux predictions, all the TeV flux is assumed to arise from a jet radius at which the synchrotron radiation in the infrared becomes optically thin (one-zone model), but additional cascade radiation may arise from higher jet radii [151].
An additional component of high energy γ-rays may also come from the decay channel

$$p\,\gamma \longrightarrow \pi^+ n \quad , \tag{6.20}$$

which is one of the proton cooling processes. These ultra-high energy cosmic rays may initiate cascades on their way from the source to the observer and thus increase the TeV γ-flux. Note that a source distance of 100 Mpc roughly corresponds to the decay length of the highest energy neutrons. If the decay and thus the cascading takes place in our neighborhood, the resulting γ-rays do not suffer absorption any more. Detailed calculations on this bypass mechanism are in preparation [152].

When comparing the flux estimate of the generic blazar to previously published upper limits on individual objects belonging to the sample (Mrk 421 and 501), the flux appears to be rather high. Upper limits from CYGNUS and EAS-TOP are in fact *below* the generic blazar flux (see Section 2.3). It is difficult to assess these upper limits, but there are several problems connected to upper limits in TeV-γ-astronomy. There is no established source above 10 TeV, thus it has never been possible to tune analysis methods on sources with known flux. Efficiencies and energy thresholds which enter the upper limit calculations are therefore only roughly known and crucially depend on MC studies. The uncertainty especially of those MC codes which are not based on the time-consuming EGS 4 and GHEISHA/FLUKA codes (which at least have shown their reliability in various applications) is expected to be rather large and often not considered in upper limit calculations.
In addition, MC statistics tends to be poor, and various authors only study fixed incident angles and energies. This is especially dangerous in cases where γ/hadron separation techniques are based on these MC samples.
To sum up, upper limits are only rough guide-lines in TeV-astrophysics, and this will only change with the discovery of individual sources at 50 TeV which may then serve as tools for tuning data analysis methods. The flux of the generic blazar is therefore not in conflict with existing upper limits.

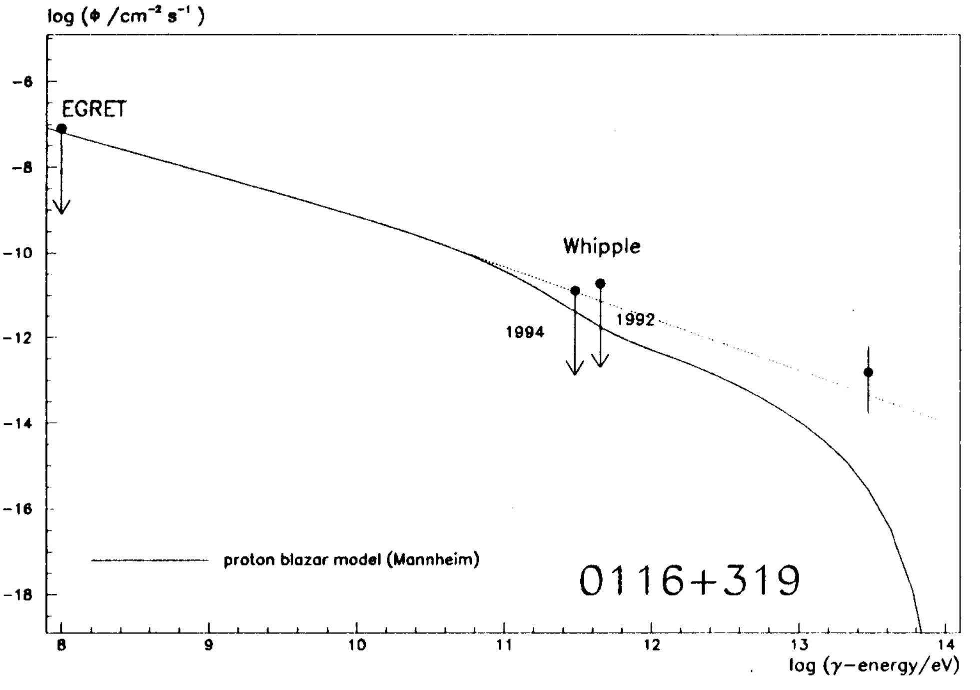

Figure 6.19: **Integral flux limits for 0116+319 at energies above 100 MeV. Values are taken from [4](EGRET), and [76](Whipple). The solid line represents the prediction of the proton blazar model (Mannheim [11]) including external absorption.**

The X-ray-selected AGN 0116+319

As shown in Fig. 6.17, both the Geiger data analysis and the analysis of the 1989-92 scintillator data yield the most significant excess for 0116+319. This is also true for the AIROBICC analysis quoted in Section 6.4, where the excess of 0116+319 is $2.9\,\sigma$ and thus dominates the overall excess like in the scintillator data.
0116+319 is an X-ray-selected AGN from the Einstein Observatory Extended Medium Sensitivity Survey (MS). In addition, radio data indicate that 0116+319 is a flat-spectrum radio source with a spectral index slightly below 0.5 [62]. The AGN has neither been detected by EGRET [4] nor by Whipple [76]. The high energy part of the spectrum is shown in Fig. 6.19.
1214+381 is another X-ray selected AGN from the MS catalogue and also has a comparatively high significance in the 1989-1992 sample. This is a rather interesting result, as Stecker et al. [77] recently suggested that X-ray selected BL Lac objects (XBLs) are the most promising TeV sources. In the synchrotron-self-Compton model, the X-ray component of the multifrequency spectra of XBLs is supposed to arise from the high energy tail of the synchrotron radiation, whereas in radio-selected BL Lacs (RBLs), the X-ray emission is from Compton up-scattering. This implies that due to *intrinsic* differences between the two types of BL Lacs, which cannot be explained by jet ori-

entation alone, the maximum electron energy is higher in XBLs than in RBLs. This would make XBLs the most likely sources of TeV emission.
The known TeV sources, Mrk 421, Mrk 501, and also 2344+514 (which has tentatively been detected with the Whipple telescope [153]) are in fact XBLs, but the statistical significance is too small to give compelling evidence for XBLs being the "typical" TeV source. In spite of the classification of 0116+319 as an X-ray selected flat-spectrum radio source, the observation is nevertheless no support for this hypothesis, as 50 TeV γ-rays cannot be explained by models based solely on electron acceleration.
Applying the stacking method to the 21 X-ray selected AGN with $z \leq 0.07$ from the MS catalogue (see [60]) yields no significant excess (see Tab. 6.10) for the Geiger tower data set. For most of these sources, no radio data are available, and it is thus not possible to select flat-spectrum sources. Observational data in different energy regions are urgently needed to find additional candidates for TeV emission.

Table 6.10: **Results for the stacking of 21 X-ray selected AGN from [60] with $z \leq 0.07$ ($n = 10$) with and without the upper cut on the shower size ($N_e \leq 30\,000$). Φ is the upper limit on the integral flux above E_{thresh}.**

source	no separation N_{on}	$10 \cdot N_{off}$	sign. [σ]	separation N_{on}	$10 \cdot N_{off}$	sign. [σ]	$\Phi^{90\%}_{u.l.}(> 50\,\mathrm{TeV})$ [$\mathrm{cm^{-2}s^{-1}}$]
$10\,000 \leq N_e \leq 30\,000$							
X-ray AGN	50 770	507 354	0.1	12 290	122 173	0.6	
$10\,000 \leq N_e$							
X-ray AGN	71 713	717 118	0.0	17 309	172 581	0.4	$8.0 \cdot 10^{-14}$

As a summary of the results on the blazar sample, Tab. 6.11 shows the total significance from the Geiger tower and scintillator analysis described in this thesis and confronts these results with measurements at different wavelengths: the radio flux at 4.85 GHz is taken from the Green Bank Catalog of Radio Sources [154], the X-ray flux between 0.1 and 2.4 keV is taken from recent ROSAT observations comprised in [11], and the high energy data are Whipple and EGRET measurements. HEGRA flux estimates are given for the two sources with a combined significance $> 3\,\sigma$, else 90 % confidence level flux upper limits are calculated.

6.6 Outlook

What do we expect from air shower experiments in the near future ?
The precedent analysis has shown that with the (marginal) detection of blazars as sources of > 50 TeV γ-rays, we are close to the limits of current air shower arrays. Increasing statistics will help us to manifest the detection and to analyze the time stability of the generic source and of individual objects from the sample: as the 4.9 σ excess of 0116+319 shows, the detection of single sources is within reach.
On the other hand, due to the huge background, further information like the energy spectrum of the sources will be difficult to obtain even with large statistics.
Lowering the energy threshold and developing γ/hadron techniques at low energies is the most promising way of improving existing arrays, as it fills the gap between the energy range of current air shower arrays and Čerenkov telescopes. Fig. 2.14 shows that upper limits at 10 TeV are very close to theoretical predictions.

Two new projects are entering into the heritage of air shower physics in the near future: the Pierre Auger Project [155] and the MILAGRO water Čerenkov detector [156]. Both detectors are built with the aim of solving problems raised by air shower arrays in the past.

(1) The Auger array is planned as a huge detector system with 3000 particle detector stations on a grid with 1.5 km spacing, thus covering an area of 5000 m^2. A second component, based on the Fly's Eye technique, will detect the fluorescence light caused by collisions of shower particles with air molecules.
The main goal of Auger is to solve the long-standing problem of the origin of the highest energy cosmic rays [117]. About 50 showers with energies exceeding 100 EeV are expected for Auger-sized detectors. To cover the whole sky, the Auger group considers building equivalent arrays in the northern and in the southern hemisphere.

(2) MILAGRO is a water Čerenkov detector of size $60 \times 80 \times 8\,m^3$, located 2600 a. s. l. near Los Alamos in New Mexico. Three layers of phototubes will detect the Čerenkov light produced by secondary particles.
One of the main advantages of air shower arrays or water Čerenkov detectors like MILAGRO is their large field of view and the possibility of probing each source of the catalogue for a certain time *every day*. We know that one of the main features of blazars is their rapid variability, thus an all-day monitoring of blazars with high sensitivity detectors is the most promising way of understanding the processes in AGN. For earth-bound detectors, this inevitably means that the energy threshold has to be lowered. For MILAGRO, γ-ray thresholds of about 500 GeV are expected. This would not only allow to observe prominent sources continuously, but also to search for yet unknown sources of TeV emission by producing the first sky-map at energies about 1 TeV.

Another important consequence of proton-initiated cascades in jets is a neutrino flux at ultra-high energies $E_{\nu,max} \simeq (10^8 - 10^{10})$ GeV [157]. Observing neutrinos at GeV to PeV energies thus complements γ-ray observations and is also likely to provide a tool for discriminating between theories. As neutrinos do not interact with the radiation background, a considerably larger part of the universe is probed. The Antarctic Muon and Neutrino Detector AMANDA [158] is a promising step on the way towards detecting the neutrino background from blazars, and definite results will certainly come from the next generation of neutrino telescopes with sensitive volumes of km^3.

One of the most important questions of astroparticle physics still is the infrared background absorption. As explained in Chapter 2, the actual strength of the infrared absorption is not only a vital question for TeV astrophysics as such, but also touches the most important *cosmological* questions like galaxy formation in the early universe, cold and hot dark matter, and the actual value of the Hubble constant.
High energy γ-ray astronomy may approach the problem in two ways. Detailed knowledge of the energy spectrum and the cutoff energy of several sources at different redshifts allows to directly pin down the infrared photon density at different energies. Furthermore, a determination of the γ-ray horizon $\tau_{\gamma\gamma} = 1$ at different energies by measuring the maximum redshift z_{max} beyond which the universe becomes opaque would provide us with indirect information on the background radiation.
Of course, several well-established sources are necessary to minimize the dependance on intrinsic effects. One of the future detectors which will help to solve this question is the 17 m MAGIC Čerenkov telescope project [159]. With this tool, the detection of point sources will be possible with high significance on short time scales. This will allow TeV astronomy to take part in multifrequency campaigns which study the time variability of blazars by simultaneous observations at all wavelengths in order to reveal the history of flares.
Furthermore, an improved angular resolution will allow to search for deviations from point-like behavior. If emission at the highest energies is typical of the blazar class, cascading inevitably takes place near the sources and while γ-rays traverse the cosmic ray background radiation. These processes may help us to gain information about external radiation fields and intergalactic magnetic fields.

Table 6.11: **Summary of blazar properties and results.**

source	z	Φ(4.85 GHz) [Jy]	ROSAT [10^{-10}erg cm^{-2} s^{-1}]	EGRET [10^{-7}cm^{-2} s^{-1}]	Whipple [10^{-12}cm^{-2} s^{-1}]
0055+300	0.017	0.91	-	< 0.8	-
2201+044	0.028	0.75	0.03	< 0.5	-
1101+384	0.031	0.72	29	1.57	15.9
0430+052	0.033	3.49	1.1	< 1.4	-
1652+398	0.034	1.37	1.2	< 1.0	8.1
2344+513	0.044	0.23	-	-	($\simeq 3\sigma$)
1514+004	0.052	1.63	0.03	< 0.9	-
1727+502	0.055	0.16	0.34	< 3.9	< 6.9
0402+379	0.055	0.94	-	-	-
0116+319	0.059	1.57	0.01	< 1.1	< 13
0802+243	0.060	1.86	(nd)	< 1.1	-
1214+381	0.062	-	0.03	< 0.5	-

Radio fluxes at 4.85 GHz from the Green Bank Catalog of Radio Sources [154]
ROSAT fluxes between 0.1 and 2.4 keV taken from [11]
EGRET integral fluxes > 100 MeV from [3, 4, 5]
Whipple integral fluxes > 300 GeV from [142, 7]

source	HEGRA telescope [10^{-11}cm^{-2} s^{-1}]	HEGRA 94/95 [σ]	HEGRA 89-92 [σ]	HEGRA flux [10^{-13}cm^{-2} s^{-1}]
0055+300		1.2	0.5	< 2.2
2201+044		1.7	1.4	< 3.1
1101+384	0.8	1.7	2.4	< 3.8
0430+052		0.3	-0.8	< 1.5
1652+398	($\simeq 5\sigma$)	0.0	0.6	< 2.0
2344+513		0.6	0.1	< 1.7
1514+004		1.4	2.9	3.0
1727+502		1.7	-0.1	< 1.7
0402+379		1.3	0.2	< 1.4
0116+319		2.1	4.4	3.4
0802+243		1.0	-1.2	< 1.2
1214+381		1.0	2.3	< 3.7

telescope: integral flux above 1 TeV, taken from [48]
89-92 Archival scintillator data, [74] and this analysis.
94/95 Geiger tower data, this analysis

Chapter 7

Summary

In this thesis, a theory-guided search for extragalactic sources of cosmic rays with energies above 50 TeV is performed. The analysis is based on data taken with the HEGRA air shower array.
Motivated by EGRET observations in the GeV energy region and by TeV detections with ground-based Čerenkov telescopes, the search focusses on nearby ***blazars***, a subclass of Active Galactic Nuclei (AGN) characterized by violent variability, a compact, flat-spectrum radio source, and a featureless, highly polarized continuum emission. Single objects of this class have been subject of intensive search by air shower arrays in the last decade, but all attempts to establish them as γ-ray emitters above 30 TeV have failed, yielding only a number of upper flux limits.
The approach chosen for the analysis presented in this thesis is different from the conventional approach in several aspects. For the first time, a *γ/hadron-separation* is applied which is based on the information provided by the charged particles of air showers. This includes the muonic component, but goes beyond pure muon counting by also analyzing the energy density of the electromagnetic shower content ($e^{\pm}, \gamma$) at different distances from the shower core. High energy particles outside the core region which show up as punch-through electrons are (just like the muons they tend to fake) indicators of hadronic showers.
The necessary information is supplied by the 17 Geiger towers within HEGRA. Their multi-layer structure and their rather moderate thickness of absorbing material makes them powerful tools for exploiting the calorimetric information together with the high energy $e^{\pm}, \gamma$, and $\mu^{\pm}$ content.
The analysis of the data used for γ/hadron separation is consequently based on *neural networks*, as multi-dimensional analysis is the natural approach to problems with a high degree of complexity. In addition to high efficiencies gained by parallel data handling, the neural network technique gives some insight into the physics involved: artificial disabling of input information allows to reveal and asses the separation criteria.
A comparison between the neural net output distribution for experimental data and MC hadron showers does not show systematic deviations. Nevertheless, in order to describe the experimental data correctly, the degraded Geiger array performance due to dead wires, layers, or towers has to be taken into account carefully.

The 90 % upper limit on the ratio of the γ-flux to the overall cosmic ray flux,

$$f_\gamma = \Phi_\gamma/\Phi_{all} \leq 0.033 \ , \tag{7.1}$$

derived from the network output distribution of the experimental data, shows that a diffuse isotropic γ-ray component in the cosmic radiation cannot be detected even with γ/hadron separation. The ratio of the flux of Galactic γ-rays ($|b| \leq 10°$) to the cosmic ray flux is less than

$$\frac{I_\gamma}{I_{CR}} \leq 5.1 \cdot 10^{-4} \tag{7.2}$$

(90 % confidence level).
To further increase the sensitivity of the source search and to smooth the violent time variability of blazars, the *source stacking method* is applied. The main selection criteria for the sample of 12 sources making up the generic blazar is their moderate distance $z \leq 0.062$ and their compactness.
The analysis of a relatively small but well-understood data sample taken with the HEGRA scintillator and Geiger array in November/December 1994 and February to April 1995 yields a $4.1\,\sigma$ excess for the generic blazar after γ/hadron separation, with no single source dominating the excess. The significance distribution of the 12 blazars is shifted to a non-zero mean value of 1.4, thus we observe a true *cumulative* signal. The excess is regularly accumulated at a rate of $\simeq 2$ γ-rays per day from the generic source and shows γ-like behavior in every respect. An analysis of the excess as a function of the source bin size furthermore shows that there is no evidence for a deviation from the behavior expected for point-like sources.
The significance of the excess is rather robust when parameters like the cut in the net output or on the maximum shower size are varied. Nevertheless, the energy range between 50 and 100 TeV turns out to be the region where the excess is accumulated. The estimated flux of

$$\Phi(E \geq 55\text{TeV}) = (1.4 \pm 0.4\ ^{+1.0}_{-0.7}) \times 10^{-13}\text{cm}^{-2}\text{s}^{-1}. \tag{7.3}$$

is in accordance with predictions based on proton acceleration in jets if no external absorption by infrared background photons takes place. The detection of ≥ 50 TeV γ-rays from extragalactic sources provides compelling evidence for the proton blazar model, with consecutive photo-production and cascading being the source of TeV γ-rays rather than synchrotron-self-Compton upscattering off relativistic electrons.
In addition to the generic blazar, the search is extended to source samples comprising BL Lac objects at higher redshift ($0.069 \leq z \leq 0.203$), flat-spectrum galaxies with $0.1 \leq z \leq 1.04$, and steep-spectrum sources with $z \leq 0.1$. No excess is found from these three samples.
The non-detection of the generic BL Lac and the flat-spectrum sources at higher redshift is in accordance with a cutoff due to external absorption becoming relevant above $z \simeq 0.07$. The estimated flux from the nearby blazars completely rules out any scenario predicting a high strength of the infrared-to-optical background.
Apart from the rather small sample analyzed with the Geiger tower γ/hadron separation, also the pure scintillator data taken between 1989 and 1992 show evidence for

γ-emission from the blazars at approximately the same rate, and a preliminary analysis of 1991/92 AIROBICC data supports the observation. *The generic blazar has thus been detected with a significance of more than 6 σ by now.*
As a striking result, the x-ray-selected flat-spectrum AGN $0116 + 319$ at $z = 0.059$ turns out to have the strongest excess in all data sets. The total significance is $4.9\,\sigma$ ($\simeq 6.1\,\sigma$ including the preliminary AIROBICC results). An observation of this source with Čerenkov telescopes seems promising and is performed with the HEGRA telescope array in September/October 1996.
These encouraging results raise our hopes that the detection of single sources with sufficient evidence may be possible with HEGRA in the following years. This would allow us to understand more clearly where the sources of extragalactic cosmic rays are. It may well be possible that our class of objects is just an extremely biased sub-class of the so far unknown class of TeV emitters. If this is true, a number of surprising new discoveries are to be expected from TeV γ-astrophysics in the near future.

Bibliography

[1] C. D. Anderson, Phys. Rev. 43 (1933) 492.

[2] C. M. G. Lattes, H. Muirhead, G. P. S. Occhialini, C. F. Powell, Nature 159 (1947) 694.

[3] C. E. Fichtel et al., Astrophys. J. Suppl. Ser. 94 (1994) 551.

[4] C. von Montigny et al., Astrophys. J. 440 (1995) 525.

[5] D. J. Thompson et al., Astrophys. J. Suppl. Ser. 101 (1996) 259.

[6] M. Punch et al., Nature 358 (1992) 477.

[7] J. Quinn et al., Astrophys. J. 456 (1996) L83.

[8] F. W. Stecker, O. C. de Jager, M. H. Salamon, Astrophys. J. 390 (1992) L49.

[9] F. W. Stecker, O. C. de Jager, M. H. Salamon, Nature 369 (1994) 294.

[10] E. Dwek, J. Slavin, 1994, Astrophys. J. 436 (1994) 696.

[11] K. Mannheim, S. Westerhoff, H. Meyer, H.-H. Fink, Astron. & Astrophys. 315 (1996) 77.

[12] K. Mannheim, Astron. & Astrophys. 269 (1993) 67.

[13] G. Kanbach et al., Space Sci. Rev., 49 (1988) 69.

[14] R. C. Hartman et al., Astrophys. J. 698 (1996) 461.

[15] A. Hewitt, G. Burbidge, Astrophys. J. Suppl. Ser. 87 (1993) 451.

[16] M. J. Disney et al., Nature 376 (1995) 150.

[17] R. A. Sramek, D. W. Weedman, Astrophys. J. 221 (1978) 468.

[18] M. P. Véron-Cetty, P. Véron, A catalogue of quasars and active nuclei (7th edition), ESO Scientific Report No. 17, 195.

[19] J. R. P. Angel, H. S. Stockman, Ann. Rev. Astron. Astrophys. 8 (1980) 321.

[20] B. E. Markarian, 1967-1977, Astrofis, 3-13.

[21] J. N. Bahcall, S. Kirhakos, D. P. Schneider, Astrophys. J. 447 (1995) L1.

[22] R. D. Blandford, A. Königl, Astrophys. J. 232 (1979) 34.

[23] K. I. Kellermann, I. I. K. Pauliny-Toth, Astrophys. J. 155 (1969) L71.

[24] T. J. Pearson et al., Nature 290 (1981) 365.

[25] F. J. Zhang, L. B. Bååth, Astron. & Astrophys. 236 (1990) 47.

[26] B. L. Faranoff, J. M. Riley, Mon. Not. R. Astr. Soc. 167 (1974) 31.

[27] K. Mannheim, Ludwig Biermann Award Lecture (1995), subm. to Rev. Mod. Astr.

[28] C. D. Dermer, R. Schlickeiser, Astrophys. J. 416 (1993) 458.

[29] P. L. Biermann, P. A. Strittmater, Astrophys. J. 322 (1987) 643.

[30] K. Mannheim, W. Krülls, P. L. Biermann, Astron. & Astrophys. 251 (1991) 723.

[31] M. T. Ressell, M. S. Turner, Comments Astrophys. 14 (1990) 323.

[32] P. L. Richards, Proc. 3rd IRAS conference (London), ed. A. Lawrence (Springer Verlag, Berlin, 1988), pp. 289-296.

[33] G. F. Smoot et al., Astrophys. J. 317 (1987) L45.

[34] P. Madau, E. S. Phinney, Astrophys. J. (1995), in press.

[35] J. L. Puget, Astron. & Astrophys. 308 (1996) L5.

[36] S. Lee, FERMILAB-Pub-96/066-A, subm. to Phys. Rev. D.

[37] E. Boldt, Phys. Rep. 146 (1987) 215.

[38] R. J. Protheroe, T. Stanev, Mon. Not. R. Astr. Soc. 264 (1993) 191.

[39] F. A. Aharonian, P. S. Coppi, H. J. Völk, Astrophys. J. 423 (1994) L5.

[40] R. J. Gould, G. Schréder, Phys. Rev. Lett. 16 (1966) 252.

[41] J. V. Jelley, Phys. Rev. Lett. 16 (1966) 479.

[42] W. Heitler, The Quantum Theory of Radiation (Oxford, London, 1960).

[43] S. D. Biller, Astroparticle Phys. 3 (1995) 385.

[44] T. J. Broadhurst, R. S. Ellis, K. Glazebrook, Nature 355 (1992) 55.

[45] C. C. Steidel, M. Dickinson, S. E. Persson, Astrophys. J. 437 (1994) L75.

[46] D. MacMinn, J. Primack, Space Sci. Rev. 75 (1996) 413.

[47] S. D. Biller et al., Astrophys. J. 445 (1995) 227.

[48] D. Petry et al., Astron. & Astrophys. 311 (1996) L13.

[49] J. P. Vallée, Astrophys. J. 360 (1990) 1.

[50] R. Plaga, Nature 374 (1995) 430.

[51] M. Stickel, K. Meisenheimer, H. Kühr, Astron. & Astrophys. Suppl. 105 (1994) 211.

[52] R. Falomo, R. Scarpa, M. Bersanelli, Astrophys. J. Suppl. 93 (1994) 125.

[53] K. MacNaron-Brown et al., Astrophys. J. 451 (1995) 575.

[54] E. S. Perlman et al., The Einstein Slew Survey Sample of BL Lacs.

[55] M. L. Sitko, A. K. Sitko, Publ. Astron. Soc. Pac. 103 (1991) 160.

[56] P. Ciliegi, L. Bassani, E. Caroli, Astrophys. J. 439 (1995) 80.

[57] E. Valtaoja et al., Astron. & Astrophys. 203 (1988) 1.

[58] J. R. Webb, Astronom. J. 95 (1988) 374.

[59] M. Stickel et al., Astrophys. J. 374 (1991) 431.

[60] T. Maccacaro et al., Astrophys. J. 374 (1991) 117.

[61] M. Elvis et al., Astrophys. J. Suppl. 80 (1992) 257.

[62] H. Kühr et al., Astron. & Astrophys. Suppl. Ser. 45 (1981) 367.

[63] R. Giacconi et al., Astrophys. J. 230 (1979) 540.

[64] R. E. Griffiths et al., Mon. Not. R. Astr. Soc. 240 (1989) 33.

[65] R. A. Ong, Nucl. Phys. B 14A (1990) 273.

[66] D. E. Alexandreas et al., Nucl. Instr. Meth. A 311 (1992) 350.

[67] M. Aglietta et al., Nucl. Instr. Meth. A 277 (1988) 23, 336 (1993) 310.

[68] M. Amenomori et al., Phys. Rev. D 47 (1993) 2675.

[69] A. Borione et al., Proc. 24th International Cosmic Ray Conference, Rome 1995, Vol. 2, p. 503.

[70] P. L. Ghia et al., Proc. 24th International Cosmic Ray Conference, Rome 1995, Vol. 2, p. 421.

[71] M. Aglietta et al., Astroparticle Phys. 3 (1995) 1.

[72] D. E. Alexandreas et al., Proc. 23rd International Cosmic Ray Conference, Calgary 1993, Vol. 1, p. 416.

[73] M. Amenomori et al., Astrophys. J. 429 (1994) 634.

[74] M. Merck, PhD thesis, University of Munich (LMU), 1994.

[75] A. Karle et al., Astroparticle Phys. 4 (1995) 1.

[76] A. D. Kerrick et al., Astrophys. J. 452 (1995) 588.

[77] F. W. Stecker, O. C. de Jager, M. H. Salamon, 1996, submitted to Astrophys. J.

[78] R. W. Clay, B. R. Dawson, R. Meyhandan, Astroparticle Phys. 2 (1994) 347.

[79] W. H. Allen, Astroparticle Phys. 1 (1993) 269.

[80] B. Wiebel, University of Wuppertal report WUB 94-08 (1994).

[81] J. N. Capdevielle et al., KFK (Kernforschungszentrum Karlsruhe) report 4998 (1992).

[82] B. Wiebel-Sooth, PhD thesis, University of Wuppertal, in preparation.

[83] K. Mannheim, D. Hartmann, B. Funk, Astrophys. J. 467 (1996) 532.

[84] B. Funk et al., Proc. 3rd Huntsville Symposium on Gamma Ray Bursts, 1995, in press.

[85] H. Krawczynski et al., Proc. 3rd Huntsville Symposium on Gamma Ray Bursts, 1995, in press.

[86] A. Karle et al., Astroparticle Phys. 3 (1995) 321.

[87] W. Rhode et al., Nucl. Instr. Meth. A 378 (1996) 399.

[88] R. Mirzoyan et al., Nucl. Instr. Meth. A 351 (1994) 513.

[89] I. F. Mirabel, L. F. Rodriguez, Proc. 17th Texas Symposium on Relativistic Astrophysics and Cosmology, eds. H. Böhringer, G. E. Morfill, J. E. Trümper, Annals of the New York Academy of Sciences 759 (1995) 21.

[90] F. Aharonian, Talk given at the 15th European Cosmic Ray Conf., Perpignan, 1996.

[91] H. Krawczynski et al., Nucl. Instr. Meth. A, 1996, in press.

[92] K. Greisen, Ann. Rev. Nucl. Part. Sci. 10 (1960) 63.

[93] T. Schmidt, Diploma thesis, University of Wuppertal, in preparation.

[94] T. Odeh, Diploma thesis, University of Wuppertal, 1994.

[95] H. Möller, Diploma thesis, University of Wuppertal, 1995.

[96] CERN Application Software Group, CERN W 5013, Version 3.21 (1994).

[97] P. Doll et al., KFK (Kernforschungszentrum Karlsruhe) report 4686 (1990).

[98] W. R. Nelson et al., SLAC Report 265 (1985).

[99] H. Fesefeldt, RWTH Aachen PITHA 85/02 (1985).

[100] A. Capella, J. Tran Thanh Van, Phys. Lett. B 93 (1980) 146.

[101] K. Werner, Physics Reports 232 (1993) 87.

[102] N. Magnussen, Habilitation thesis, University of Wuppertal, 1996.

[103] J. Matthews et al., Astrophys. J. 375 (1991) 202.

[104] Proc. 4th Int. Worksh. Software Engineering, Artificial Intelligence and Expert Systems for High Energy and Nucl. Phys., ed. B. Denby, Pisa, 1995.

[105] W. S. McCulloch, W. Pitts, Bulletin of Mathematical Biophysics 5 (1943) 115.

[106] D. E. Rumelhart, G. E. Hinton, R. J. Williams, Nature 323 (1986) 533.

[107] J. Hertz, A. Krogh, R. G. Palmer, Introduction to the Theory of Neural Computation (Addison-Wesley, Redwood City, 1991).

[108] K. Hornik, M. Stinchcombe, H. White, Neural Networks 2 (1989) 359.

[109] G. Cybenko, Mathematics of Control, Signals, and Systems 2 (1989) 303.

[110] L. Lönnblad, C. Peterson, T. Rögnvaldsson, Comp. Phys. Comm. 81 (1994) 185.

[111] T. P. Vogl et al., Biol. Cybern. 59 (1988) 257.

[112] J. E. Jackson, A User's Guide To Principal Components (John Wiley, New York, 1991).

[113] S. Denis, S. Phillips, University of Queensland (Department of Computer) techn. report 207 (1991).

[114] R. J. Muirhead, Aspects of Multivariate Statistical Theory (John Wiley, New York, 1982).

[115] J. Petry, Diploma thesis, University of Wuppertal, 1996.

[116] A. Karle et al., Phys. Lett. B 347 (1995) 161.

[117] F. Halzen et al., Astroparticle Phys. 3 (1995) 151.

[118] P. Bhattacharjee, C. T. Hill, D. N. Schramm, Phys. Rev. Lett. 69 (1992) 567.

[119] F. A. Aharonian, P. Bhattacharjee, D. N. Schramm, Phys. Rev. D 46 (1992) 4188.

[120] F. Halzen et al., Phys. Rev. D 41 (1990) 342.

[121] P. Bhattacharjee, N. C. Rana, Phys. Lett. B. 246 (1990) 365.

[122] P. Bhattacharjee, G. Sigl, Phys. Rev. D 51 (1995) 4079.

[123] G. Sigl, S. Lee, P. Coppi, FERMILAB-Pub-96/087-A, 1996, subm. to Phys. Rev. Lett.

[124] D. J. Bird, Phys. Rev. Lett. 71 (1993) 3401.

[125] N. Hayashida, Phys. Rev. Lett. 73 (1994) 3491.

[126] O. Helene, Nucl. Instr. Meth. 212 (1983) 319.

[127] C. Fichtel et al., Astrophys. J. 217 (1977) L9.

[128] S. W. Digel, S. D. Hunter, R. Mukherjee, Astrophys. J. 441 (1995) 270.

[129] J. L. Osborne, A. W. Wolfendale, L. Zhang, J. Phys. G 20 (1994) 1089.

[130] X. Chi et al., Astroparticle Phys. 1 (1993) 129, Astroparticle Phys. 1 (1993) 239.

[131] G. Sigl, K. Jedamzik, D. N. Schramm, V. Berezinsky, Phys. Rev. D. 41 (1990) 342.

[132] R. C. Hartman et al., Astrophys. J. 230 (1979) 597.

[133] H. A. Mayer-Hasselwander et al., Astron. & Astrophys. 105 (1982) 164.

[134] A. W. Strong et al., Astron. & Astrophys., 1996, in press.

[135] S. D. Hunter et al., Proc. 24th International Cosmic Ray Conference, Rome 1995, Vol. 2, p. 182.

[136] P. T. Reynolds et al., Astrophys. J. 404 (1993) 206.

[137] T. A. Porter, R. J. Protheroe, J. Phys. G (1996), subm.

[138] V. S. Berezinsky, V. A. Kudrayavtsev, Astrophys. J. 349 (1990) 620.

[139] V. S. Berezinsky, T. K. Gaisser, F. Halzen, T. Stanev, Astroparticle Phys. 1 (1993) 281.

[140] M. Maisack, K. S. Wood, D. E. Gruber, Astron. & Astrophys. 284 (1994) 28.

[141] Y. Rephaeli, D. Gruber, M. Persic, D. MacDonald, Astrophys. J. 380 (1991) L59.

[142] A. D. Kerrick et al., Astrophys. J. 438 (1995) L59.

[143] D. E. Alexandreas et al., Nucl. Instr. Meth. A 328 (1992) 570.

[144] T. Li, Y. Ma, Astrophys. J. 272 (1983) 317.

[145] M. Amenomori et al., Phys. Review D 47 (1993) 2675.

[146] N. Magnussen, W. Rhode, HEGRA Internal Report, 1996.

[147] J. Prahl et al., Proc. 24th International Cosmic Ray Conference, Rome 1995, Vol. 2, p. 354.

[148] F. Halzen, University of Wisconsin, Madison, MAD/PH/958.

[149] G. Yodh, private communication.

[150] F. Krennrich et al., Proc. High Energy Phys. Div. Meeting, San Diego, April 1996.

[151] R. D. Blandford, A. Levinson, Astrophys. J, 441 (1995) 79.

[152] K. Mannheim, private communication.

[153] D. J. Fegan, Talk given at the 15th European Cosmic Ray Conf., Perpignan, 1996.

[154] P. C. Gregory, J. J. Condon, Astrophys. J. Suppl. Ser. 75 (1991) 1011.

[155] Pierre Auger Project, Design Report, 1995.

[156] G. B. Yodh, Space Sci. Rev. 75 (196) 199.

[157] K. Mannheim, Astroparticle Phys. 3 (1995) 295.

[158] D. Lowder et al., Nature 353 (1991) 331.

[159] S. M. Bradbury et al., Proc. Workshop "Towards a Major Atm. Čerenkov Detector IV", Padua (1995) 277.

Acknowledgements

This work has been pursued in the framework of the HEGRA collaboration and I would like to thank all former and present members.

It is a pleasure to thank Prof. Hinrich Meyer for his constant support. Without his innumerable and fruitful ideas this work would not have been possible.

I wish to thank all Wuppertal members of the HEGRA collaboration, in particular B. Wiebel-Sooth, K. H. Becker, B. Funk, Dr. N. Magnussen, H. Möller, S. Ommer, Dr. W. Rhode, A. Schumacher, and R. N. Sooth.

I am grateful to Dr. Karl Mannheim, Göttingen, for his continuous and encouraging support.

This work has additionally profited from discussions with Prof. Peter L. Biermann, Bonn.

This work was supported by the BMBF, FRG, under contract number 05 2 WT 164.